Numerical Analysis of Electromagnetic Textiles and Application in Emergency Communication Network

by

Houmin Li

A dissertation submitted to the Graduate Faculty of
Auburn University
in partial fulfillment of the
requirements for the Degree of
Doctor of Philosophy

Auburn, Alabama
May 9, 2011

Keywords: electromagnetic textile; artificially electromagnetic surface; textile antenna; emergency communication network; wireless sensor network

Approved by

Gwynedd Thomas, Chair, Associate Professor of Polymer and Fiber Engineering
Lloyd Riggs, Professor of Electrical and Computer Engineering
Peter Schwartz, Professor of Polymer and Fiber Engineering
Ann Beth Presley, Associate Professor of Consumer Affairs
Xinyu Zhang, Assistant Professor of Polymer and Fiber Engineering

Abstract

In this paper, we presented a new type of textile antenna with new radiation mechanism that is capable of resonating at 1/9 the size of a corresponding microstrip antenna due to the woven structures. Further study of this phenomenon suggests development of textile electromagnetic structures with artificially magnetic conductor (AMC) and frequency selective surface (FSS) characteristics. Full-wave finite element method (FEM) simulation of the antennas as well as textile FSS and textile AMC are carried out and compared with existing electromagnetic structures. The results suggest conventional electromagnetic structures such as FSS and AMC can be realized with flexible textile materials. These textile electromagnetic materials possess unique electromagnetic properties that can be applied to a variety of electromagnetic problems, including new kinds of low-profile antennas, standalone FSS and artificial electromagnetic surfaces.

On the other hand, efforts toward development of a novel wireless emergency communication network have been made. Public communication infrastructures are vulnerable to catastrophic events and are usually incapacitated when disaster hits. An airborne Wireless Sensor Network (WSN) with Global Special Mobile (GSM) Short Message Service (SMS) capability is proposed to provide rapidly deployable emergency wireless communication solution. A SMS-WSN node prototype is developed and encapsulated in a weatherproof and airdrop enabled shell. A cargo aircraft loaded with the

SMS-WSN nodes can be deploy to an affected area within hours, distribute thousands of nodes to form a complimentary SMS network which is capable of relaying text messages among all cellular users. Although more work is needed to improve the design, our results have demonstrated the viability of providing text messaging service among cellular users during emergency to help saving people's lives.

Acknowledgments

Foremost I would like to thank God for giving me the strength and determination to achieve my graduate degree. I would like to express deepest appreciation to Dr. Thomas and Dr. Riggs for their continual tutoring, support, and encouragement for every step in the process. I would also like to thank Dr. Schwartz, Dr. Presley, and Dr. Zhang for their contribution to this dissertation by serving on my graduate committee, and Dr. Baginski for serving as my outside reader. To all of the professors and staff that helped me, I am forever grateful. To my research colleagues, David Branscomb, Jeff Thompson, Ashton Johnson, and Joshua Hamilton, I am thankful for all your help throughout my research.

I also would like to express great thanks to my family, for their endless support, encouragement, and love.

Table of Contents

List of Tables

List of Figures

List of Acronyms

8PSK	8-Phase Shift Keying
ACN	Airborne communications node
ADC	Analog to digital converter
AEC	Artificial electric conductor
AMC	Artificial magnetic conductor
AUT	Antenna under test
BTS	Base station
CDMA	Code division multiplexing
EBG	Electromagnetic bandgap
ECN	Emergency communication network
EM	Electromagnetic
FDTD	Finite difference time domain
FEM	Finite element method
FSS	Frequency selective surface
GMSK	Gaussian minimum shift keying
GSM	Global special mobile

GUI	Graphic user interface
IC	Integrated circuit
LCS	Longitudinal corrugated surface
LNA	Low noise amplifier
MCU	Microcontroller
MEMS	Microelectromechanical systems
MOM	Method of moments
PA	Power amplifier
PBG	Photonic bandgap
PEC	Perfect electric conductor
PGA	Programmable gain amplifier
PLL	Phase locked loop
PMC	Perfect magnetic conductor
PML	Perfect matched layer
QoS	Quality of service
RF	Radio frequency
SACCH	Slow associated control channel
SDCCH	Standalone dedicated control channel
SMS	Short text messaging
TCP	Transmission control protocol
TCS	Transverse corrugated surface
UDP	User datagram protocol

USB	Universal serial bus
VCO	Voltage controlled oscillator
WINS	Wireless integrated network sensors
WSN	Wireless sensor network

Chapter 1.Preface

Due to the development of technology, today's society has become an information society in which the creation, distribution, diffusion, use, integration and manipulation of information is a significant economic, political, and cultural activity. The communication of information needs conduits. Physically, there are only two ways to communicate information: wired transmission, and wireless transmission. Land line telephones, cable TV, cable internet falls into the wired category, while cellular communication, satellite communication, wireless local area network, falls into wireless category. As the communication requirement from society grows, wired transmission especially optical fiber technology has become the preferred communication network backbone solution due to the enormous bandwidth it can provide. Meanwhile, wireless technology has become the preferred "last mile" solution to the end user due to its mobility and multi-access capability [1].

A wireless communication system utilizes EM wave to transmit information, and the EM wave transmission and reception is done by means of antennas. Two major functions of antennas are to convert electrical energy to EM wave energy and directionally transmit or receive EM radiation [2, 3]. The antenna is a critical component of a wireless communication system because its properties have direct impact on overall system performance. Ever since the first pair of antennas were developed by Heinrich Hertz in

1887, and especially after the Second World War, antenna theory, design, and application has been developed drastically and has entered a relatively mature stage [3]. However, the development of antenna never ceased, research, exploration and application of wireless technology has placed new requirements on antenna systems including miniaturization, high mobility, and conformity [4].

There is currently much interest in textile antenna systems for body-worn communication or communication off body to fixed and mobile networks. The most widely used portable antennas are whip antennas or ducky antennas. However, these antennas have to be placed perpendicular to a ground plane and do not conform to device surfaces. There are two solutions toward conformal antennas, one is the printed circuit board microstrip antenna, and the other is the textile antenna. The textile antenna has significant advantage over the microstrip antennas in that it is flexible can be integrated into cloth and other textile products. However, the current numerical modeling method on textile antenna is confined to mimicking microstrip antenna using the transmission line model. The transmission line model uses the simplest approximation to study microstrip antennas and only applies to the fundamental radiation mode. Shown in this study, the textile antennas can behave in a far more complicated manner than the microstrip antenna and can operate in radiation mode other than the fundamental mode. To reveal the physics behind the textile antennas, a more strict and useful cavity model is utilized and the higher mode radiation of the textile antenna is used to study the resonant modes higher than the fundamental mode, meanwhile the leaky wave antenna model is used to study the modes lower than the fundamental mode. The results have suggested that by arranging the

conductive yarns properly, the designed textile patch can also be used as frequency selective surfaces.

An effort toward numerical modeling of textile frequency selective surfaces is also given in this study. The periodicity of textile materials makes it a perfect candidate for frequency selective surfaces implementations. However, the current researches on frequency selective surfaces are mostly focused on the hard dielectric backed PCB approach, not much research is done on flexible textile based frequency selective surfaces. The implementation of textile based frequency selective surfaces can be applied to any communication system, large to small, very easily by just covering it with the textile. Moreover, the fabrication process of textile frequency selective surface can also be easily incorporated into advanced composite manufacturing to integrate FSS into composite structures in a one-step process.

Another work presented here is the effort toward developing a solution to the real world problem of emergency communication congestion using the textile antenna and FSS. From the lessons learn through hurricane Katrina, the Select Bipartisan Committee to Investigate the Preparation for and Response to Hurricane Katrina suggests the ECN in the future should rapidly deploy, be portable and easily configured, require low power, and should be integrated into humanitarian aid infrastructure. The recent advances in ultra-low power integrated circuit (IC) technologies have created low cost, low-power, and multi-functional devices, which can be configured and programmed to fulfill the requirements of future terrestrial ECN.

The low-power requirements imply that such communication system must be battery/solar operated, and can only have very limited communication range. Due to the

broadcasting nature of the ECN, omnidirectional antennas must be used. The only ways to improve the communication range for the ECN nodes are either to increase the transmitting power, which is prohibited by the low-power requirement, or to use more efficient antenna and FSS. Whip or ducky antennas are widely studied and efficient. However, they require a size too large (a quarter of the wavelength) being perpendicular to a ground plane, thus do not meet the conformity requirement. Microstrip antennas are conformal, but they are rigid and vulnerable to weather, and generally contained inside the communication device. Their small sizes determined they can only have low radiation efficiency.

In our research, we propose to develop a network containing a large set of relay nodes scattered over a wide area to serve the people in need of emergency communication. The proposed ECN consists of a number of relay nodes that collaborate to accomplish the task of transmitting and receiving data packages such as text messages using the radio link to an emergency responding center node (sink node, such as satellite phone station or 911 station) under conditions when the conventional communication infrastructure is destroyed, a common situation caused by natural disasters. The ECN can serve both survivors and emergency responders for real time communication needs.

In this specific application of ECN, the proposed relay nodes can be deployed in several different ways depending on the scale and severity of the disaster, the population density of the affected area, and the total population affected. The overall system architecture design is presented, a relay node prototype is developed, and the feasibility of applying textile antenna and FSS to the relay nodes is discussed.

Chapter 2.Antenna and Artificial Electromagnetic Surface Fundamentals

2.1.Introduction

Accompanied by the discovery of electromagnetism, antennas have been widely studied for over one hundred years. As electromagnetic (EM) theory develops in depth, the understanding of radiation mechanism of various existing antenna structures has become more mature while new antenna structures has been suggested and tested. Through sophisticated application of the Maxwell equations, antenna design has come to the stage of replacing expensive prototyping and field testing with simulation and numerical analysis [2] .

Meanwhile, Artificial Electromagnetic Surface (AES) as a promising way to further improve antenna and microwave circuit performance, has been widely studied. The hypothetical concept of the Perfect Magnetic Conductor (PMC) has been suggested by mathematicians and applied in EM modeling for years. However, the emergence of High Impedance Surface (HIS), a special type of AES, has brought the possibility to realize the characteristic of PMC as a part of AES and is named Artificially Magnetic Conductor (AMC). With its unique surface wave bandgap property and in phase reflection property, it is possible to drastically reduce sizes of antennas while improving performance and has drawn significant interest from the EM research society.

In particular, frequency selective surface (FSS) is another promising application area of AES or AMC. FSS is typically a large scale periodic planar array with metallic elements or periodic aperture array in a metallic screen. FSS has certain frequency selecting characteristic to EM wave and can be considered as an open space EM filter. FSS itself does not absorb RF energy. Its scattering characteristic is frequency dependent. It is almost transparent to pass band EM wave but opaque to stop band EM wave. The frequency selecting characteristic depends on the shape of the individual array element. Due to its unique property and promising application potentials, FSS with AMC integration has become another popular topic of the EM research area.

As computer technology developed in the past decades, the numerical method has become the preferred way to analyze antenna and AES properties. With powerful computing and optimized differential equation solvers, modern antenna and AES design has become more efficient and accurate. However, no matter what method people use, antenna and AES will always follow the fundamental laws of electromagnetism. This chapter will briefly introduce the fundamental laws of electromagnetism, EM radiation theories, microstrip antenna theories including transmission line model and cavity model, AES in general and FSS theories.

2.2.Maxwell's Equations

An antenna is a conductive component designed to send and receive radio waves. It is a transitional structure between the circuit and the free space. Antenna properties can be analyzed with basic laws of physics. These laws have been collected into a set of equations commonly referred to as *Maxwell's equations.[5]*

The time domain *Maxwell's equations* can be show as

$$\nabla \times \boldsymbol{\mathcal{E}} = -\frac{\partial \boldsymbol{\mathcal{B}}}{\partial t} - \boldsymbol{\mathcal{M}} \tag{2-1}$$

$$\nabla \times \boldsymbol{\mathcal{H}} = -\frac{\partial \boldsymbol{\mathcal{D}}}{\partial t} + \boldsymbol{\mathcal{J}} \tag{2-2}$$

$$\nabla \cdot \boldsymbol{\mathcal{D}} = \rho(t) \tag{2-3}$$

$$\nabla \cdot \boldsymbol{\mathcal{B}} = m \tag{2-4}$$

The cross and dot operators are referred to as the curl and divergence respectively. Another equation can be derived from equation (2-2) and (2-3) is

$$\nabla \cdot \boldsymbol{\mathcal{J}} = -\frac{\partial \rho(t)}{\partial t} \tag{2-5}$$

Equation (2-5) is denoted as the continuity equation to describe the electric current density $\mathcal{J}$ in terms of the movement of volumetric electric charge, ρ. A similar relationship also exists for the magnetic current density $\mathcal{M}$ and volumetric magnetic charge m. The other quantities $\mathcal{E}$, $\mathcal{H}$, $\mathcal{D}$, $\mathcal{B}$, are electric and magnetic field intensity, and the electric and magnetic field densities respectively.

In most antenna applications, the EM analysis is based on sinusoidal varying sources in a linear environment. For time-harmonic fields with a single radian frequency of ω, we can use the phasor form of the electrical field

$$\boldsymbol{\mathcal{E}} = \mathrm{Re}(\mathbf{E} \cdot e^{j\omega t}) \tag{2-6}$$

and the phasor form of *Maxwell's equations* can be derived as

$$\nabla \times \mathbf{E} = -j\omega\mathbf{B} - \boldsymbol{\mathcal{M}} \tag{2-7}$$

$$\nabla \times \mathbf{H} = j\omega\mathbf{D} + \boldsymbol{\mathcal{J}} \tag{2-8}$$

$$\nabla \cdot \mathbf{D} = \rho \qquad (2\text{-}9)$$

$$\nabla \cdot \mathbf{B} = m \qquad (2\text{-}10)$$

and the phasor form continuity equation

$$\nabla \cdot \mathbf{J} = -j\omega\rho \qquad (2\text{-}11)$$

If there is more than one frequency present, the solution to the *Maxwell's equations* may be found for each individual frequency separately and the results combined for the total solution. The linearity environment restriction is to ensure that the analysis should be restricted to a single frequency. For nonlinear environment, it is advantageous to solve the time-domain equations first and obtain the frequency-domain form through a Fourier transform process.

Maxwell's equations define relationships between the field quantities, but do not provide information about the media in which these fields exist. The material can be characterized by three quantities: permittivity ϵ, permeability μ, and conductivity σ. Sometimes the material conductivity is given in the form of resistivity $\rho = \frac{1}{\sigma}$. These quantities define the relationship between the density and intensity quantities as well as the portion of the current due to conduction. Thus we have $\mathbf{D} = \epsilon\mathbf{E}$, $\mathbf{B} = \mu\mathbf{H}$, and $\mathbf{J} = \sigma\mathbf{E}$. Applying these to the *Maxwell's equations* give

$$\nabla \times \mathbf{E} = -j\omega\mu\mathbf{H} - \mathbf{M} \qquad (2\text{-}12)$$

$$\nabla \times \mathbf{H} = (\sigma + j\omega\epsilon)\mathbf{E} + \mathbf{J_i} \qquad (2\text{-}13)$$

$$(\epsilon - \frac{\sigma}{j\omega})\nabla \cdot \mathbf{E} = \rho_i \qquad (2\text{-}14)$$

$$\mu\nabla \cdot \mathbf{H} = m \qquad (2\text{-}15)$$

and

$$\nabla \cdot \mathbf{J_i} = -j\omega\rho_i \qquad (2\text{-}16)$$

The i-subscript denotes the impressed sources in the system, equivalent to the independent sources of circuit theory. The medium is described by scalar quantities, which implicating the media is isotropic. And the material parameters are extracted from the derivatives, which implicating the media is constant and homogeneous. Such simplifications are valid for common antenna problems.

2.3.Fundamental Theory of EM Radiation

EM Radiation is caused by current source and magnetic source. Given the distribution of current and magnetic source, the EM field distribution of any arbitrary position can be determined by solving Maxwell's equation. When analyzing a radiation problem, it is typical to solve radiation source, then calculate the radiation field accordingly. The auxiliary potential function method is most widely used in solving such problems [2]. The most commonly used auxiliary function pair is **A** (magnetic vector potential) and **F** (electric vector potential). It is common practice to solve auxiliary functions, and then solve the EM field to simplify the problem.

Figure 2.1 shows the relationship between the different function pairs. Normally the integration and differentiation of path 2 is easier than the integration of path 1 alone.

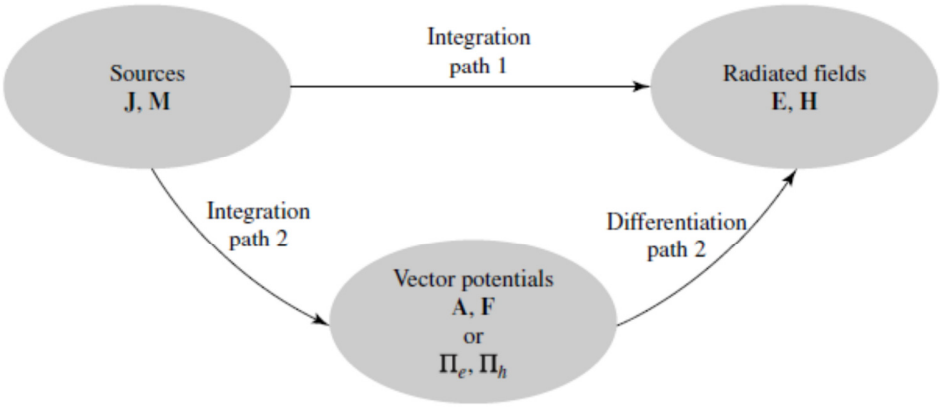

Figure 2.1 Diagram for computing EM fields [2].

2.3.1.Source Current Densities J and M

The vector potential A is widely used when solving the EM field generated by current density J. We define

$$\mathbf{H}_A = \frac{1}{\mu}\nabla \times \mathbf{A} \qquad (2\text{-}17)$$

Solving A and J using vector identity and Maxwell equation (2-13) gives

$$\nabla^2\mathbf{A} + \mathrm{k}^2\mathbf{A} = -\mu\mathbf{J} \qquad (2\text{-}18)$$

The E-field satisfies

$$\mathbf{E}_A = -\nabla\phi_e - j\omega\mathbf{A} = -j\omega\mathbf{A} - j\frac{1}{\omega\mu\epsilon}\nabla(\nabla\cdot\mathbf{A}) \qquad (2\text{-}19)$$

Once **A** is known, $\mathbf{H}_A$ can be found from (2-17) and $\mathbf{E}_A$ from (2-19).

Although magnetic current source **M** is considered physically unrealizable, the volume or the surface equivalent magnetic currents is widely used when solving real EM problems.

Harmonic magnetic current **M** generates potential vector **F. F** satisfies the following relationship:

$$\nabla^2\mathbf{F} + k^2\mathbf{F} = -\epsilon\mathbf{M} \qquad (2\text{-}20)$$

If we define

$$\mathbf{E}_F = -\frac{1}{\epsilon}\nabla \times \mathbf{F} \qquad (2\text{-}21)$$

Apply vector identity and Maxwell equation (2-12)(2-12)

$$\mathbf{H}_F = -j\omega\mathbf{F} - \frac{j}{\omega\mu\epsilon}\nabla(\nabla \cdot \mathbf{F}) \qquad (2\text{-}22)$$

Once **F** is known, $\mathbf{E}_F$ can be found from (2-21) and $\mathbf{H}_F$ from (2-22).

In order to solve EM field, the source currents **J** and **M** must be solved first, then **A** and **F** can be solved, and finally using the above equations, **E** and **H** field generated by **J** and **M** can be solved accordingly.

Electric current density **J** and vector potential **A** satisfies the following relationship

$$\mathbf{A} = \frac{\mu}{4\pi}\iiint_v \mathbf{J}\frac{e^{-jkR}}{R}dv' \qquad (2\text{-}23)$$

While magnetic current density **M** and vector potential **F** satisfies the following relationship

$$\mathbf{F} = \frac{\epsilon}{4\pi}\iiint_v \mathbf{M}\frac{e^{-jkR}}{R}dv' \qquad (2\text{-}24)$$

Where $k^2 = \omega^2\mu\epsilon$ and R is the distance from any point in the source to the observation point. Then we can find $\mathbf{H}_A$ from (2-17), $\mathbf{E}_A$ from (2-19), $\mathbf{H}_F$ from (2-22), and $\mathbf{E}_F$ from (2-21).

The total fields are then determined by

$$\mathbf{E} = \mathbf{E}_A + \mathbf{E}_F = -j\omega\mathbf{A} - j\frac{1}{\omega\mu\epsilon}\nabla(\nabla\cdot\mathbf{A}) - \frac{1}{\epsilon}\nabla\times\mathbf{F} \quad (2\text{-}25)$$

$$\mathbf{H} = \mathbf{H}_A + \mathbf{H}_F = \frac{1}{\mu}\nabla\times\mathbf{A} - j\omega\mathbf{F} - \frac{j}{\omega\mu\epsilon}\nabla(\nabla\cdot\mathbf{F}) \quad (2\text{-}26)$$

When computing using the far field approximations, the second term in $\mathbf{E}_A$ and $\mathbf{H}_F$ expressions can be negligible, and thus further simplify the problem.

2.3.2.Far Field Radiation

The radiated wave can be considered as spherical plane wave from an antenna with finite sizes. The solution of the vector wave equation under spherical coordination can be expressed as:

$$\mathbf{A} = \hat{\mathbf{a}}_r A_r(r,\theta,\varphi) + \hat{\mathbf{a}}_\theta A_\theta(r,\theta,\varphi) + \hat{\mathbf{a}}_\varphi A_\varphi(r,\theta,\varphi) \quad (2\text{-}27)$$

The amplitude variations of r in each component has the form of $\frac{1}{r^n}, n = 1,2,\ldots$ and (2-27) can be reduced to

$$\mathbf{A} \cong \left[\hat{\mathbf{a}}_r A'_r(\theta,\varphi) + \hat{\mathbf{a}}_\theta A'_\theta(\theta,\varphi) + \hat{\mathbf{a}}_\varphi A'_\varphi(\theta,\varphi)\right]\frac{e^{-jkr}}{r}, r\to\infty \quad (2\text{-}28)$$

Substituting (2-28) into (2-17) and (2-19) we get

$$\mathbf{E} = \frac{1}{r}\left\{-j\omega e^{-jkr}\left[\hat{\mathbf{a}}_r(0) + \hat{\mathbf{a}}_\theta A_\theta(\theta,\varphi) + \hat{\mathbf{a}}_\varphi A_\varphi(\theta,\varphi)\right]\right\} + \frac{1}{r^2}\{\ldots\} + \cdots \quad (2\text{-}29)$$

$$\mathbf{H} = \frac{1}{r}\left\{-j\frac{\omega}{\eta}e^{-jkr}\left[\hat{\mathbf{a}}_r(0) + \hat{\mathbf{a}}_\theta A_\theta(\theta,\varphi) + \hat{\mathbf{a}}_\varphi A_\varphi(\theta,\varphi)\right]\right\} + \frac{1}{r^2}\{\ldots\} + \cdots \quad (2\text{-}30)$$

Where $\eta = \sqrt{\mu/\epsilon}$ is the intrinsic impedance of the medium.

Neglecting higher order terms of $1/r^n$, the radiated **E**- and **H**- fields have only θ and φ components. They can be expressed as

$$Far - Field\ Region$$

$$\begin{cases} E_r \cong 0 \\ E_\theta \cong -j\omega A_\theta \quad so\ that\ \mathbf{E}_A \cong -j\omega\mathbf{A} \\ E_\varphi \cong -j\omega A_\varphi \end{cases} \quad (2\text{-}31)$$

$$\begin{cases} H_r \cong 0 \\ H_\theta \cong +j\dfrac{\omega}{\eta}A_\varphi = -\dfrac{E_\varphi}{\eta} \quad so\ that\ \boldsymbol{H}_A \cong \dfrac{\hat{\mathbf{a}}_r}{\eta} \times \mathbf{E}_A \\ H_\varphi \cong -j\dfrac{\omega}{\eta}A_\theta = +\dfrac{E_\theta}{\eta} \end{cases} \quad (2\text{-}32)$$

$$= -j\frac{\omega}{\eta}\hat{\mathbf{a}}_r \times \boldsymbol{A}$$

Radial field components exist only for higher order terms of $1/r^n$.

In a similar manner, the far-zone fields due to a magnetic source **M** (potential **F**) can be written as

$$\mathbf{H}_F \cong -j\omega\mathbf{F} \quad (2\text{-}33)$$

$$\boldsymbol{E}_F \cong -\eta\hat{\mathbf{a}}_r \times \mathbf{H}_F = j\omega\eta\hat{\mathbf{a}}_r \times \boldsymbol{F} \quad (2\text{-}34)$$

Finally combining the two corresponding parts gives the total EM field. It can be easily shown that the **E** and **H** fields are orthogonal in the far field and thus forms a TEM wave. The radiation field can be subdivided into near field, transition zone, and far

radiation field based on the distance from the radiator. In practice the smallest radial distance of far field is $2D^2/\lambda$ where D is the largest dimension of the radiator.

2.4.Microstrip Antenna Basics

The MSA is a low profile antenna. It is also named as patch or planar antenna. The MSA is a popular built-in antenna for electronics because of it is lightweight, inexpensive, and offers conformal structures [6]. The fundamental radiation mechanism can be explained by studying a rectangular flat plate over a substrate with a ground plane using transmission line model or cavity model.

2.4.1.Transmission Line Model

As shown in Figure 2.2, the microstrip has a dimension of $W \times L$, dielectric thickness of h, $h \ll \lambda_0, \lambda_0$ is the free space wavelength. The radiating patch can be considered as a microstrip transmission line. Since the terminal edge (W) is open circuit, a standing wave will be generated on the patch. The length of the transmission line L can be approximated as $L \approx \frac{\lambda_g}{2}$, λ_g is the wavelength on the transmission line, so that the other terminal edge (W) is open circuit too.

The electric field of MSA can be approximately expressed as

$$E_x = E_0 \cos(\pi y/L) \qquad (2\text{-}35)$$

Also shown in Figure 2.2, the electric field of the MSA is zero at the center, maximum (positive) at one side, and minimum (negative) on the opposite side, according to (2-35). When a signal is applied, the minimum and maximum continuously change sides according to the instantaneous phase of the signal [6]. The length L of MSA is the factor

that causes resonance at its half-wavelength frequency. The radiating edges are the two edges at the ends of the L-dimension of the patch. Radiation that occurs at the ends of the W-dimension is far less compared to those at L-dimension edges, and is normally ignored.

There are several keys to successfully design a MSA structure. First, the structure needs to be a half-wavelength length resonator. Second, a low dielectric constant substrate for the MSA is preferred. Third, a thicker dielectric substrate could broaden the bandwidth, but the substrate thickness should always be just a fraction of a wavelength [2].

The resonant frequency of MSA is inversely proportional to its size. Because of this, MSA are mostly used for frequencies of microwave and above. For frequencies lower than microwave, MSA application is very limited because of the sizes required. For example, an MSA to receive FM radio at 100 MHz would have a size on the order of 1 meter long, which is a very large circuit for any type of substrate. To receive AM radio at 1000 KHz, the MSA would have the size of a football field [2]. One application example of MSA is in satellite radio receivers (XM and Sirius) [6].

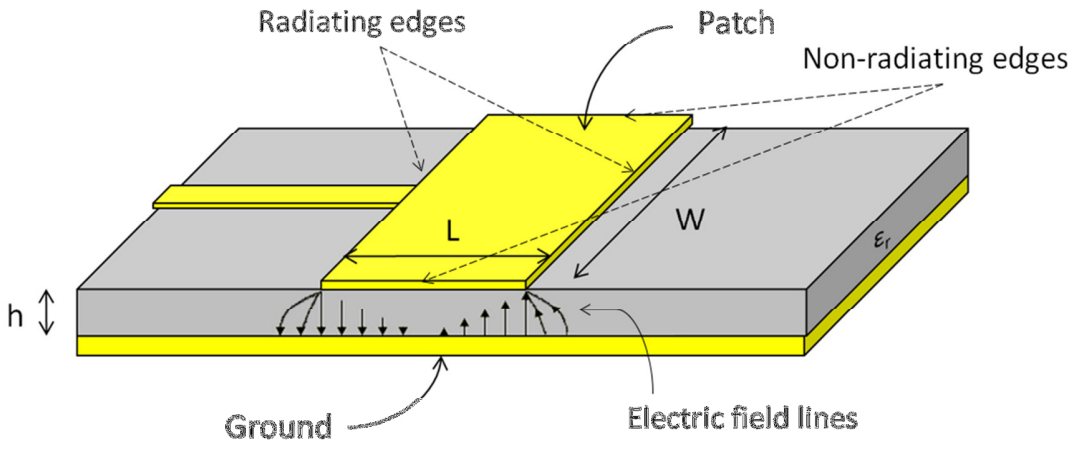

Figure 2.2 Microstrip antenna structure and electric field lines

The radiation efficiency is determined by the patch width W and the impedance matching network. In order to achieve best radiation efficiency, W can be calculated according to (2-36).

$$W = \frac{c}{2f_0\sqrt{\frac{(\varepsilon_r + 1)}{2}}} \tag{2-36}$$

Where c is the speed of light, f_0 is the resonant frequency, and ε_r is the dielectric constant.

Once the resonant frequency f_0 is set by the application requirement, patch length L can be calculated based on effective dielectric constant ε_{reff} according to (2-37) through (2-40).

$$\varepsilon_{reff} = \frac{\varepsilon_r + 1}{2} + \frac{\varepsilon_r - 1}{2}[1 + 12\times\frac{h}{W}]^{-\frac{1}{2}} \tag{2-37}$$

$$L_{eff} = \frac{c}{2f_0\sqrt{\varepsilon_{reff}}} \tag{2-38}$$

$$\Delta L = 0.412h\times\frac{(\varepsilon_{reff} + 0.3)(\frac{W}{h} + 0.264)}{(\varepsilon_{reff} - 0.258)(\frac{W}{h} + 0.8)} \tag{2-39}$$

$$L = L_{eff} - 2\times\Delta L \tag{2-40}$$

To match the antenna impedance to the 50Ω transmission line and feed structure, the edge impedance can be calculated using (2-41) and a quarter wave transformer can be designed accordingly.

$$Z_L = 90\times(\frac{\varepsilon_r^{\,2}}{\varepsilon_r - 1})\times(\frac{L}{W})^2 \tag{2-41}$$

2.4.2.Cavity Model

The transmission line is the simplest model used to study MSA. However, it only applies to the fundamental radiation mode. To study the higher mode radiations, a more strict and useful cavity model must be utilized. The cavity model is first suggested by Y. T. Lo et al. in 1979 [7]. Based on the feature of $h \ll \lambda_0$, MSA can be considers as dielectric-loaded cavities bounded by electric conductors (above and below it) and by magnetic walls (to simulate an open circuit) along the perimeter of the patch. The radiated field can be calculated from the equivalent magnetic current around the cavity, while the input impedance can be calculated from cavity field and feed source boundary condition. The cavity model has been successfully utilized in computing antenna pattern, input admittance, and resonant frequencies and compare well with measurements [7-9] . This model provides a more detailed physical insight into the radiation mechanism of MSA and generates many novel designs and applications. The cavity model can be applied not only to rectangular patch, but also applicable to other regular shape patches. The cavity model is conformant to the transmission line model in that the latter is merely the fundamental radiation mode of the cavity model.

The approximation method used is the cavity model is the two step method. First, calculate the source field distribution on the radiator or equivalent source field distribution on a closed surface surrounding the source. Second, solve the far field distribution based on the solution of the source field distribution to. The second step is a strict mathematical solution based on Huygens principle, but because it is based on the

approximation result from step 1, the overall solution is an approximate solution. The overall accuracy depends on the accuracy of step 1.

First solve for the near field:

Select the coordination as shown in Figure 2.3, when $h \ll \lambda_0$, it can be assumed that: (1) the E-field has only E_z component, while the H-field has only H_x and H_y components, in other words, the field inside the cavity is has only TM mode in z direction. (2) The field inside the cavity does not vary with z. (3) the current around the cavity does not have normal components, thus the tangential component of H-field is zero, so the side walls of the cavity can be considered as PMC boundaries. This is assumption is made for ease of calculation, in reality MSA has a fringing effect like microstrip transmission lines, the fringing effect can be accounted for by calculating the equivalent effective sizes.

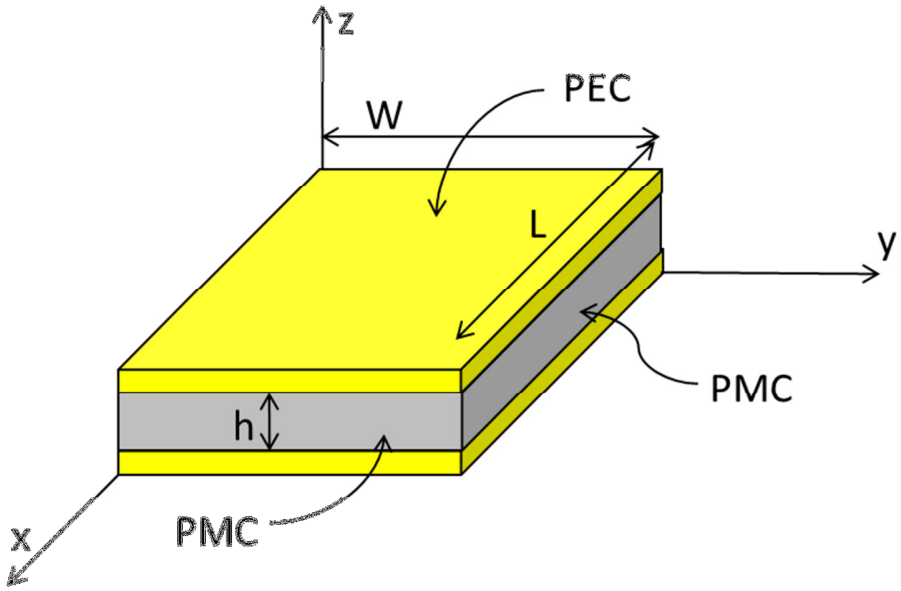

Figure 2.3 Microstrip antenna cavity model coordination selection

The assumptions result in a modified form of the Maxwell equation:

$$\nabla \times \mathbf{H} = -\mathrm{j}\omega\epsilon\mathbf{E} + \mathbf{J}$$
$$\nabla \times \mathbf{E} = -\mathrm{j}\omega\mu_0\mathbf{H}$$
$$\nabla \cdot \mathbf{H} = 0 \qquad (2\text{-}42)$$
$$\nabla \cdot \mathbf{E} = 0$$

Since $h \ll \lambda_0$, current source $\mathbf{J}_z$ can be considered constant along z direction, so $\nabla \cdot \mathbf{J} = -j\omega\rho = 0$, thus $\nabla \cdot \mathbf{E} = 0$. From (2-42) we can get

$$\nabla^2\mathbf{E} + k^2\mathbf{E} = j\omega\mu_0\mathbf{J} \qquad (2\text{-}43)$$

Where $k = \omega\sqrt{\mu_0\varepsilon} = k_0\sqrt{\varepsilon_0(1 - j\tan\delta)}$, $\tan\delta$ is the loss tangent of the dielectric material. Since $\mathbf{J} = \hat{z}\mathbf{J}_z$, $\mathbf{E} = \hat{z}\mathbf{E}_z$, (2-43) can be simplified into a scalar equation:

$$(\nabla^2 + k^2)\mathrm{E}_z = j\omega\mu_0\mathrm{J}_z \qquad (2\text{-}44)$$

To solve (2-44), we can use the eigenmode expansion method. This method solves the equation by expressing the solution as a superposition of the eigenvalues. The eigenfunction is derived from the homogeneous wave equation:

$$(\nabla^2 + {k_{mn}}^2)\Psi_{mn} = 0 \qquad (2\text{-}45)$$

Ψ_{mn} must satisfy the PMC boundary condition $\frac{\partial\Psi_{mn}}{\partial n} = 0$, the n on the denominator is the normal vector of the PMC boundary. For regular shape cavities, variable separation can be used to solve for Ψ_{mn} and corresponding k_{mn}.

After solving (2-44), we can get E_z, then using Maxwell Equation (2-42) we can solve for $\mathrm{H_x}$ and $\mathrm{H_y}$ thusly:

$$\begin{cases} Hx = -\dfrac{j}{\omega\mu_0}\dfrac{\partial E_z}{\partial y} \\ Hy = -\dfrac{j}{\omega\mu_0}\dfrac{\partial E_z}{\partial x} \end{cases} \tag{2-46}$$

2.5.Surface Waves

A surface wave is a type of EM wave. Its intrinsic property is an exponential decay away from the surface along the surface normal direction, in other words, the energy is bound in close proximity to the surface.

2.5.1.Conditions of Existence

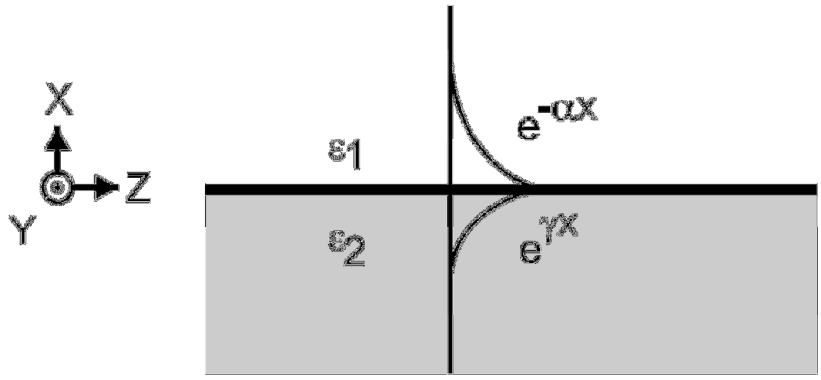

Figure 2.4 Surface wave on a general interface between two media

As shown in Figure 2.4, ε_1 and ε_2 are the dielectric constant of the two media respectively. For the instance of TM mode, assume the surface wave is propagating along z direction and decay in x direction, with e^{jwt} term implicit the E-field components in region I can be written as:

$$E_x = A \cdot e^{-jkz-\alpha x}$$

$$Ey = 0 \qquad (2\text{-}47)$$

$$Ez = B \cdot e^{-jkz-\alpha x}$$

In material II, the electric field has the same form, given below.

$$E_x = C \cdot e^{-jkz+\gamma x}$$

$$Ey = 0 \qquad (2\text{-}48)$$

$$Ez = D \cdot e^{-jkz+\gamma x}$$

Where A, B, C, D, are constants, and k, α, γ are unknown variables. Recall Maxwell equation

$$\nabla \times \mathbf{B} = \frac{\varepsilon_r}{c^2}\frac{\partial E}{\partial t}$$

$$\nabla \times \mathbf{E} = -\frac{\partial \boldsymbol{B}}{\partial t} \qquad (2\text{-}49)$$

Where $= \frac{1}{\sqrt{\mu_0 \varepsilon_0}}$, is the speed of light in vacuum, and from

$$\nabla \times \nabla \times \mathbf{E} = \frac{\varepsilon_r}{c^2}\omega^2 \mathbf{E} \qquad (2\text{-}50)$$

Expanding (2-50) yields

$$\hat{\mathrm{x}}\left(-\frac{\partial^2 E_x}{\partial z^2} + \frac{\partial^2 E_z}{\partial x \partial z}\right) + \hat{\mathrm{z}}\left(\frac{\partial^2 E_x}{\partial x \partial z} - \frac{\partial^2 E_z}{\partial x^2}\right) = \frac{\varepsilon_r \omega^2}{c^2}(\hat{\mathrm{x}}\mathrm{E}_x + \hat{\mathrm{z}}\mathrm{E}_z) \qquad (2\text{-}51)$$

Since the x and z derivatives equal respectively

$$-\frac{\partial^2 E_x}{\partial z^2} + \frac{\partial^2 E_z}{\partial x \partial z} = \frac{\varepsilon_r \omega^2}{c^2}\mathrm{E}_x$$

$$\frac{\partial^2 E_x}{\partial x \partial z} - \frac{\partial^2 E_z}{\partial x^2} = \frac{\varepsilon_r \omega^2}{c^2}\mathrm{E}_z \qquad (2\text{-}52)$$

Substituting (2-47) and into (2-52) we can get

$$k^2 A + jk\alpha B = \frac{\varepsilon_1 \omega^2}{c^2} A$$
$$jk\alpha A - \alpha^2 B = \frac{\varepsilon_1 \omega^2}{c^2} B \tag{2-53}$$

And substitute (2-48) and into (2-52) we can get

$$k^2 C - jk\gamma D = \frac{\varepsilon_2 \omega^2}{c^2} C$$
$$-jk\gamma C - \gamma^2 D = \frac{\varepsilon_2 \omega^2}{c^2} D \tag{2-54}$$

Tangential component of E-field and normal component of D have to be continuous across the dielectric interface, so that

$$\varepsilon_1 A = \varepsilon_2 C$$
$$B = D \tag{2-55}$$

Substituting (2-55) into (2-54) yields

$$\varepsilon_1 k^2 A - jk\gamma \varepsilon_2 B = \frac{\varepsilon_1 \varepsilon_2 \omega^2}{c^2} A$$
$$-jk\gamma \varepsilon_1 A - \varepsilon_2 \gamma^2 B = \frac{{\varepsilon_2}^2 \omega^2}{c^2} B \tag{2-56}$$

Combining equations (2-53) and (2-56) we have four equations and four unknowns k, α, γ, $\frac{A}{B}$. Solving these we can get

$$k = \sqrt{\frac{\varepsilon_1 \varepsilon_2}{\varepsilon_1 + \varepsilon_2}} \frac{\omega}{c}$$
$$\alpha = \sqrt{\frac{-{\varepsilon_1}^2}{\varepsilon_1 + \varepsilon_2}} \frac{\omega}{c} \tag{2-57}$$

$$\gamma = \sqrt{\frac{-\varepsilon_2{}^2}{\varepsilon_1 + \varepsilon_2}}\frac{\omega}{c}$$

Generally speaking region I is air, so that $\varepsilon_1 = 1$, and let $\varepsilon_r = \varepsilon_2$, (2-57) can be simplified into

$$k = \sqrt{\frac{\varepsilon_r}{1 + \varepsilon_r}}\frac{\omega}{c}$$

$$\alpha = \sqrt{\frac{-1}{1 + \varepsilon_r}}\frac{\omega}{c} \qquad (2\text{-}58)$$

$$\gamma = \sqrt{\frac{-\varepsilon_r{}^2}{1 + \varepsilon_r}}\frac{\omega}{c}$$

According to (2-58), for air-dielectric interface, if $\varepsilon_r > 0$, α and γ are pure imaginary numbers, the EM Field does not decay in the x direction, and the TM mode surface wave is not supported, so the plane waves simply propagate through the dielectric interface. On the other hand, if $\varepsilon_r < -1$ (air-metal interface), the solution describes a wave that is bound to the surface. A TM mode surface wave is supported.

Similarly, the solution for TE surface waves can be obtained according to the principle of duality [2]. If the electric and magnetic fields are exchanged, and μ is substituted for ε, the solution above can be applied to the TE case.

2.5.2.Surface Impedance of TE and TM Mode Surface Waves

Referring to Figure 2.4, assume that a surface wave is propagating along the z direction and exponentially decaying in the x direction. The surface impedance Z_s is the impedance looking down on the surface. For the TM mode surface wave:

$$Z_s{}^{TM} = \frac{E_z}{H_y} \tag{2-59}$$

Let,

$$E_z = Ce^{-jkz-\alpha x} \tag{2-60}$$

Recall Maxwell equation

$$\nabla \times \boldsymbol{H} = \varepsilon \frac{\partial E}{\partial t} \tag{2-61}$$

Plug (2-60) into (2-61) we can get

$$H_y = \frac{-j\omega\varepsilon}{\alpha} Ce^{-jkz-\alpha x} \tag{2-62}$$

So the TM mode surface impedance is

$$Z_s{}^{TM} = \frac{j\alpha}{\omega\varepsilon} \tag{2-63}$$

Applying the same procedure to the TE mode surface wave we get

$$Z_s{}^{TE} = -\frac{E_y}{H_z} = \frac{-j\omega\mu}{\alpha} \tag{2-64}$$

It is obvious that the TM mode is supported only when the surface has positive impedance (inductive), and TE mode is supported only for negative impedance (capacitive).

2.6.Artificially Electromagnetic Surface Basics

2.6.1.Definitions

In the field of Electromagnetism and microwave research, new terminologies such as soft and hard surfaces, electromagnetic band-gap (EBG) structures, Negative Index Materials (NIM), and artificial magnetic/electric conductors (AMC/AEC) have arisen and attracted much interest from the research community. These structures or materials do not occur in nature and possess valuable EM properties. Their unique properties have shown great advantages in the applications of high performance antennas and microwave devices.

This work addresses all these structures or materials as Artificially Electromagnetic Surface (AES). The following is a brief definition and introduction of a few AES.

2.6.2.Corrugated Surface

Corrugated surfaces emerged in the 1960s, and were considered the first type of AES. They were mainly designed for corrugated horn antennas. In 1996, Simmons, Rumsey, and Minnett successfully designed hybrid-mode horn antennas with low cross-polarization and symmetrical radiation patterns using corrugated surface [10-12]. Until now, corrugated horn antennas are still widely used as feed source for satellite ground station antennas.

The diagram of classic corrugated surface is shown in Figure 2.5. It is a one-dimensional periodic structure formed by infinite long slots with a quarter wavelengths depth, and the width of slot is far less than a wavelength. Every slot can be considered as a parallel plate waveguide, where the bottom of the slot is a shorted terminal. When the depth of waveguide is greater than a quarter wavelength, the surface impedance

appears to be capacitive and does not support TM mode propagation, while the TE mode can only propagate along y direction. The overall performance is equivalent to a bandstop filter to the surface wave in z direction, thus is called transversely corrugated surface (TCS).

It is worth note that because the depth of the slot is a quarter wavelength, when a z-polarized surface wave incident on the TCS is in the negative x direction, the reflected wave is in phase with the incident wave, which is a characteristic of the ideal Artificial Magnetic Conductor (AMC). The TCS is merely a 1D structure, Lee and Jones further developed a 2-D periodic structure with grating arranged metallic rods, and analyzed its scattering characteristics [13]. While Kildal et al developed the soft and hard surface theory based on these findings and acoustic principles [14, 15].

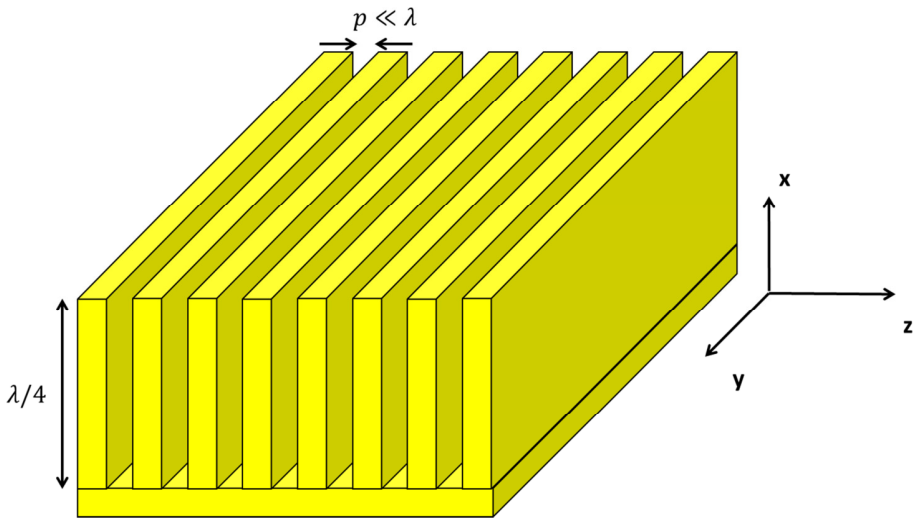

Figure 2.5 Classic corrugated surface

2.6.3.Soft and Hard Surfaces

Starting in 1986, Kildal et al began to investigate the application of the corrugated surfaces in varies of antennas and found that the bandstop characteristic of the corrugated surface is similar to the soft surface in acoustic research, which means the Poynting vector is zero on the corrugated surface within the stop band [16]. Due to the similarity of acoustic and EM waves, a question on whether there is an EM structure similar to acoustic hard surface has been suggested. Based on simple physics reasoning, Kildal et al suggested a modified corrugated surface with the slots filled with dielectric materials, when the EM wave propagates along the y direction (see Figure 2.7), the surface has hard surface characteristic and is called a longitudinal corrugated surface (LCS). Kindal concluded the work on TCS and LCS as well as the corresponding theory in 1988, thus defined the artificially soft and hard surfaces for electromagnetic waves [14].

Table 2-1 Surface impedance and boundary conditions of different EM surfaces

	Transverse Impedance (Z_t)	Longitudinal Impedance (Z_l)	Boundary Condiction (E_t)	Boundary Condiction (E_n)
PEC	0	0	$E_t = 0$	$\frac{\partial E_n}{\partial n} = 0$
PMC	∞	∞	$\frac{\partial E_t}{\partial n} = 0$	$E_n = 0$
Artificially Soft Surface	0	∞	$E_t = 0$	$E_n = 0$
Artificially Hard Surface	∞	0	$\frac{\partial E_t}{\partial n} = 0$	$\frac{\partial E_n}{\partial n} = 0$

To define artificial soft and hard surfaces, anisotropic surface impedance has to first be defined as

$$Z_l = -E_l/H_t \qquad Z_t = -E_t/H_l \qquad (2\text{-}65)$$

Where Z_l and Z_t correspond to the longitudinal and transverse surface impedances, respectively. The subscript l stands for the longitudinal component, while subscript t stands for the transverse component, referring to Figure 2.6 and Figure 2.7 for coordinate definitions. Table 2-1 also gives the surface impedance and boundary conditions of PEC, PMC, and artificial soft and hard surfaces.

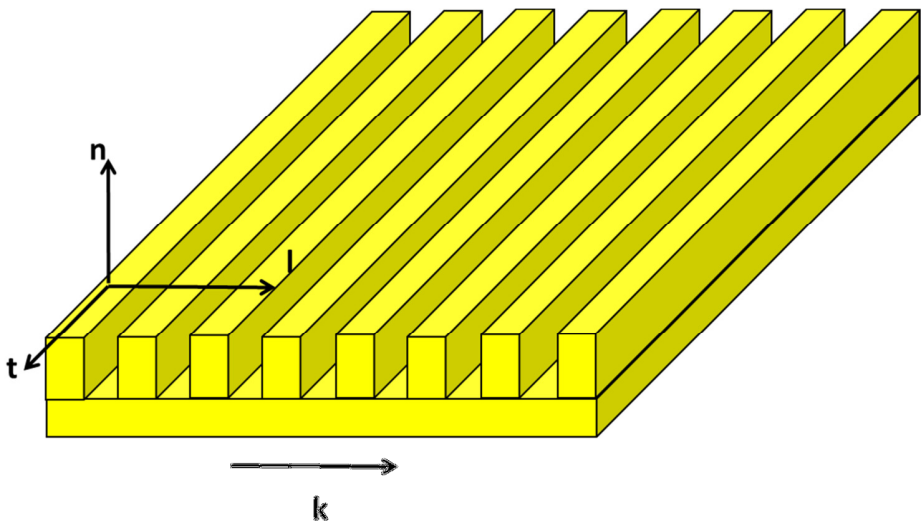

Figure 2.6 Soft surface diagram

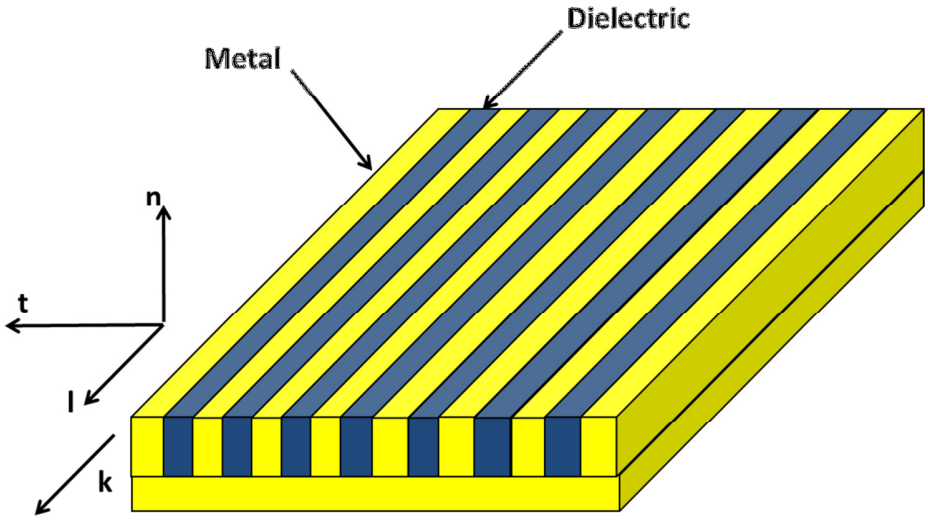

Figure 2.7 Hard surface diagram

Soft surface

Figure 2.6 shows the classic soft surface formed by transverse corrugated metal strips. A soft surface can stop surface wave propagation of any polarization thus is typically used for reduction of cross-polarization and generating symmetrical radiation patterns for corrugated horn antennas. However, since the thickness of the classic soft surface has to be a quarter wavelengths, it is very costly to make and limited in applications. This issue can be solved by dielectric loaded soft surfaces.

Hard surface

Figure 2.7 shows the classic hard surface formed by longitudinal dielectric filled corrugated metal straps. A hard surface can enhance the surface wave propagation on the surface with any polarization, and once rolled up to form a wave guide, the TEM wave mode will be supported. A hard surface horn antenna can be formed if the outlet of the wave guide is broadened, which is one of the most important applications of hard surfaces.

2.6.4.Electromagnetic Bandgap Structures

The electromagnetic Bandgap (EBG) structure, analogous to the Photonic Bandgap (PBG) structure or photonic crystal in the RF and microwave domain, was originated by E. Yablonovitch from Bell labs and S. John from Princeton University independently in 1987 [17, 18] .

Both electrons and photons have wave–particle duality, and obey Schrödinger's equation and Maxwell's equations [19]. Within crystals, the periodic potential around the atoms causes discretization of electron energy, dividing the energy bands into pass bands and stop bands. Meanwhile, it is possible to create an artificial crystal with periodic dielectric constants so that when light passes through it photon energy may separate into a pass band and a stop band as well. For the photon, its energy is proportional to frequency squared, so stop band means photon propagation is prohibited within certain frequency bands. This type of artificial crystal is named as the Photonic Crystal and the band stop feature is named PBG.

Since the EM wave is the same as photons (accordance with Maxwell Equation), PBG can be reproduced in RF and microwave frequencies, so the structure thus is named as EBG structure. EBG structure in general is formed by a series of unit cells periodically arranged inside a substrate material. Proper selection of substrate material, unit cell structure, and unit cell arrangement can result in a band stop feature to surface waves with arbitrary incident angles and polarizations [20].

In 1987, E. Yablonoviteh first proved the band stop feature of 3D PBG through experiment. 1995 J. Joannopoulos in his book explained properties and applications of 1, 2,

3D photonic crystals in detail, and proved that Diamond/BCC structure can provide complete band stop characteristic over three dimensions [19].

EBG structures can be applied in varies fields including microwave circuit, antenna, and optical devices. Its band stop characteristic over RF made it possible to eliminate or reduce surface EM waves to reduce coupling between devices, and improve RF device performance.

EBG can be categorized by the axis dimensions of the unit cell arrangement as shown in Figure 2.8.

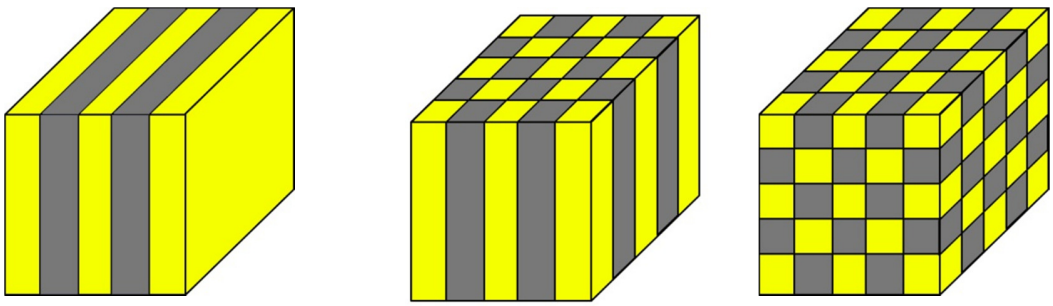

Figure 2.8 One, two, and three dimensional EBG structures

Different dimensional arrangement results in different properties when interacting with surface waves. 1-D EBG, identical to corrugated surface, is the easiest to make and is mostly applied in corrugated antenna and waveguide designs. While 2-D and 3-D EBG require more sophisticated manufacturing processes and are mostly used as AMC/AEC in antenna reflection surfaces or microwave circuits.

Based on the materials used, EBG can also be categorized as dielectric EBG, metal EBG, and hybrid EBG. The 2-D and 3-D dielectric EBG are widely used as patch antenna substrates, suppressing the surface wave on the patch or ground plane thus improving antenna gain and reducing side and back lobes. Metal EBGs are usually etched on the

ground plane and used as microwave transmission lines or in circuit bandstop filters. Hybrid EBG i.e. Sievenpiper mushroom or coplanar EBG also finds application in microstrip antenna ground planes for surface wave reduction.

2.7. Artificially Magnetic Conductor Basics

PEC and PMC are very important concepts in classic EM theory. Because the PEC boundary condition requires the tangential E-field to be zero, the reflected wave and the incident wave are always 180° out of phase. This property determines when using metal as reflective surface to improve antenna gain, the antenna and the reflective surface must be a quarter wavelength apart. If not, the reflected wave E-field will cancel out the radiated wave E-field and reduce antenna efficiency, which is a constraint on reducing antenna dimensions. According to the reciprocity of EM theory, if plane wave is incident on the PMC surface, the reflected wave will be in phase with the incident wave, thus making PMC an ideal choice for an antenna reflection surface. However, PMC do not exist in nature and left PMC exists only in EM theory and an ultimate goal for EM researchers.

In the 1960s, the emergence of the corrugated surface has made in phase reflection possible. However, corrugated surfaces require a quarter wavelength depth to behave like PMC, making it less attractive to the solution of the antenna reflective surface. In 1999, D. Sievenpiper from UCLA suggested a novel EBG structure named High Impedance Surface (HIS). The HIS is based on microstrip substrate, is intrinsically low profile and light weight, and has in phase reflection characteristic just like PMC. The discovery of HIS has attracted much interest from the EM society, and was named Artificial Magnetic Conductor, a

subcategory of Artificial Electromagnetic Material. For convenience purposes, AMC will be used throughout this discussion. The AMC structure suggested by D. Sievenpiper is relatively simple. It consists of an array of metal protrusions on a flat metal sheet arranged in a two-dimensional lattice which are connected to the continuous lower conductor by vertical posts [21]. Due to its shape, the structure is also known as the "Sievenpiper mushroom". The Sievenpiper mushroom is a type of EBG periodic structure, however, the bandgap mechanism is different from PBG's Bragg diffraction mechanism, which requires the unit cell dimension be one half of the corresponding wavelength. The AMC unit cell is much less than a wavelength and has a resonator structure, which makes it a very practical solution to antenna reflective surface problems.

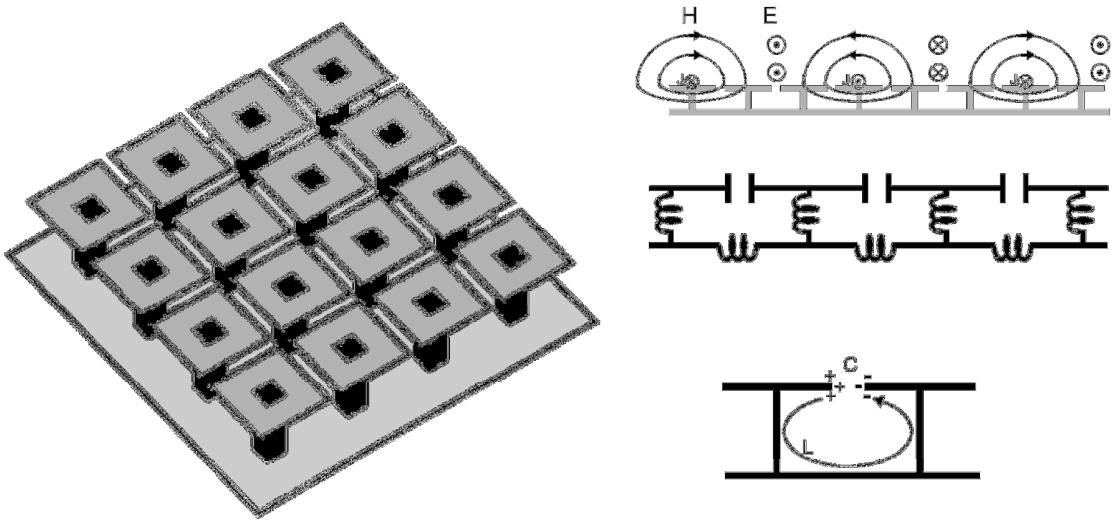

Figure 2.9 Sievenpiper mushroom structure and equivalent circuit [21]

The AMC structure developed by D. Sievenpiper was first called HIS because AMC has high surface impedance at certain frequency range. From the equivalent circuit shown in Figure 2.9, the equivalent circuit suggests a shunt LC resonant circuit, where the gap between patches are coupled to provide capacitance while patch, ground, and plated vias provide equivalent inductance. The surface impedance can be written as

$$Z = \frac{j\omega L}{1 - \omega^2 LC} \tag{2-66}$$

When surface wave frequency is equal or close to the resonant frequency, the surface will have high impedance and prevent surface wave propagation.

To understand the mechanism of the AMC, first we have to look back at corrugated surfaces. The corrugated slots can be considered as a parallel-plate transmission line terminated with shorted load, as shown in Figure 2.10. Assume the plane wave incident along the –x direction, so reflection occurs at the discontinuity at x=0. Let E_i and H_i represent the incident field, E_r and H_r represent reflected field vectors respectively, the incident and reflected fields overlap and form the standing wave:

$$\begin{aligned} E(x) &= E_i e^{jkx} + E_r e^{-jkx} \\ H(x) &= H_i e^{jkx} - H_r e^{-jkx} \end{aligned} \tag{2-67}$$

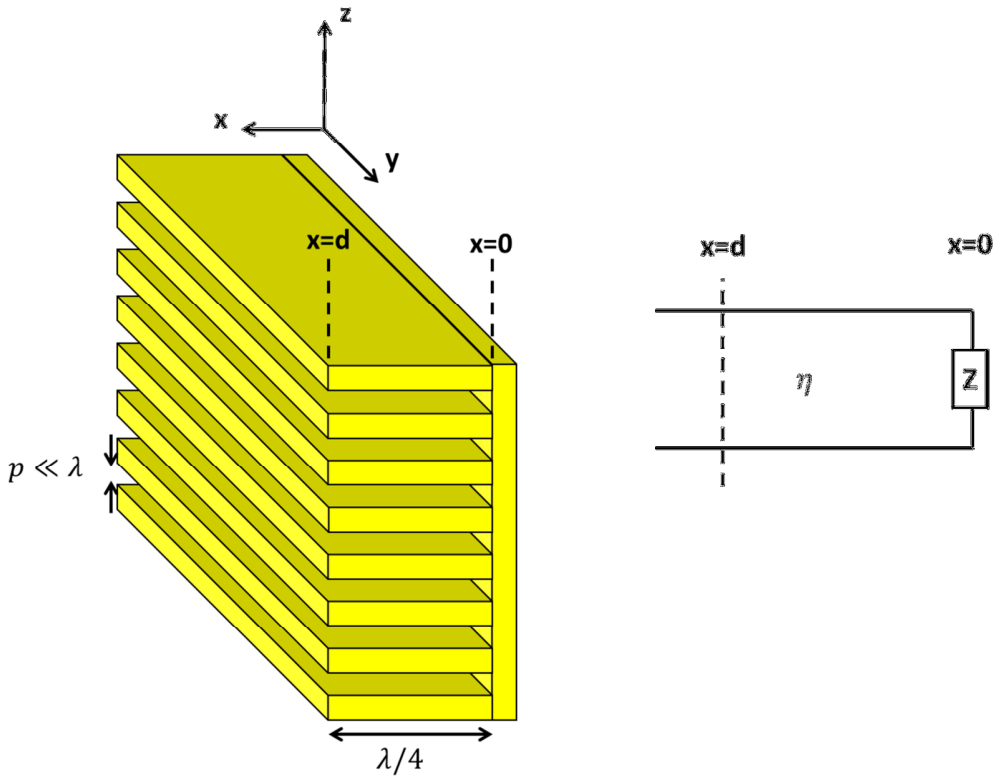

Figure 2.10 Corrugated surface analysis

Wave impedance of the transmission line η can be written as the ratio of E and H field components:

$$\eta = \left|\frac{E_i(x)}{H_i(x)}\right| = \left|\frac{E_r(x)}{H_r(x)}\right| \tag{2-68}$$

The input impedance at x=0, can be written as

$$Z = \frac{E(x)}{H(x)} \tag{2-69}$$

And since the boundary is a short, $Z(0) = 0$, plug into (2-69) we get

$$E_r(0) = -E_i(0)$$
$$H_r(0) = -H_i(0) \tag{2-70}$$

The phase difference between incident and reflection wave can be written as:

$$\phi = Im\left\{\ln(\frac{E_i}{E_r})\right\} = Im\left\{\ln(\frac{Z_s - \eta}{Z_s + \eta})\right\} \tag{2-71}$$

When $\eta \ll Z_s$, phase difference is $\pm\pi$, the surface can be considered as PEC. When $\eta \gg Z_s$, the phase difference is 0, the reflected and incident wave are in phase, so the surface can be considered as PMC. In other words, low impedance surface is equivalent to PEC, while high impedance surface is equivalent to PMC. In reality, good conductors can realize $\pm\pi$ phase difference over entire frequency range, but AMC can only be realized in phase reflection in a very limited frequency band. As a result, the AMC can be considered as PMC only in a limited bandwidth. In general, bandwidth of AMC is defined by the frequency range where $|\phi| < \pi/2$, as shown in Figure 2.11 [21].

Combining (2-67) (2-68) (2-69), we can also get

$$Z(d) = \frac{E(d)}{H(d)} = \frac{E_i(e^{jkd} - e^{-jkd})}{H_i(e^{jkd} + e^{-jkd})} = j\eta\tan(kd) \tag{2-72}$$

From (2-72), when the depth of slot $d < \lambda/4$, Z(d) is positive (inductive) and supports the TM mode surface wave only. When $d = \lambda/4$, $Z(d) \to \infty$, all surface wave modes are suppressed thus the EM bandgap is formed. When $d > \lambda/4$, Z(d) is negative (capacitive), and only the TE mode surface wave is supported. This can be shown in the dispersion diagram in Figure 2.12 [21].

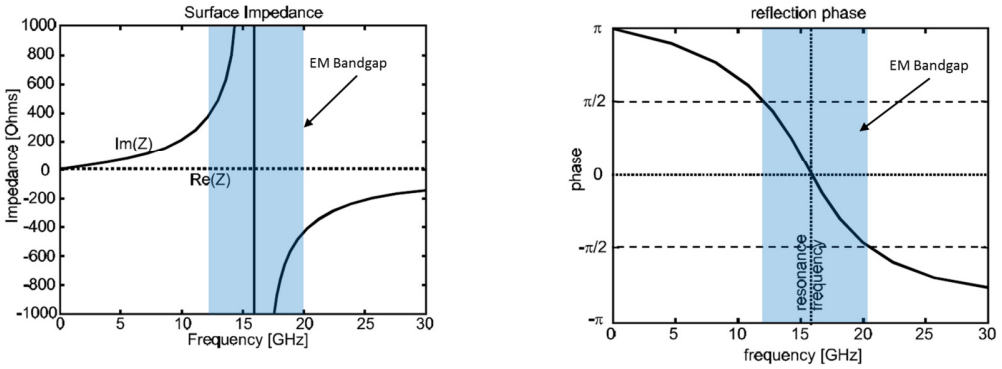

Figure 2.11 Impedance and phase of a parallel resonant circuit [21]

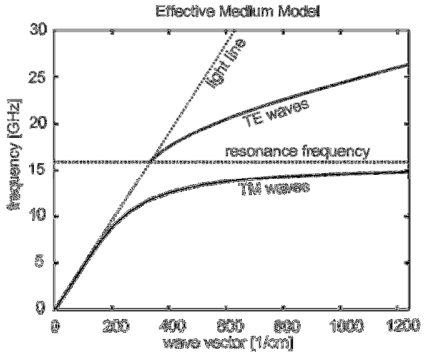

Figure 2.12 Dispersion diagram for bound surface waves [21]

The above analysis is applicable to the surface wave bound to the surface only. For the complete dispersion diagram, the leaky wave mode must be taken into consideration. From Figure 2.12, the TE band begins as a branch out of the light line at the resonance frequency, which is contrary to wave physics. The TE waves that lie to the left of the light line must exist and the only explanation is radiative leaky TE waves.

The radiation from these leaky TE modes can be modeled as a resistor in parallel with the AMC and the modified the equivalent circuit model is shown in Figure 2.13. The circuit equations are satisfied at the resonant frequency. Therefore, the leaky modes that

exist to the left of the light line can be represented by a horizontal line as shown in Figure 2.14.

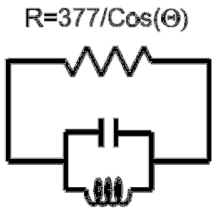

Figure 2.13 Circuit model of leaky TE waves [21]

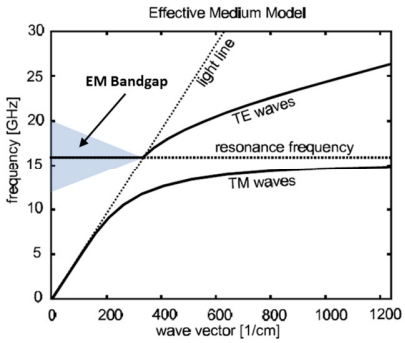

Figure 2.14 Complete dispersion diagram, including leaky modes [21]

A simulated band structure for a two-layer AMC is shown in Figure 2.15. The band gap is clearly shown between the lowest TM and TE modes.

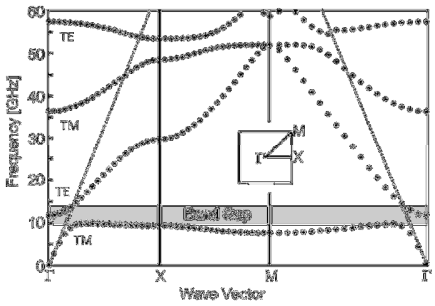

Figure 2.15 Surface wave band structure for a two-layer AMC [21]

2.8. Frequency Selective Surface Basics

One of the major applications of AES is to make Frequency Selective Surface (FSS). The concept of FSS was first suggested by physicist David Rittenhouse over 200 years ago [22]. FSS is typically a single layer or multi-layer planar structure with 2-D periodic elements placed on top of dielectric backing. There are generally two types of FSS: the capacitive FSS (patch-type) and the inductive FSS (aperture-type) as shown in Figure 2.16. FSS has a frequency selecting characteristic which is similar to that of passive EM wave filters. At resonating frequencies, it can be totally reflective (capacitive FSS) or totally transparent (inductive FSS) to the incoming wave.

Figure 2.16 Capacitive and inductive FSS

In general, patch-type FSS is transparent at low frequencies but reflective at high frequencies, which is similar to low pass filters, while aperture-type FSS is the opposite of patch-type and similar to high pass filters. For non-dielectric backed FSS, the frequency response curves of patch-type and aperture-type are complimentary, in accordance with Babinet's principle [23].

Theoretically, scattering of the EM wave will occur for any planar surface with periodically arranged patches or apertures. The scattering characteristic depends on the form of array element, distance between elements, and dielectric layer properties [23]. The periodic structure can be optimized for any particular application with certain characteristics by designing the elements as well as the way they are placed in the periodic array. When the form of the 2-D array is determined, resonance will occur at a certain frequency when the incident EM wave hits the surface. In free space, the resonance usually occurs when the dimension of the element is an integer number of half wavelengths of the incident wave. The scattering is strongest at the first harmonic. As wavelength become smaller, higher order harmonics will occur with less energy scattered, until scattering reaches zero [22, 23].

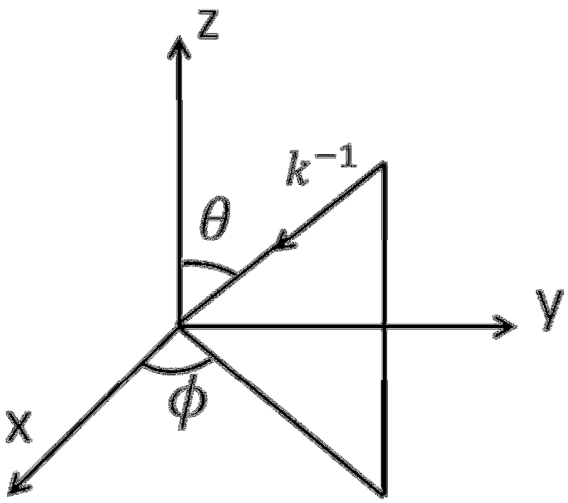

Figure 2.17 Coordination set up of the FSS problem

The research on FSS theory began in the 1960s. With decades of development, several theories have been suggested to analyze FSS properties. Before we formulate the FSS

scattering problem, several assumptions of the FSS have to be made. In general, FSS is assumed to have a 2-D periodic distribution of elements, the elements are infinitely thin PEC patches or apertures, and the incident wave is a homogenous plane wave. The coordination is set up according to Figure 2.17, and the FSS problem set up is shown in Figure 2.18.

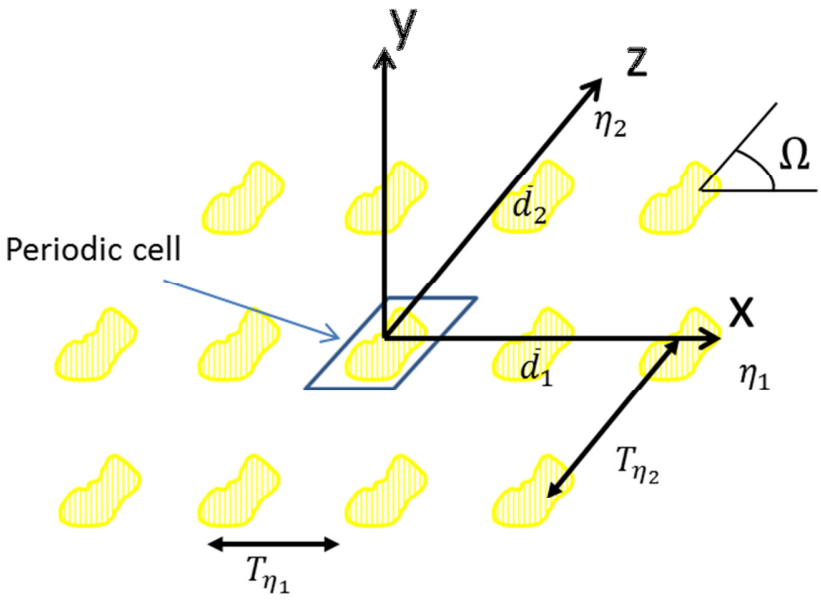

Figure 2.18 Problem set up of FSS

In the same way we treated antenna problems, we can use auxiliary functions to solve FSS problems. Let $\mathbf{J}$ be the induced surface current density on the FSS and $\mathbf{A}$ be the magnetic vector potential generated by **J.** In general, due to the planar nature of the FSS, the induced surface current $\mathbf{J}$ is nonzero only in the transverse direction [22].

Assuming the time convention is $exp\ (j\omega t)$, the transverse (to z) components of $\mathbf{A}$ and $\mathbf{J}$ should have the following relationship:

$$\begin{bmatrix} A_x(x,y) \\ A_y(x,y) \end{bmatrix} = \bar{\bar{\boldsymbol{G}}}(x,y) * \begin{bmatrix} J_x(x,y) \\ J_y(x,y) \end{bmatrix} \qquad (2\text{-}73)$$

Where

$$\bar{\bar{\boldsymbol{G}}} = \frac{\exp(-jk_0 r)}{4\pi r}\bar{\bar{\boldsymbol{I}}}, \qquad r = \sqrt{x^2 + y^2} \qquad (2\text{-}74)$$

$k_0 = free\ space\ wave\ number$

$\bar{\bar{\boldsymbol{I}}} = identity\ tensor$

$*\ is\ the\ convolution\ operator$

Next, the transverse components of the scattered electric field $\boldsymbol{E}^s$ in the plane of the screen, i.e., at z = 0, can be expressed in terms of the transverse components of the vector potential **A**:

$$\begin{bmatrix} E_x^s \\ E_y^s \end{bmatrix} = \frac{1}{j\omega\mu_0}\begin{bmatrix} \dfrac{\partial^2}{\partial x^2} + k_0 & \dfrac{\partial^2}{\partial x \partial y} \\ \dfrac{\partial^2}{\partial x \partial y} & \dfrac{\partial^2}{\partial y^2} + k_0 \end{bmatrix}\begin{bmatrix} A_x \\ A_y \end{bmatrix} \qquad (2\text{-}75)$$

In order to take full advantage of the periodicity of the geometry, it is convenient to rewrite the above equation in the spectral domain [24, 25]. Fourier transform of (2-75) gives:

$$\begin{bmatrix} \bar{E}_x^s(\alpha,\beta) \\ \bar{E}_y^s(\alpha,\beta) \end{bmatrix} = \frac{1}{j\omega\mu_0}\begin{bmatrix} k_0^2 - \alpha^2 & -\alpha\beta \\ -\alpha\beta & k_0^2 - \beta^2 \end{bmatrix}\bar{\bar{\boldsymbol{G}}}\begin{bmatrix} \bar{J}_x(\alpha,\beta) \\ \bar{J}_y(\alpha,\beta) \end{bmatrix} \qquad (2\text{-}76)$$

Where

$$\bar{\bar{\boldsymbol{G}}} = \frac{-1}{2\sqrt{(k_0^2 - \alpha^2 - \beta^2)}}\bar{\bar{\boldsymbol{I}}} \qquad (2\text{-}77)$$

α and β are the transform variables corresponding to the x and y coordinates, respectively.

To take advantage of the periodicity of FSS, we can implement the Floquet Modal analysis. Since FSS is assumed to be infinitely periodic in both x and y directions, the Fourier transform of the induced current **J** is nonzero only for an infinite set of discrete values of the spectral variables α and β. These values, designated here as α_{mn} and β_{mn}, are associated with the Floquet harmonics for the doubly periodic screen, named after the nineteenth century French mathematician Floquet who introduced the concepts of these harmonics in the context of his work on the periodic solution of differential equations. The α_{mn} and β_{mn} can be expressed as:

$$\alpha_{mn} = \frac{2\pi m}{a} + k_0 \sin\theta \cos\phi \tag{2-78}$$

$$\beta_{mn} = \frac{2\pi n}{b \sin\Omega} - \frac{2\pi m}{a}\cot\Omega + k_0 sin\,\theta \sin\phi \tag{2-79}$$

Where θ and ϕ are the angles of the incident plane wave, and according to Figure 2.18, a is T_{η_1} and b is T_{η_2}.

The inverse Fourier transform of (2-76) and the boundary condition $\vec{\boldsymbol{E}}^s = -\vec{\boldsymbol{E}}^i$ on the PEC surface of FSS obtains the following [24]:

$$-\begin{bmatrix} E_x^i(x,y) \\ E_y^i(x,y) \end{bmatrix} = \frac{1}{j\omega\mu\epsilon_0}\sum_m\sum_n \begin{bmatrix} k_0^2 - \alpha_{mn}^2 & -\alpha_{mn}\beta_{mn} \\ -\alpha_{mn}\beta_{mn} & k_0^2 - \beta_{mn}^2 \end{bmatrix}$$

$$\cdot \bar{\bar{\boldsymbol{G}}}(\alpha_{mn},\beta_{mn})\bar{\bar{\boldsymbol{J}}}(\alpha_{mn},\beta_{mn})e^{j\alpha_{mn}x + j\beta_{mn}y} \tag{2-80}$$

$$= \sum_m\sum_n \begin{bmatrix} \bar{G}_{xx} & \bar{G}_{xy} \\ \bar{G}_{yx} & \bar{G}_{yy} \end{bmatrix} \begin{bmatrix} \bar{J}_x(\alpha_{mn},\beta_{mn}) \\ \bar{J}_y(\alpha_{mn},\beta_{mn}) \end{bmatrix} e^{j\alpha_{mn}x + j\beta_{mn}y}$$

Equation (2-80) can then be solved with Galerkin's procedure [24]. Once the induced currents have been solved, other quantities of practical interest, such as reflection and

transmission coefficients for the dominant harmonics, as well as the scattering matrix, can be readily calculated. A practical approach to solving the above equations under various conditions of illumination is to use FEM simulation programs on computers.

The coplanar AMC can also be considered as an FSS with the ground plane. Such an AMC can be formed by using capacitive FSS coupled with the ground plane utilizing the reflection property of the capacitive structure (patch-type). The structure can also be considered as a Sievenpiper mushroom structure without vias, thus has similar phase reflection property as the Sievenpiper mushroom. Because the metal patches are separated from each other on the capacitive FSS, current cannot flow across the gap between the patch elements thus surface wave propagation is prohibited at resonant frequencies and act as AMC.

2.9.Important Parameters of Antennas

2.9.1.Input impedance

The input impedance of an antenna is the impedance presented by an antenna at its terminals or the ratio of the voltage to the current at the pair of terminals or the ratio of the appropriate components of the electric to magnetic fields at a point [2]. Hence the impedance of the antenna can be written as:

$$Z_{in} = R_{in} + jX_{in} \qquad (2\text{-}81)$$

Where Z_{in} is the antenna impedance at the terminals

R_{in} is the antenna resistance at the terminals

X_{in} is the antenna reactance at the terminals

2.9.2.Voltage Standing Wave Ratio

Figure 2.19 shows an equivalent circuit of transmitting antenna. For an antenna to radiate efficiently, the power transferred from the transmitter to the antenna must be maximized. Maximum power transfer can only occur when the impedance of the antenna (Z_{in}) is matched to that of the transmitter (Z_S).

When such a matching condition is not satisfied, some of the power will be reflected to the transmitter. This could cause standing waves, which can be characterized by the parameter Voltage Standing Wave Ratio (VSWR).

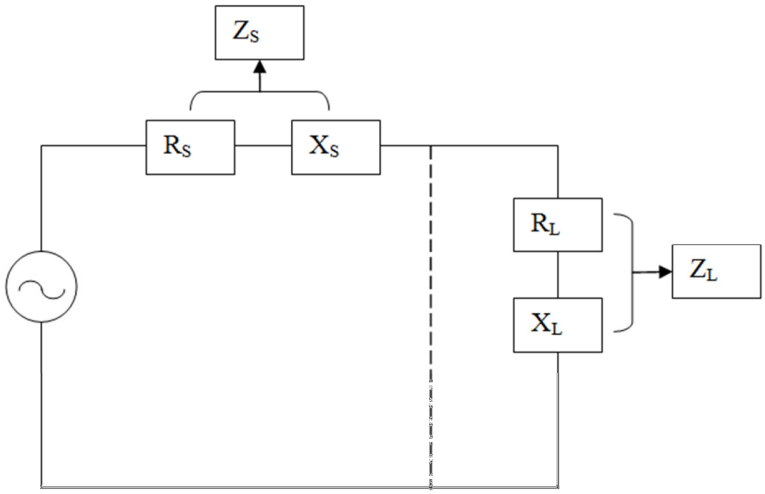

Figure 2.19 Equivalent circuit of transmitting antenna

The VSWR can be expressed as [26]:

$$VSWR = \frac{1+|\Gamma|}{1-|\Gamma|} \qquad (2\text{-}82)$$

$$\Gamma = \frac{V_r}{V_i} = \frac{Z_{in} - Z_S}{Z_{in} + Z_S} \qquad (2\text{-}83)$$

Where Γ is called the reflection coefficient, V_r is the amplitude of the reflected wave, and V_i is the amplitude of the incident wave.

The VSWR represents the impedance mismatch between the transmitter and the antenna. The higher the VSWR, the greater the mismatch will be. The theoretical minimum VSWR which corresponds to a perfect match is unity. A practical antenna design should match an input impedance of 50Ω which is the impedance of the coaxial cable.

2.9.3.Return Loss

The Return Loss (RL) is a parameter similar to VSWR. It is a parameter indicating the amount of power that is lost to the load and does not return as a reflection. As explained in VSWR section, reflected waves lead to the formation of standing waves when the transmitter and antenna impedance do not match. So the RL is a parameter indicating how well the transmitter and antenna matches. RL can be expressed as [26]:

$$RL = -20\log_{10}|\Gamma| \quad \text{(dB)} \qquad \text{(2-84)}$$

When the transmitter and the antenna are perfectly matched, Γ=0 and RL=-∞which means no power is reflected. On the other hand, when Γ=1, RL=0dB, which means all input power is reflected. For practical antenna applications, a VSWR of 2 is acceptable, this equivalent to a RL of -9.5dB.

2.9.4.Radiation Pattern

In the field of antenna design, radiation pattern refers to the directional (angular) dependence of radiation from the antenna [2]. The radiation pattern is directly related to the surface current and the radiation mechanism of the antenna. The radiation pattern is usually presented in polar form with a dB strength scale. Patterns are normalized to the maximum graph value, 0 dB, and directivity is given for the antenna. The plot is typically represented as a three-dimensional graph as shown in Figure 2.20.

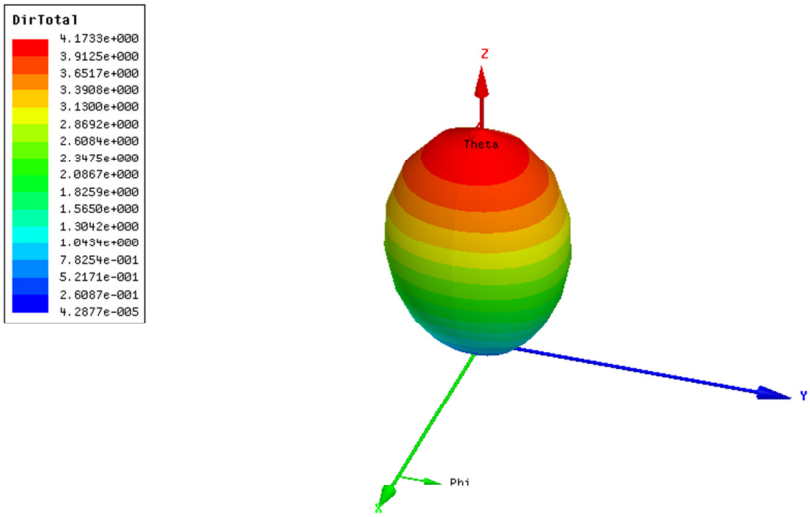

Figure 2.20 Radiation pattern of antenna

2.10.Summary

This chapter first introduced the fundamental EM theories including the Maxwell equations and EM radiation theory. The general routine of solving EM radiation problem was given. Then we introduced the fundamental theory of MSA with transmission line model and cavity model. Transmission line model is easy to understand and easy to use, but

lacked the physical details of how MSA works. The cavity model is stricter than the transmission line model, which offers greater insight into the radiation mechanism of MSA. After that we introduced the fundamental theories of surface wave, AES and AMC. And then FSS was introduced as well as a general routine to solve FSS problems. Lastly the definitions of a few important antenna parameters were introduced. Overall, this chapter serves a basis for the research work that follows.

Chapter 3.Numerical Modeling of Electromagnetic Textiles

3.1.Numerical Modeling Methods

Among the numerical modeling methods, FEM, MOM, and FDTD are the most popular ones. The fundamental concept of FEM is based on the decomposition of the domain and its corresponding boundary condition into a finite number of subdomains (elements) for which the systematic approximate solution is constructed by applying the variational methods [27]. The assumed approximating functions within each element can be expressed by the unknown field variables. These functions are defined in terms of the values of the field variables at the points along the element boundaries and connecting adjacent elements. The discretize procedure greatly reduces the requirement on the computer as well as the calculation time, which makes the method a valuable and practical analysis tool for the solution of boundary, initial, and eigenvalue problems.

In order to analyze antenna problems, the following procedure can be followed. First, establish antenna models by using approximations or empirical formula, calculating the initial design parameters. Second, define metallic, vacuum, dielectric materials and their corresponding properties. Next, define boundary conditions i.e. PEC, PMC, radiation boundary, symmetry planes, and excitation ports i.e. discrete ports, wave guide ports, plane wave sources. Then, define calculation parameters for optimizing system resource

and improving calculation speed and efficiency. Finally, post processing allows analysis for antenna parameters such as S parameters, field distribution, energy distribution etc.

Meanwhile, in order to analyze FSS problems, an alternative procedure has to be followed. First, establish FSS models by calculating the initial design parameters of a unit cell with upper and lower PML layers. Second, define materials, same as antenna simulation. Next, for boundary conditions, besides PEC, PMC, periodic boundaries and PMLs must be defined. Calculation parameters and post processing are the same as antenna simulations.

In order to shorten the research time required, we used commercial FEM software package HFSS from Ansys for CAD and EM field analysis. (See Figure 3.1 for the interface of HFSS) Ansys HFSS is a mainstream FEM based solver package for EM structures from Ansys Corporation. The acronym originally stood for High Frequency Structural Simulator. It is one of the most popular and powerful EM simulation softwares, and among one of the earliest commercialized. Due to its highly mature algorithm, high simulation precision, and relatively high speed, it has been widely utilized in scientific research, technical designs, as well as other applications. When using HFSS for numerical design, the calculation precision and time is highly dependent on the size of the object and its mesh sizes. The finer meshes will result in more precise results, but requires longer computing time as well as larger RAM. As a result, during early simulation stages, it places high requirements on computers.

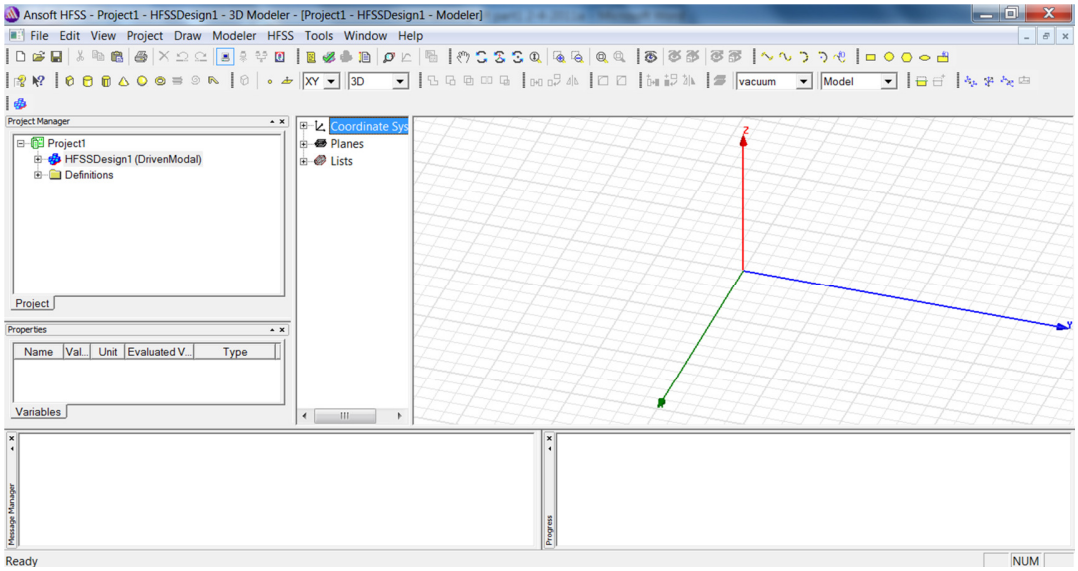

Figure 3.1 Interface of Ansoft HFSS

3.2.Numerical Modeling of Woven Antennas

3.2.1.Introduction

Over the past decades, woven antennas have drawn significant attention from researchers for their intrinsic flexibility, conformity, mount-ability, low manufacturing cost, and ease of fabrication. Various types of antennas made of textile materials have been developed during the past few years [28-35]. Most of these antennas are designed based on the assumption that woven antennas have the same radiation characteristic as microstrip antennas (MSA) and are designed and analyzed using conventional the MSA transmission line model. However, such an assumption has to be investigated with care because there are intrinsic differences between conductive woven conductive structure and PEC boundary. By introducing different weave patterns into the radiating patch, the woven

antenna has the capability of eliminating the fundamental mode of MSA while operating under higher order modes, with its performance changed dramatically from MSA.

The goal of this research was to reveal the effect of weave arrangement and crimp on the radiation mechanism of woven antennas. In this paper we fabricated a woven antenna using plain weave method and compared it to reference microstrip antenna (MSA). Prior to the antenna fabrication we also carried out finite element method (FEM) simulation using Ansoft High Frequency Simulation Software (HFSS) to confirm our findings.

The resonance characteristics of the antennas under test (AUT) are measured by a vector network analyzer. The radiation patterns of the AUTs are measured in a microwave anechoic chamber. The impacts of the plain weave configuration on radiation modes are discussed.

3.2.2.Materials

3.2.2.1.Non-conductive Yarns

The textile material we chose for this research is a generic polypropylene yarn acquired from Belton Industries. The yarn has a width of 2 mm and thickness of 0.1 mm. The standard configuration of the textile fabric is 9 picks per cm of 1000 denier polypropylene monofilament yarn according to qualifications for the American Association of State Highway & Transportation Officials (AASHTO) standardized Class 1 Stabilization standards.

3.2.2.2.Conductive Wires

In order to study the impact of weave configuration on antenna performance, a conductive wire with the same dimension of the non-conductive yarn was carefully chosen. The wire we chose was designed to be used as solar cell interconnecting wires (photovoltaic ribbon wire) acquired from Ulbrich Industries. It was a double side coated ribbon wire with 62% tin 36% lead and 2% silver soldering coating of 0.001-0.0015mm per side. The conductive wire was 2 mm wide and 0.1 mm thick, which is the same as the non-conductive yarn.

3.2.2.3.Dielectric Substrate

The substrate provides the dielectric between the antenna patch and the ground plane. The general requirements for the substrate include low electrical loss, homogenous thickness, low moisture absorption, and uniform electrical properties over frequency. For our proposed application, chemical resistance and resilience are also important. Accordingly, the dielectric substrate material we chose was a 1.72mm thick Rogers RT5880 high frequency laminate. It has ε_r of 2.2 with a loss tangent (tanδ) of 0.0009.

3.2.3.Antenna Design

In this study, higher order modes of the MSA are studied. To describe the higher order resonances, a cavity model in which the MSA resembles dielectric-loaded cavities needs to be used [2]. In this model, the MSA is defined as a cavity with length of L, width of W, and height of h. Since the height-to-width ratio is usually very small, the cavity is considered generating only transverse current density J_t at the bottom and top surfaces

underneath the patch, and the E field inside the cavity is considered constant across the patch. The fringing field close to the edges of the patch are approximated as constant and normal to the surface of the patch. As a result, no TE mode will be generated in the cavity mode. The side walls are approximated as having no tangential magnetic field component and thus are modeled as perfect magnetic conducting (PMC) walls. The resulting cavity model is defined by perfect electrically conducting (PEC) boundaries in the yz plane separated by h, PMC boundaries in the xz plane separated by W, and PMC boundaries in the xy plane separated by L, as shown in Figure 3.2, the yellow color represents conductive material, the gray color represents non-conductive material, as is the convention throughout the paper. The resonant frequencies predicted by the cavity model are given by

$$(f_r)_{mnp} = \frac{1}{2\pi\sqrt{\mu\varepsilon}}\sqrt{(\frac{m\pi}{h})^2 + (\frac{n\pi}{L})^2 + (\frac{p\pi}{W})^2} \qquad (3\text{-}1)$$

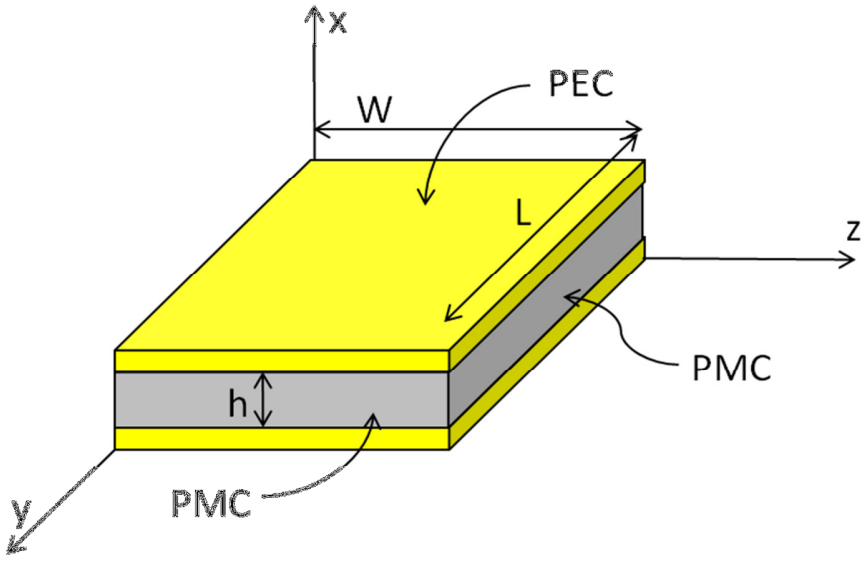

Figure 3.2 Boundary conditions of MSA cavity mode

The radiation mode of the MSA depends on the dimension of the radiating patch. For different cases of L, W, h arrangements, usually the fundamental and secondary modes are among TM^x_{010}, TM^x_{001}, TM^x_{020}, and TM^x_{002} as shown in Figure 3.3, respectively.

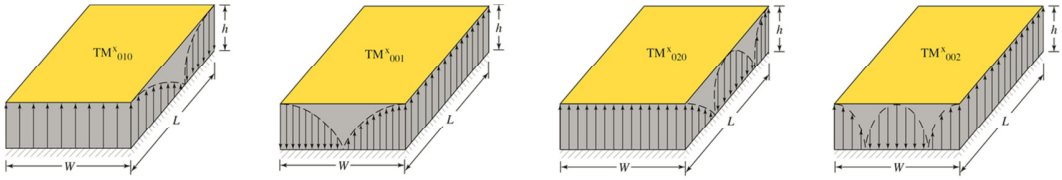

Figure 3.3 Resonance modes of MSA (a) TM^x_{010}, (b) TM^x_{001}, (c) TM^x_{020}, and (d)TM^x_{002}.

The parameters of MSA is designed based on the equations (3-2) and (3-3) assuming TM^x_{010} as the fundamental mode, taking into account the fringing effects

$$W = \frac{1}{2f_r\sqrt{\varepsilon_0\mu_0}}\sqrt{\frac{2}{\varepsilon_r+1}} \qquad (3\text{-}2)$$

$$L = \frac{1}{2f_r\sqrt{\varepsilon_{reff}\varepsilon_0\mu_0}} - 2\Delta L \qquad (3\text{-}3)$$

Where f_r is the fundamental TM^x_{010} mode resonance frequency. The width W determines the input impedance of the radiating patch and is carefully chosen so that one of the yarns in the warp direction can be used as quarter wave transformer to connect the patch to the 50Ω transmission line.

As for the antenna feed structure, we used a 50Ω microstrip transmission line and a microstrip quarter wave transformer in series to match the impedance of the microstrip patch to a SubMiniature version A (SMA) coaxial cable. The widths of the transmission line and microstrip transformer were computed using the microstrip transmission line formulas given in Balanis [2]. The final parameters of the MSA design are listed in Table 3-1, and the resulting scheme of MSA is shown in Figure 3.4 Design scheme of MSA

Table 3-1 Design summary of MSA

Microstrip	λ/4 Transformer	Feed Structure	Substrate
W=102.7mm	W_{qw}=2mm	W_{50}=5.24mm	W_{sub}=190mm
L=58mm	L_{qw}=32.9mm	L_{50}=10mm	L_{sub}=140mm

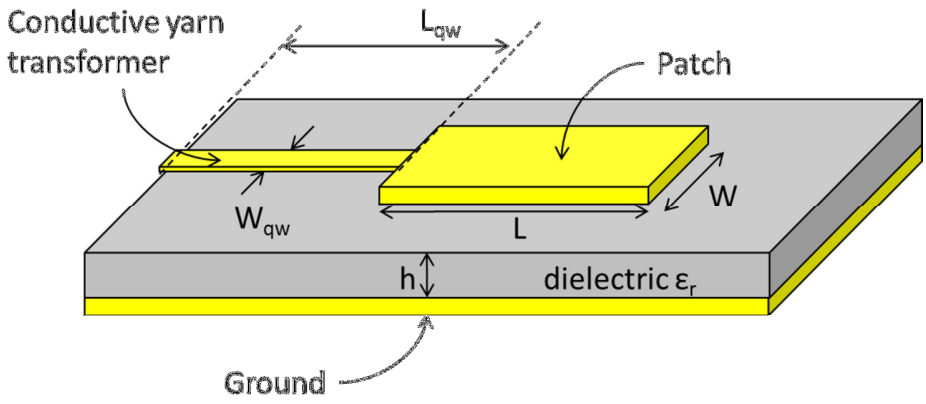

Figure 3.4 Design scheme of MSA

3.2.4.Antenna Manufacturing

The MSA is fabricated with copper single clad RT5880 board and adhesive copper foils. To fabricate the woven antenna, a plain weave process is carried out on a wooden loom, which is normal practice for textile product prototype manufacturing.

Since it is easier to manipulate the weft yarns, the radiating patch forming wires are woven from the weft direction. Before the weaving begins, the warp yarn in the middle is replaced with a conductive wire for antenna feed structure and the conductive wires are inserted as weft yarns. The resulting scheme of the radiating patch of the MSA and woven antenna are shown in Figure 3.5 and Figure 3.6 . After the radiating patch is woven, the

excessive yarns outside the radiating patch are trimmed off, and the dielectric substrate is attached to the patch using adhesives. Photographs of the MSA and woven antenna are shown in Figure 3.7 and Figure 3.8 respectively.

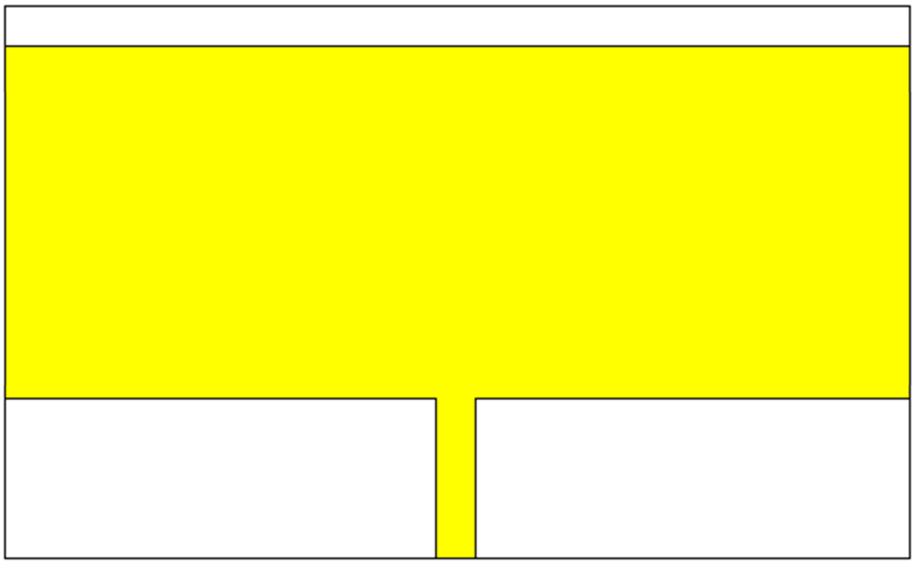

Figure 3.5 MSA design scheme.

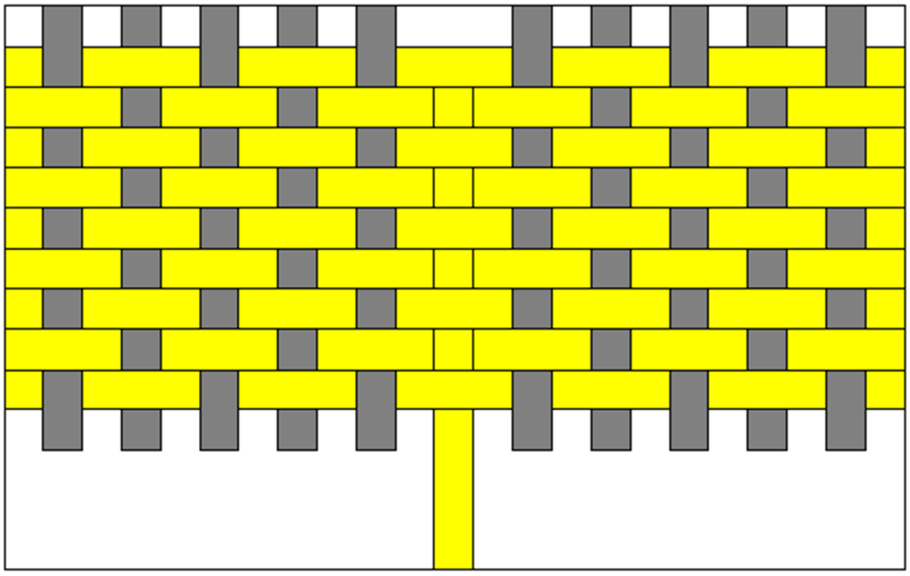

Figure 3.6 Woven antenna design scheme.

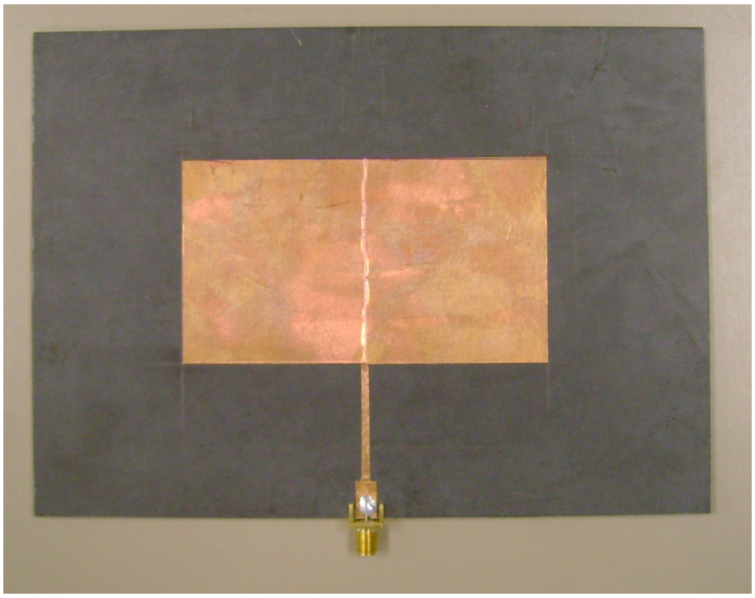

Figure 3.7 Picture of fabricated MSA.

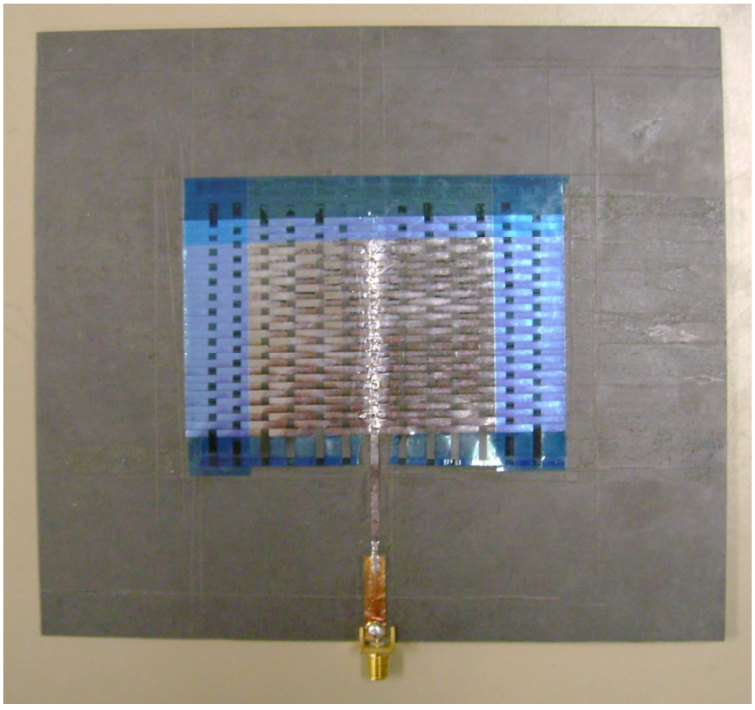

Figure 3.8 Picture of fabricated woven antenna.

3.2.5.Simulation and Measurement Results

In order to validate the antenna performance, we conducted full-wave FEM simulations using Ansoft HFSS. The antenna model of reference MSA is established with the 3d modeler of HFSS. The MSA model is relatively simple: for the radiation patch it has a feed structure, quarter wave transmission line, and square patch with dimensions listed in Table 3-1, plus dielectric substrate and ground plane. A waveguide port is added perpendicular to the patch as radiation source. An air box with radiation boundary is established to enclose the entire structure.

To confirm the simulation result, first we measured the S11 return loss of the woven antenna and MSA to find out possible correspondent radiation modes. A HP8753C vector network analyzer is used for S11 measurement. The data is extracted to a laptop computer using an Agilent 82357 USB/GPIB interface and Agilent Intuilink data capture software. First the simulated S11 of MSA is compared with the measured data to find out the corresponding resonances as shown in Figure 3.9. The measured S11 of woven antenna and MSA are shown in Figure 3.10.

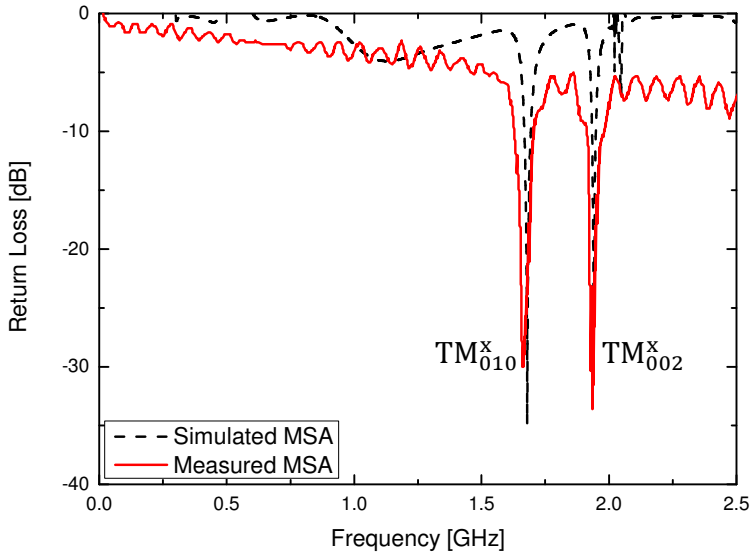

Figure 3.9 Simulated (solid) and measured (dashed) S11 return loss of MSA

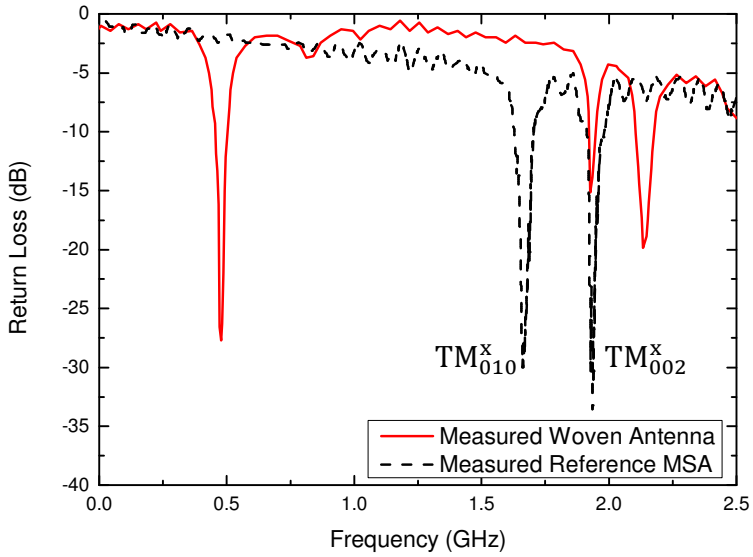

Figure 3.10 Measured S11 of woven antenna (solid) and MSA (dashed)

In order to study the effect of crimp on radiation characteristics, a woven antenna and a grating MSA are also modeled separately. The woven antenna is modeled with analytical curve sweeping, and the wires are modeled as a sine function of y in z direction with

0.1mm spacing between the wires. The lengths of wires are set the same as width of reference MSA, and the number of wires is chosen carefully to match the patch size of reference MSA. For the grating MSA, the patch is modeled as individual microstrips with the same size as the conductive wires in woven antenna and 0.1mm spacing in between, we call it grating MSA for convenience. The simulation models and the simulated S11 return loss are shown in Figure 3.11 and Figure 3.12 respectively. To confirm the simulation result, a grating MSA is fabricated as shown in Figure 3.13 and the measured S11 of the grating MSA comparing with woven antenna is shown in Figure 3.14.

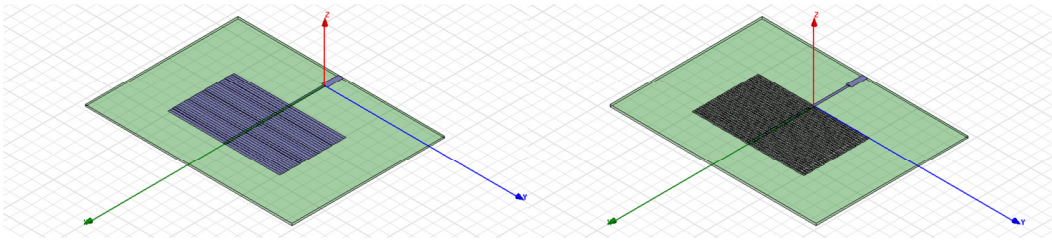

Figure 3.11 Simulation model of (a) grating MSA and (b) woven antenna

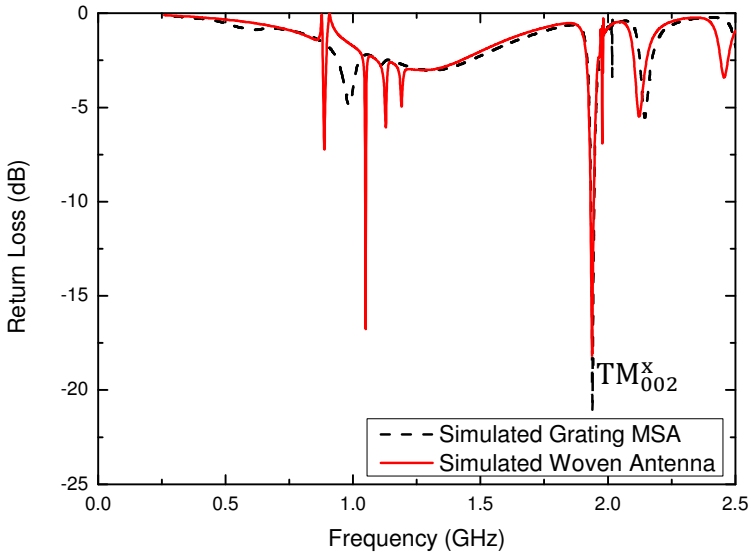

Figure 3.12 Simulated S11 of woven antenna (solid) and grating MSA (dashed)

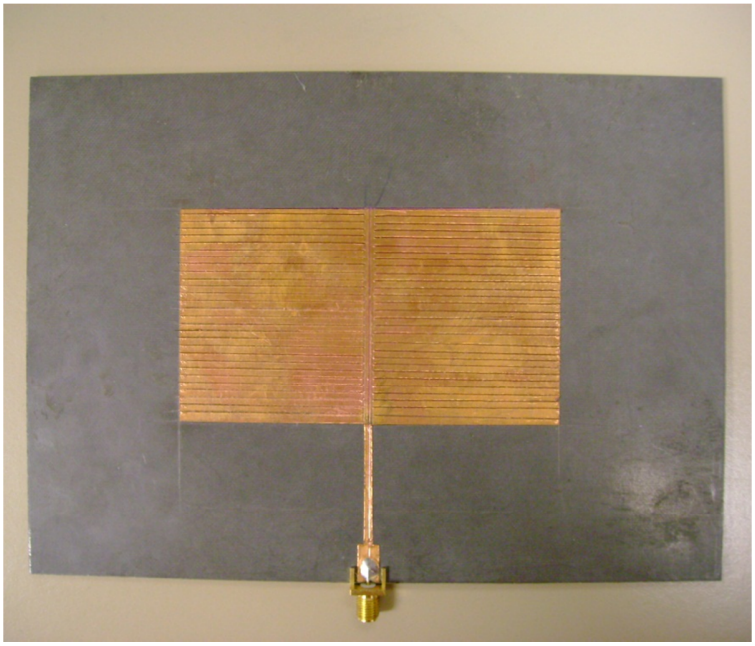

Figure 3.13 Picture of fabricated grating MSA.

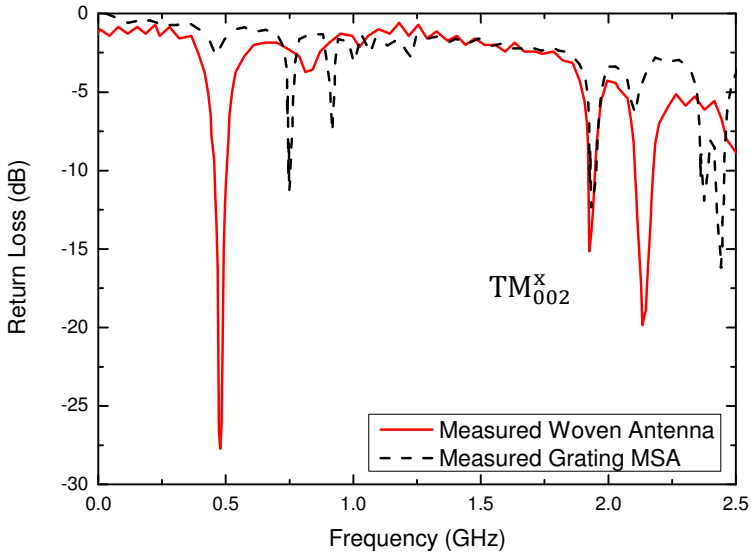

Figure 3.14 Measured S11 of woven antenna (solid) and grating MSA (dashed)

Next, we loaded the AUTs onto the Desktop Antenna Measure System (DAMS) in the anechoic chamber to acquire radiation patterns. An L-band horn antenna is used as source antenna and the HP8753C is tuned into continues wave mode and act as the power source. At the receiving end, a DAMS x100 turn table system is used as the testing platform. The AUT is connected to a power amplifier and then to an Agilent 34401A multi meter for signal reading. The data is collected by DAMS software for further processing. The entire experiment is set up in the anechoic chamber to minimize reflection and external interferences.

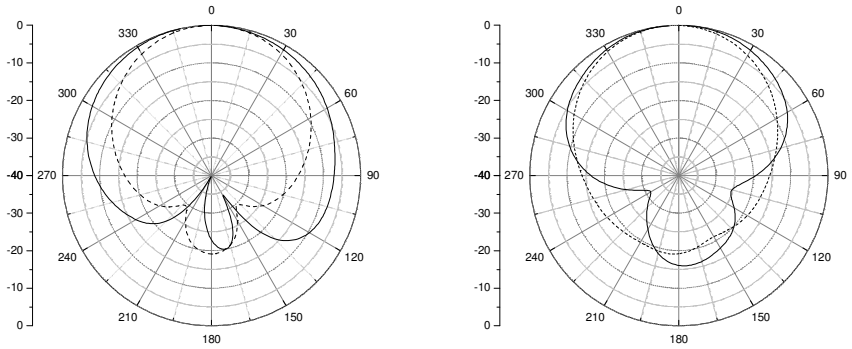

Figure 3.15 Simulated (solid) and measured (dashed) radiation pattern of MSA TM^{x}_{010} mode. (a) XZ plane. (b) YZ plane.

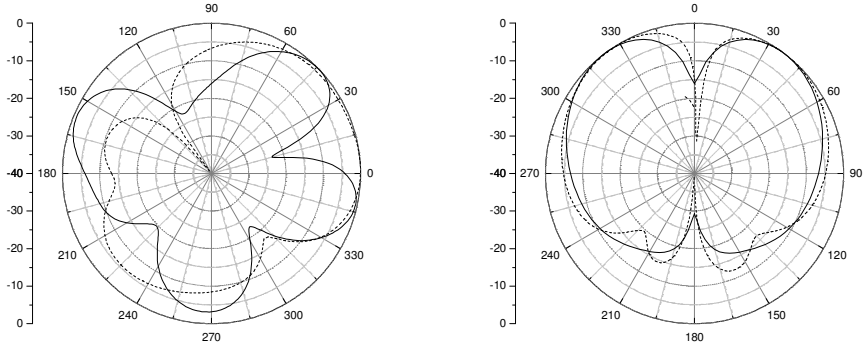

Figure 3.16 Simulated (solid) and measured (dashed) radiation pattern of MSA TM^{x}_{002} mode. (a) XZ plane. (b) YZ plane.

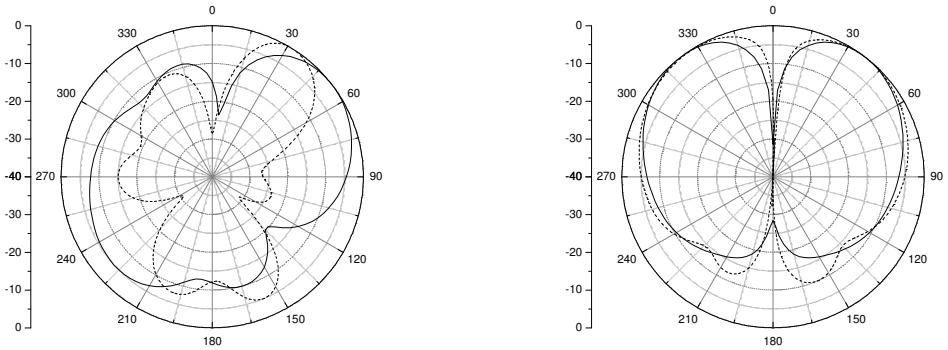

Figure 3.17 Simulated (solid) and measured (dashed) radiation pattern of woven antenna TM^{x}_{002} mode. (a) XZ plane. (b) YZ plane.

The simulated and measured radiation patterns of MSA TM^{x}_{010} mode, TM^{x}_{002} mode, and the woven antenna TM^{x}_{002} mode are shown in Figure 3.15 through Figure 3.17, respectively.

3.2.6.Discussion

Based upon the results, herein the radiation characteristic of the woven antenna is drastically different from the MSA. Figure 3.9 shows the dominant radiation mode of the MSA is TM^{x}_{010} and the next higher mode is TM^{x}_{002} as the cavity model predicted. However, the dominant mode of the woven antenna is shown to be TM^{x}_{002} mode instead of TM^{x}_{010}, as shown in Figure 3.10.

TM^{x}_{010} mode is generated by transverse current density J_t in Y direction. (Refer to Figure 3.2 and Figure 3.3). Continuous J_{ty} requires a continuous PEC boundary condition in Y direction, which is disrupted by the periodic crimps introduced by the weaving method. From the cavity model, the PEC boundary on top of the cavity is replaced with a periodic PEC and crimp boundary, the transverse current in the Y direction is disrupted by the crimps, while a tangential E-field is allowed in the openings, making the TM^{x}_{010} mode a prohibited mode. Meanwhile, the TM^{x}_{002} mode is generated by J_{tz} which requires a continuous PEC boundary in the z direction. Although there are open slots introduced by the crimp between the conductive wires, they remain parallel to the current flow, and since the size of the openings is electrically small, the J_{tz} current is undisrupted and TM^{x}_{002} became the preferred mode in woven antenna.

A careful examination of the crimp effect is made by comparing a grating MSA with a woven antenna. The simulation and measured results are shown in Figure 3.12 and Figure 3.14 respectively, which suggests the elimination of TM_{010}^{x} mode is common for both the grating MSA and the woven antenna. However, the crimp introduces strong resonances below 1GHz, which is not present in the grating MSA. The simulated result shows a -7dB resonance of woven antenna at 886MHz and -5dB resonance of grating MSA at 979MHz. However, the measured result shows -28dB resonance at 478MHz for the woven antenna and the grating MSA has a -11dB resonance at 745MHz. The crimps in the structure have drastically changed the radiation mechanism of the antenna, and allow a highly efficient mode at 478MHz, which is much lower than cavity model prediction. This result appears to be a unique behavior of woven antenna. The result suggests that a woven antenna is able to replace an MSA nine times its size, $248 \times 210mm$ MSA compared to $103 \times 58mm$woven antenna for the same design with the same efficiency. The woven antenna is even superior to a Planar Inverted-F Antenna (PIFA), which is widely used in cellular designs nowadays, in that PIFA operates one quarter the size of MSA with the trade off of lower efficiency and more sophisticated structure [2].

Although the FEM simulation is inaccurate, the simulation can still give some insights into its radiation mechanism. The simulated radiation pattern of 886MHz is shown in Figure 3.18. The radiation pattern suggests a 45 degree main lobe in the xz plane which is different from any MSA model predictions but similar to microstrip slot antenna. The travelling wave TE^{x} mode of the slot antenna allows the main lobe direction to be pointed in any direction, from broadside to end-fire, by varying the width of the slots [4]. Such

behavior can also be explained with an artificially electromagnetic surface. An artificial soft surface prevents certain modes of surface waves from propagating in the stop band. In this case, the grating strips are in the transverse direction, thus the TM^x mode wave is prohibited, while the TE^x mode surface wave becomes a leaky wave and causes the radiation pattern shown in Figure 3.18. Further investigation is needed to confirm this hypothesis.

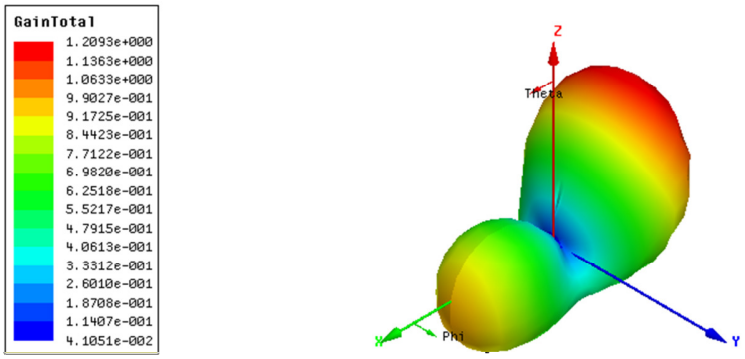

Figure 3.18 Simulated woven antenna radiation pattern at 886MHz

3.2.7.Conclusion

The characteristics of MSA and woven antennas were measured. The simulation and experimental results confirm that the radiation characteristic of the MSA has been changed dramatically by the incorporation of plain weave. The weave configuration eliminates the TM^x_{010} mode, while it preserves the TM^x_{002} mode. The weave structure also enabled the woven antenna to operate in an unknown mode, one ninth of the size of a conventional MSA. It is possible that the grating weave configuration introduced an electromagnetic

bandgap structure, preventing TM mode surface mode, and made the antenna to operate in leaky-wave TE mode as microstrip slot antenna.

3.3.Numerical Modeling of Woven Frequency Selective Surface

3.3.1.Introduction

Artificial surfaces have numerous applications in antenna design and microwave engineering [36]. Among these, the frequency selective surface (FSS) is considered one of the most promising, and the interest in the integration of FSS into composite materials has led to various kinds of frequency selective fabric structures [37-44]. An FSS is an artificially engineered surface, comprising of periodic metallic structures with selective EM wave transmission or reflection characteristics. Research into frequency selective fabric has inspired many new applications, especially in new generation wireless communication systems and radar systems. However, most of the current research has been focused on microwave absorption properties of the resulting composite material. In this paper, we suggest a new class of FSS that can be manufactured with the weaving process, which gives rise to novel devices including self-supported standalone FSS. Some other advantages of woven FSS include: relatively light weight, flexible (conformal) substrates, and simple integration into other textile or composite products. Therefore FSS formed of special fabrics can be considered as a substitute for conventional printed circuit devices.

In this work, a textile FSS has been studied using the numerical analysis method for the first time. The goal of this research was to reveal the effect of weave arrangement and crimp on the EM wave interaction mechanism of textile FSS. We modelled a textile FSS together with a conventional aperture type FSS using a commercial finite element method (FEM) simulation package - Ansoft High Frequency Simulation Software (HFSS). HFSS has been proven to be an efficient and accurate way to calculate EM field under various conditions. Based on the simulation result, the impacts of the plain weave configuration on FSS performance is discussed.

3.3.2.Floquet's Modal Analysis

Due to its periodic nature, FSS may comprise patch type or aperture type. The aperture type FSS is studied herein for the ease of fabrication using the weaving technique. To model the periodic FSS structure, one can take advantage of Floquet-Bloch theorem. In this study we used periodic boundary conditions in HFSS, which essentially set up a Bloch boundary along the unit cell walls. The fields at one wall of the cell are related to the fields at the opposite wall by the wave vector. A frequency sweep can be set up to scan the entire frequency band of interest, which yields scattering parameter data for FSS performance analysis.

3.3.3.Simulation Model Setup

The geometry of the aperture FSS and textile FSS are shown in Figure 3.19 and Figure 3.20, respectively. The aperture FSS structure consists of periodic apertures 2.5×2.5mm in size and placed 2.5 mm apart uniform along x and y direction. The textile FSS consists

of two types of yarns, conductive copper yarn and non-conductive Teflon yarn, both of which are 1.25mm wide and 0.05mm thick. The plain weave structure is modeled with an analytical curve, sweeping with the yarns, and modeled as a sine function in the z direction. The arrangement of the copper and Teflon yarns is a two by two repeating pattern in both warp and weft directions, thus making a 2.5 non-conductive aperture in the middle of the unit cell, matching that of the conventional aperture FSS. The non-conductive Teflon yarns are hidden in Figure 3.20 to show the copper yarns more clearly.

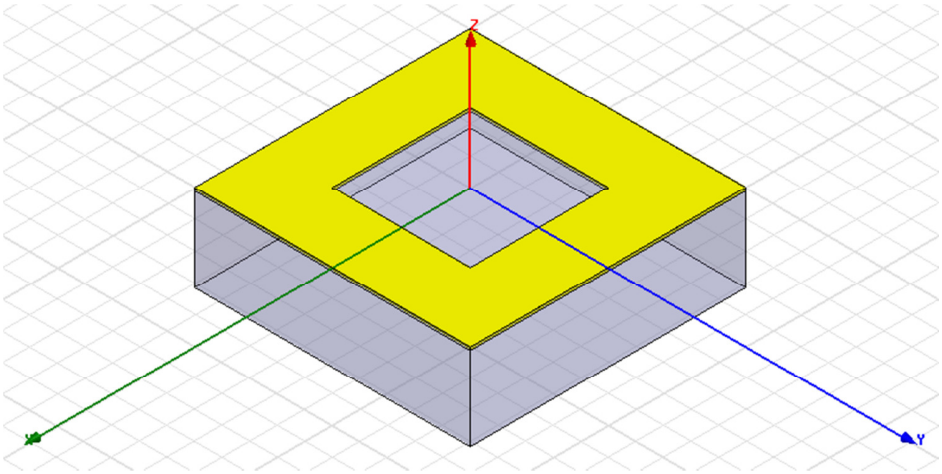

Figure 3.19 Model setup of aperture FSS

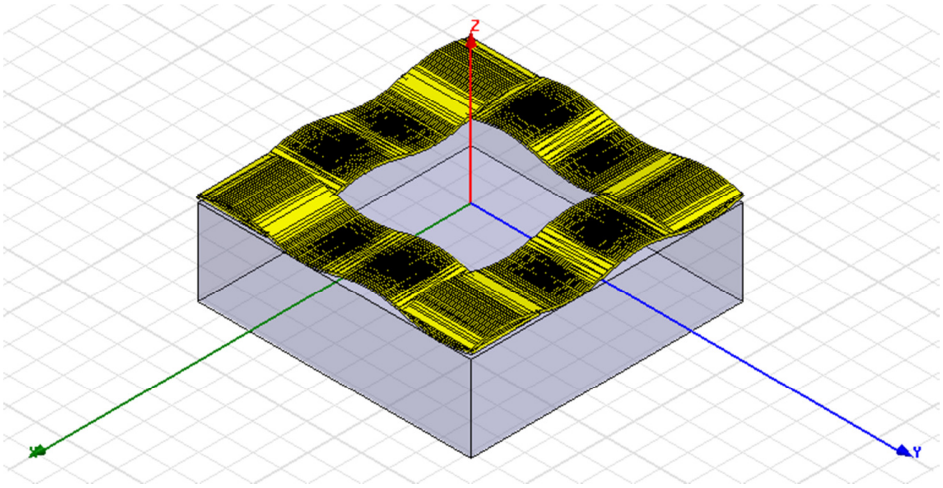

Figure 3.20 Model setup of textile FSS

3.3.4.Simulation Results and Discussion

The simulated S-parameter (S11 and S21) results of the aperture and textile FSS are shown in Figure 3.21 and Figure 3.22. The primary interests in this case are the S-parameter results, which represent the reflection from and transmission through the FSS. The results show significant differences between the aperture and textile FSS. From Figure 3.21, the transmission of textile FSS was almost completely blocked at 14.5 GHz, as seen from the Textile FSS S21 of about -54 dB, and the reflection was almost complete, as seen from Textile FSS S11 of 0 dB. On the other hand, the first reflection of aperture FSS was not present until 24.2GHz. Moreover, the aperture FSS behaves like a high-pass filter (reflect incident wave <10GHz) as FSS theory predicted, but the textile FSS appears to be low-pass filter, which is contrary to the theory on an aperture type FSS.

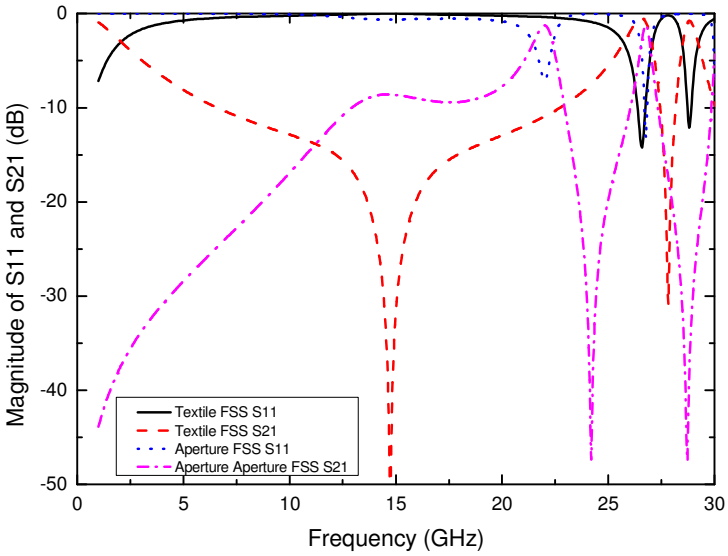

Figure 3.21 Magnitude of S11 and S21 of textile FSS and Aperture FSS

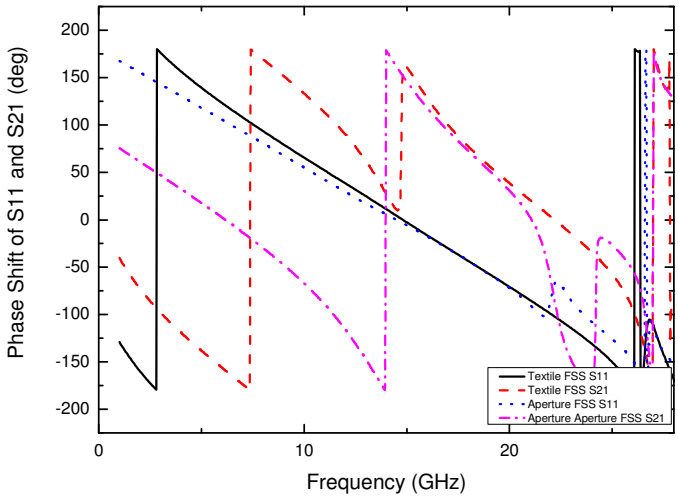

Figure 3.22 Phase shift of S11 and S21 of textile FSS and Aperture FSS

Moreover, the dependence of the FSS resonant frequency on the angle of the incident plane wave is of interest. The incident angle stability of both aperture and woven FSS is investigated as shown in Figure 3.23 through Figure 3.26.

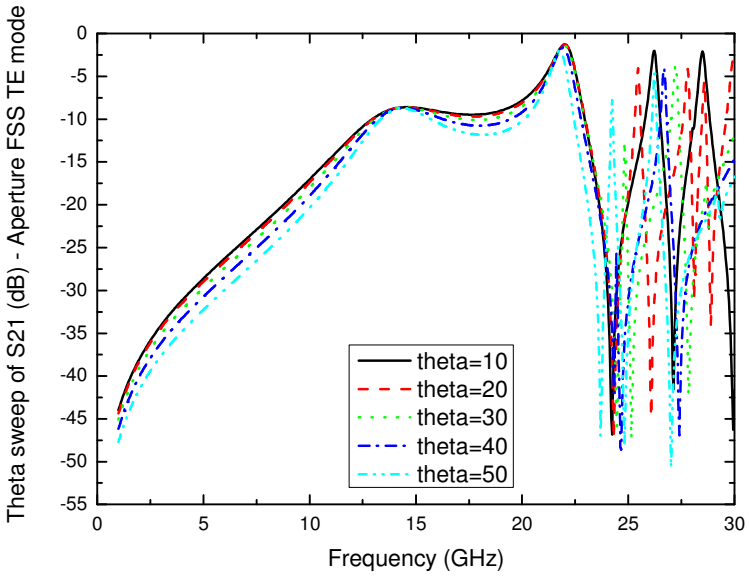

Figure 3.23 Aperture FSS incident angle dependence TE mode

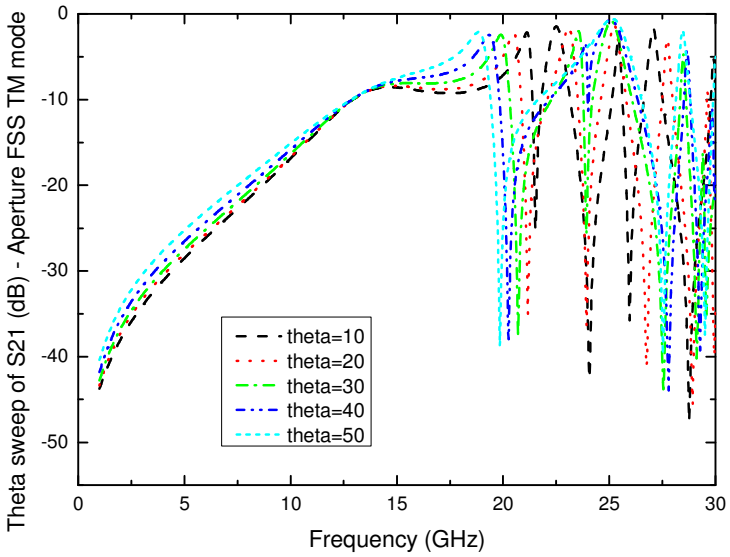

Figure 3.24 Aperture FSS incident angle dependence TM mode

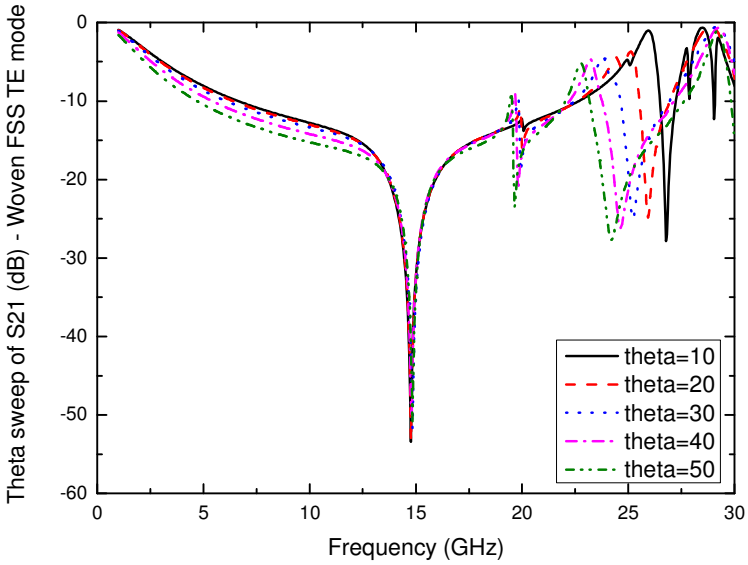

Figure 3.25 Woven FSS incident angle dependence TE mode

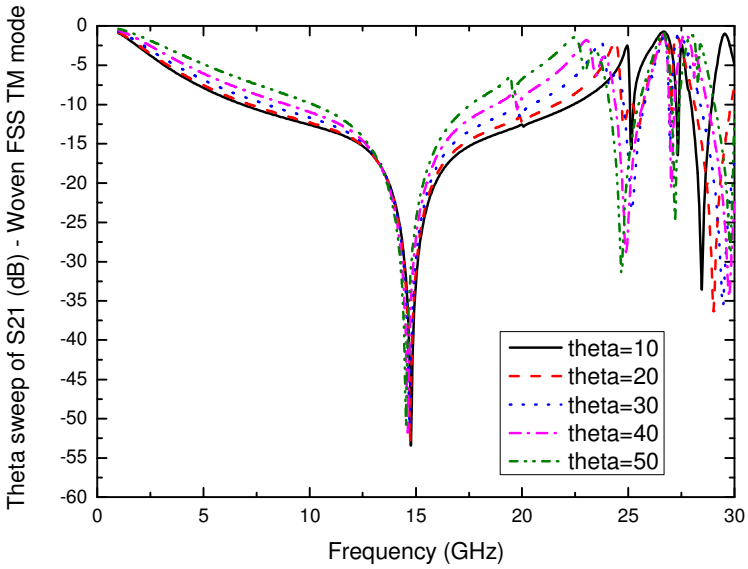

Figure 3.26 Woven FSS incident angle dependence TM mode

For the aperture FSS, the transmission coefficient (S21) of the TE mode (24GHz) shows greater dependence on variation of the scan angle in theta than the TM mode (24GHz) does. This is to be expected since the shape of the aperture changes to rectangle

when incidence is not normal. For the TE mode, the E-field is perpendicular to the width of the rectangle, which is varying with scan angle, thus the frequency of the TE mode transmission coefficient mode varies with scan angle. While for the TM mode, the E-field is parallel to the width of the rectangle, so the amplitude instead of the resonant frequency changes with scan angle. Either way, this incident angle dependency is undesirable for FSS applications.

On the other hand, for the textile FSS, both the TE and TM mode at 15GHz are independent of scan angle. The incident angle stability is possibly due to the sine and cosine cross section of the textile aperture. The complimentary curvatures in the aperture cross section have a similar effect of ring resonators which is well known for incident angle stability. Further investigation needs to be carried out including the investigation of an equivalent lumped element circuit model.

3.3.5.Conclusion

A new type of textile FSS with unique EM properties has been simulated using the FEM method. It is characterized by an inverted filtering behavior and much lower fundamental resonant frequency than its aperture FSS counterpart. The incident angle stability of textile FSS is also comparable with ring resonators. It can be easily manufactured by weaving technology and even indicates the feasibility of standalone FSS manufacturing. The previously unpredicted EM behavior of such a material might lead to further development of the FSS theory and novel applications including electromagnetic textiles and artificially magnetic conducting textiles.

3.4.Numerical Modeling of Textile Artificial Magnetic Conductor

3.4.1.Introduction

High Impedance Surface (HIS) such as the Sievenpiper mushroom is capable of providing in-phase reflection for plane wave incidence. This is an important characteristic of a perfect magnetic conductor (PMC), and so HIS is also called Artificial Magnetic Conductor (AMC). Due to its surface wave suppression characteristic [21], it is widely studied in the applications of low profile antennas [45], high performance IC filters [46], and high Q resonators [47].

There is also much interest in the integration of wireless communication systems into wearable products, which lead to various kinds of body worn antenna structures [28, 29, 31, 32, 34, 35, 48-54]. It is a logical to attempt to integrate AMC structures into body worn antennas to improve their performance. Bashir et al. [33] has suggested flexible frequency selective surface (FSS) by incorporating HIS into fabric structures. However, the work is done by using fabric felt material as substrate and the traditional printed circuit technique (PCB) technique to form the periodic pattern, thus is not a purely textile AMC/AEC.

In this paper, we address the impact of fabric nature on the electromagnetic performance of textile AMC/AEC structures. Yarns in a piece of fabric are periodic in nature. To the author's best knowledge, study of textile AMC/AEC structure has never been done. Arranging conductive fibers in the weft direction only and attaching the fabric to a suitable substrate results in an AMC/AEC composite surface. The comparison between periodic conducting-strip grating and a woven AMC/AEC surface was studied for the first time. Based on this study, several distinct phenomena regarding weave-introduced crimps

were observed which lead to conclusions regarding the feasibility of textile AMC/AEC and other electromagnetic textiles.

3.4.2.Eigenmode Analysis

To study the behavior of a textile AMC/AEC surface, a finite-element model with detailed weave geometry of the textile surface is included. In the FEM model, the structure of the unit cell is discretized, and the electric field at all points on the grid can be reduced to an eigenvalue equation, which may be solved numerically. In this study we used periodic boundary conditions in HFSS, which essentially set up Bloch boundary along the unit cell walls. The fields at one wall of the cell are related to the fields at the opposite wall by the wave vector. The calculated eigenvalue is essentially the allowed frequencies for a particular wave vector. The procedure can be repeated for each wave vector to produce the entire dispersion diagram. The structures analyzed herein are a PEC strip grating and a woven grating, shown in Figure 3.27 and Figure 3.28 respectively. The straight strips and woven strips are infinitely long and uniform along the x direction, and periodic in the y direction. The lattice constant was 5 mm, the strip width is 2.5 mm, and the substrate thickness is 1.8 mm.

The textile AMC/AEC structure consists of two types of yarns, conductive copper yarn and non-conductive Teflon yarn, both of which are 1.25mm wide and 0.05mm thick. The plain weave structure is modeled with analytical curve sweeping with the yarns modeled as a sine function in the z direction. The copper and Teflon yarns are inserted repeatedly in weft direction to form the grating, and the warp has only Teflon yarns to form

the plain weave patch. The Teflon yarns in Figure 3.28 are hidden in order to better show the copper yarn structure.

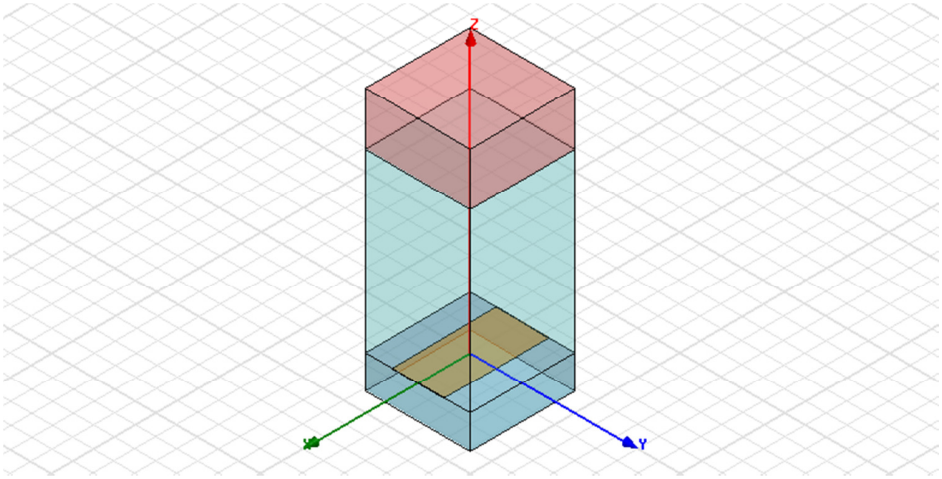

Figure 3.27 Model setup of PEC strip grating

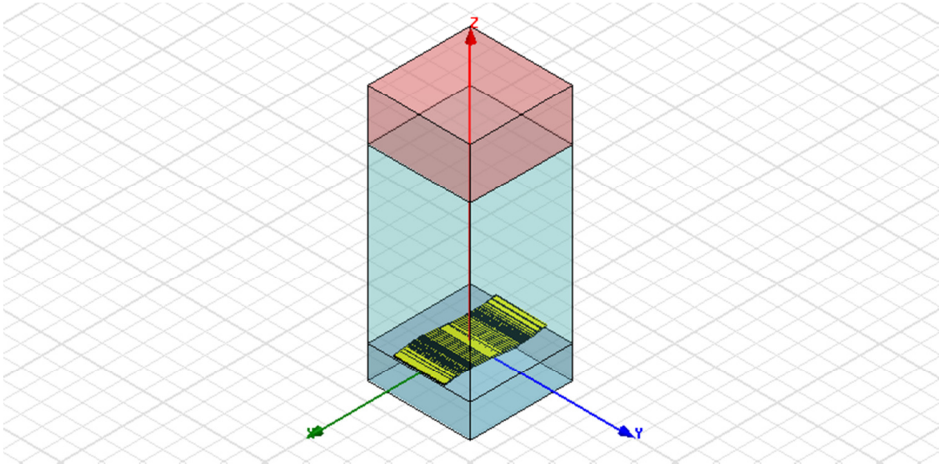

Figure 3.28 Model setup of woven strip grating

3.4.3.Numerical Results and Discussion

The primary interests in AMC/AEC study are the dispersion diagrams, which represent the EBG of the AMC/AEC structure. A dispersion diagram is a plot of the propagation constant versus frequency. It indicates how much phase shift a material has at

a given frequency. For background on Brillouin zone and details of how to generate dispersion diagram, please refer to Appendix B. The simulated dispersion diagrams of the grating AMC/AEC and textile AMC/AEC are shown in Figure 3.29 and Figure 3.30, respectively.

For the grating AMC/AEC, the band gap between first TM and TE mode is clearly shown from Γ to X and M to Γ, which suggest the structure is AMC for these wave vectors in the Brillouin zone. However, the bandgap collapsed from X to M, which suggests the structure is AEC for these wave vectors. For the textile AMC/AEC, the behavior of Γ to X and M to Γ are the same as the grating AMC/AEC. However, for X to M, the bandgap does not collapse, which means the textile AMC/AEC is really an entire AMC structure. In other words, by incorporating a weave pattern into a grating structure, the 1-D EBG is transformed into a 2-D EBG, meaning it is possible to reproduce the behavior of the more complicated Sievenpiper mushroom with a simple weave pattern.

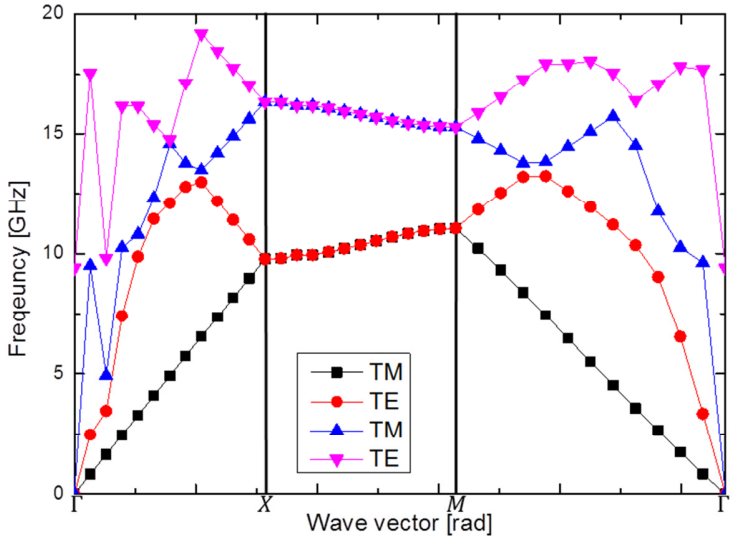

Figure 3.29 Dispersion diagram of grating AMC/AEC

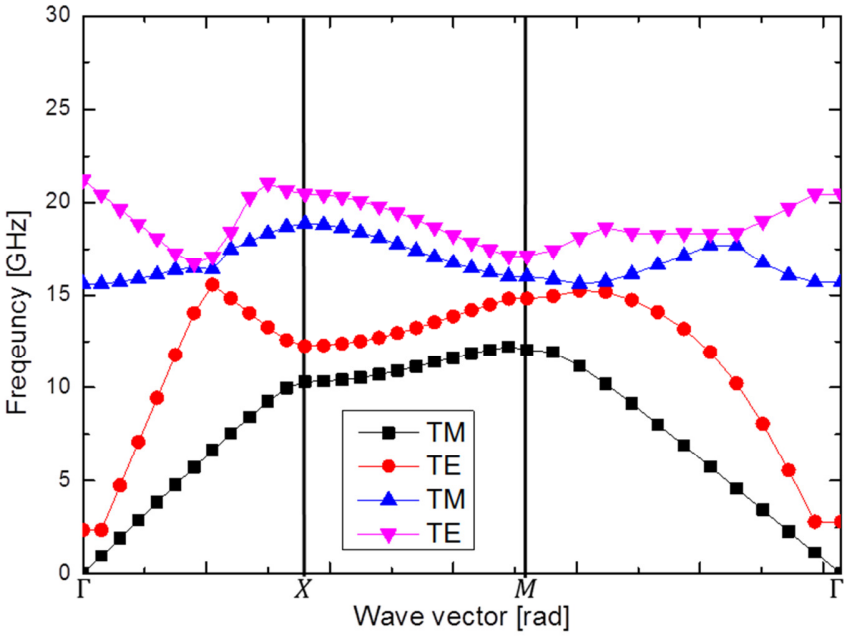

Figure 3.30 Dispersion diagram of textile AMC/AEC

3.4.4.Conclusion

A new type of textile AMC/AEC structure with unique EM properties has been simulated using the FEM method. It is characterized by having a 2-D EBG dispersion property on a 1-D periodic structure, and is able to turn an AMC/AEC structure into a full AMC structure. The simulated textile structure can be manufactured easily using weaving technology, providing the feasibility of pure textile AMC/AEC structure by incorporating the conductive yarns into a fabric dielectric substrate. The discovery of such unique EM behavior of the novel textile material might lead to further development of AMC theory and novel applications including electromagnetic textiles and flexible low profile high performance textile antennas.

Chapter 4.Emergency Communication Network

4.1.Introduction

In recent disasters such as hurricane Katrina, and the Wenchuan and Haiti earthquakes, we have witnessed great losses of human life due to lack of communication. Many sources emphasize that the most common problem in disasters is the deficiency of communication, equipment, and ultimately the ability to respond [55-59]. Pursuing a solution to this recurring problem was the inspiration to develop this project.

The function of communication networks to disseminate reliable information to the public, and enable the survivors to be connected to the "outside" world is critical during catastrophes [56]. Because transportation and power infrastructures are often damaged or destroyed during such times, it is impossible to restore the entire communication infrastructure immediately. Meanwhile, the first responders primarily acquire critical information from 911 calls, and are required to communicate quickly because their reaction speed means life or death to those in danger [56, 59]. Thus a rapidly deployable, easily reconfigurable, low power and low cost ECN that can provide temporary bandwidth to physically breach the communication gap is highly desired for such relief effort. Wireless sensor network (WSN), enabled by the recent advances in electronics, networking, information processing, is a promising technology toward the solution of an effective ECN.

A WSN featuring air-drop enabled nodes that can be distributed to any terrain promptly was investigated. With its performance and protocols dedicated for emergency text messaging service, a reliable emergency network among survivors and first responders can be established to improve emergency management effectiveness.

4.1.1.Impact on Humanity

Technology is best administered when it involves helping people, especially those in danger. The project addresses primarily the need for sustainable communications during disaster. In the event of a catastrophe, access to reliable communication systems is critical for the survivors. During Hurricane Katrina, much of the wireless and landline network infrastructure was destroyed or severely damaged, resulting in an overload of the remaining infrastructure as first responders, and rescue personnel, and the general public were all attempting simultaneous access. Moreover, the failure of backup 911 networks resulted in many unanswered emergency calls which confused the public about the relief effort while leaving life threatening situations unresolved.

The proposed approach provides rapid-deployable wireless communication capability during an emergency until the public communication infrastructure can be systematically restored. In this study, a WSN prototype that can be deployed to the affected area within hours by aircraft is designed. The WSN nodes will form a self-organized text messaging network, disseminate public safety information, and relay text messages among the survivors and responders. By re-establishing communications, capable survivors will also be enabled to assist in rescue effort before responding force arrives.

The solution could provide a reliable emergency communication method among survivors and first responders. The system will increase people's confidence when facing

disaster, increase awareness among survivors and responders, and relieve anxiety and combat rumors, thus improving morale in affected communities. Local and national government agencies can make more efficacious and informed decisions. Finally, and most importantly this communication system can save people's lives.

4.1.2.General Solution

The developed prototype involves the construction of a novel, rapidly-deployed, ultra-low power, distributed wireless communication network utilizing recycled post-consumer products and off-the-shelf components. The solution could enable survivors to communicate critical, lifesaving information with emergency responders via text messages using this network. The solution involves a multi-disciplinary scientific and engineering approach, combining electrical, computer, mechanical and textile engineering in an innovative way.

How it works: As soon as initial report of disaster is received, thousands of the communication nodes can be loaded on aircraft within minutes and air-dropped to the affected area. The air-dropped nodes will form a self-organized network to provide SMS service to the area. Based on the SMS feedback, humanitarian aid as well as additional nodes can be effectively distributed according to need.

The benefits of this concept are as follows. First, this approach facilitates saving of lives by serving as an interim communication network to quickly restore wireless communications during a time critical event. Next, the concept utilizes standardized components and works well with existing infrastructure, i.e. relief agencies are familiar with airborne relief methods. This system can be easily deployed over a large area from aircraft and utilized by existing cell phones with text messaging. Finally, the scale and

topology of the network are versatile such that they can be adapted to any emergency event.

SMS has become an overwhelmingly popular method of mobile communication nowadays (~5 billion cell phones worldwide); therefore utilizing SMS eliminates special training required for the survivors to operate the interim system. Moreover, unlike walkie-talkies and conventional landline telephones which may be left unanswered, text messages will be stored in a responder's cell phone memory, thus not easily ignored. The text messages from the survivors can also help the first responders, local and national governments in assessing the damage and dispatching aid efficiently.

The ultra-low power feature of the WSN node ensures full capacity communication for over two weeks with a single AAA battery. By adding solar-cells and rechargeable batteries, an energy harvest interface can ensure the service be extended almost indefinitely if needed. The WSN node prototype is designed to be fabricated with post-consumer products including recycled soda bottles.

The solution comprises the following modules: WSN node, GSM, power harvest, pneumatic control, multi-functional tether, and protective shell and base. The WSN node module comprises the fundamental elements forming the backbone of the WSN radio link and provides a backhaul of text message data to the sink node. The GSM module provides "Um" radio interface to the mobile users, allowing users to register with the emergency network for peer-to-peer or cell broadcast text messaging. The power harvest module integrates off-the-shelf rechargeable batteries, solar panels, and onboard voltage regulators to sustain system operation under varying conditions. The pneumatic control module utilizes off-the-shelf hardware to fulfill safe descending while providing antenna elevation

thus increasing communication range. The multi-functional tether facilitates balloon filling, power transmission, and load carrying between the balloon and base. Such a multi-functional tether is developed to connect the balloon, transmitter, and enclosure. The protective shell and base module provides supporting hardware surrounded by impact absorbing polyurethane foam and is also designed to act as an anchor to the ground by arranging the heavy components appropriately.

Based on testing, the developed WSN node will provide critical time-sensitive information to rescue responders and help save lives amid disaster and crisis. A computer aided imaginary deployment of the system is shown in Figure 4.1.

Figure 4.1 Wireless emergency communication network concept

4.2.Overall System Design

When catastrophic disaster strikes, the quickest way to deliver external responding force is by airborne methods [55]. An airborne communication network at this time is one of the best ways to relieve the communication needs of the people affected and the local

first responders for situation assessment. An airborne cellular communication network in such a situation is most desirable due to interoperability, wide spread availability, and ubiquity. Deaton et al. have suggested an ACN, which has a cell phone BTS loaded on aircraft to fly over the affected area and provide communication services [60]. However, the feasibility of such a solution for large scale disasters needs further investigation. First of all, a single aircraft will not be able to cover the affected area. For example, during Hurricane Katrina, Federal disaster declarations covered 233,000 km^2 of affected area in U.S. However, the ideal coverage of a WC-130 is 730 km^2 according to Deaton, et al [60]. In order to service the entire affected area, a fleet of over 300 aircraft need to be prepared and deployed when the hurricane hits. The cost for modifying aircraft, fuel, pilots and crew is significant. Therefore the ACN solution can only support emergency communication for small areas and relatively short periods of time.

Although ACN is not economically preferred, airborne methods are still the quickest and at times the only possible way to get help into the affected area. As a matter of fact, the C-130 Hercules has participated in countless humanitarian aid operations and has far superior performance especially in fierce weather conditions. The Lockheed WC-130 Weatherbird is configured with palletized weather instrumentation for penetration of tropical disturbances and storms, hurricanes and winter storms, and will be able to provide real-time humanitarian aid under virtually any weather condition. In our project, we propose to utilize specially designed air-drop WSN relay nodes in an airborne deployable form to provide emergency communication capability. Clusters of the WSN relay nodes can be loaded on a C-130 and precisely delivered to the affected area quickly. The nodes have all the circuitry built in a protective shell for weather proofing. It also employs a

multi-functional tether and helium balloon for safe descending and antenna elevation. Once dropped from the carrier, the balloon on the node will start to inflate and slow the descent. The helium tank, pneumatic valve, and other heavy components are built into the bottom compartment of the protective shell, while the communication module and solar panel (optional) will be attached to the balloon.

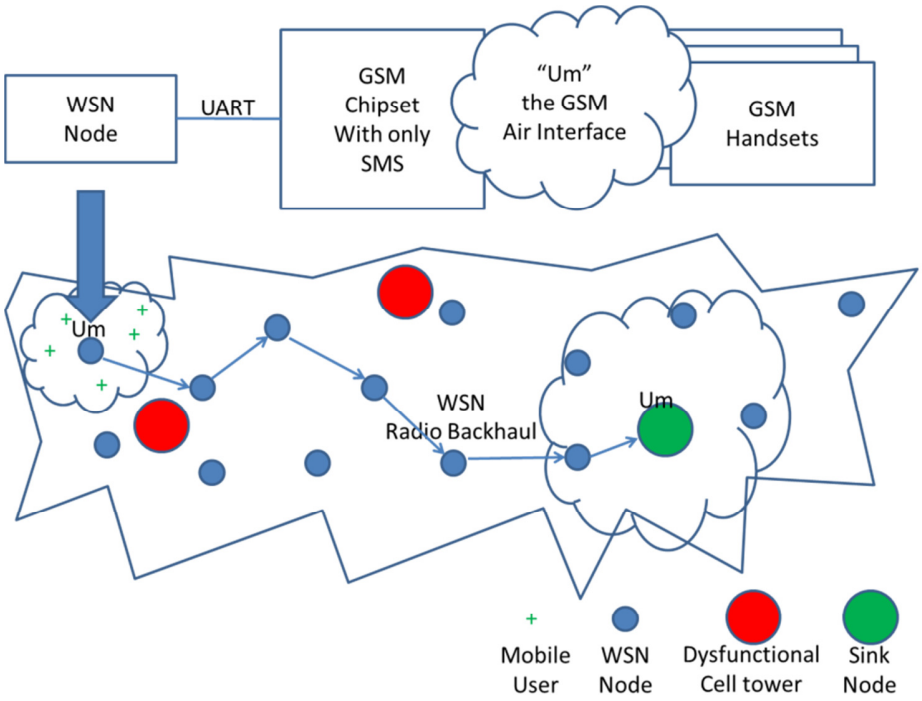

Figure 4.2 Overall emergency communication system architecture

Once landed, the WSN node will remain aloft at 20 feet above ground (lower than power lines) by the balloon for increased communication range. The tether prevents the balloon from being blown away by the wind and protects the connecting components. The WSN nodes will automatically form self-organized networks and gather SMS from GSM users and send them through the WSN to the sink node which will have connection to the public network. Please see Figure 4.2 for proposed overall system architecture.

4.3.Wireless Sensor Network Basics

Recent advances in low-power highly integrated digital electronics, microprocessors, and low-power radio frequency (RF) technologies have created low cost, low-power, and high performance devices that enable battery operated wireless signals transmission over long distances. With conventional data acquisition methods evolved from single wired mode to highly integrated, miniaturized, automated, and interconnected modes, these devices have drawn significant attention from researchers. They have integrated sensor technology, embedded computing, distributed information technology, and telecommunication technology. They could cooperatively and in real-time monitor, sense, and gather any information about the environment or an object under test, process this information, and convey them to the end users.

Wireless Sensor Network (WSN) is typically a self-organized network. It bloomed in late 90s, and can be applied to national security, environmental monitoring, traffic control, modern logistics, medical care, smart homes and many other fields. It has great potential for improving people's lives. WSN has become a new hot topic since then and will impact the way people live in the near future.

4.3.1.WSN System Structure

4.3.1.1.WSN Networking Structure

WSN is typically composed of a sensor node, sink node, and management node. A great number of sensor nodes randomly scattered inside or around the sensing field, form a network using self-organize capability, real-time monitoring and capture of information about objects. They send data back to the sink node through multi-hopping or other

mechanisms. The data can be processed during transmission, and then passed to the internet or a satellite to the management node. The end user can configure and manage the whole sensor network remotely, setting monitor tasks or change objectives on the fly. A basic WSN network structure is shown in Figure 4.3.

Sensor nodes are usually micro embedded systems, they have very limited processing power, memory storage and communication capability. They are usually equipped with a small battery, a radio transceiver, and a microprocessor used to control and process wireless data packages. The hardware and software of sensor nodes are the key research area of WSN. On the other hand, sink nodes usually have better processing power, memory storage, and communication capability. They may have connectivity to an external network such as the internet, implement interconnectivity between different protocols, disseminating tasks to the sensor nodes, and convey the gathered data to external network.

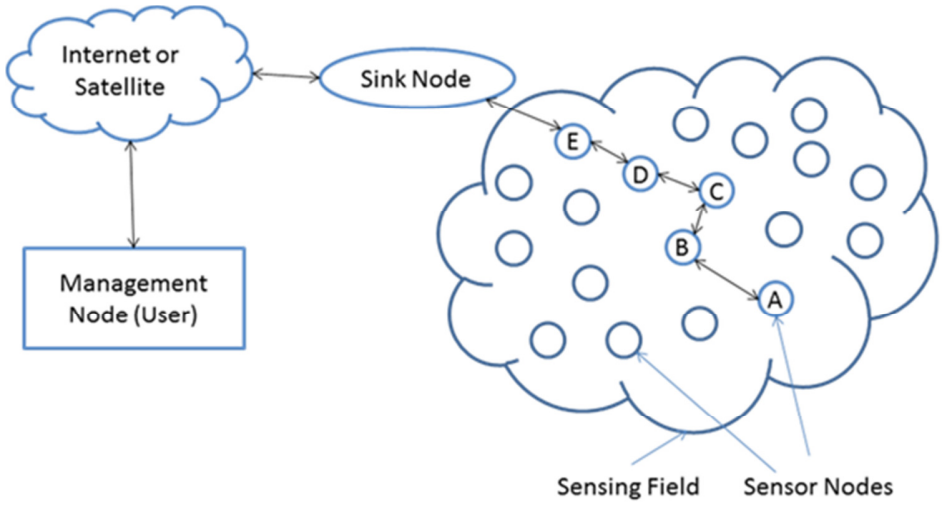

Figure 4.3 WSN network structure

4.3.1.2.WSN Sensor Node Structure

WSN has emerged as an independent computer network, and its basic unit is the node. Every node has its own sensor unit, processing unit and communication module. The functions of each node are to sense data, process data, and transmit data. A sensor node can have up to five major components as shown in Figure 4.4.

.

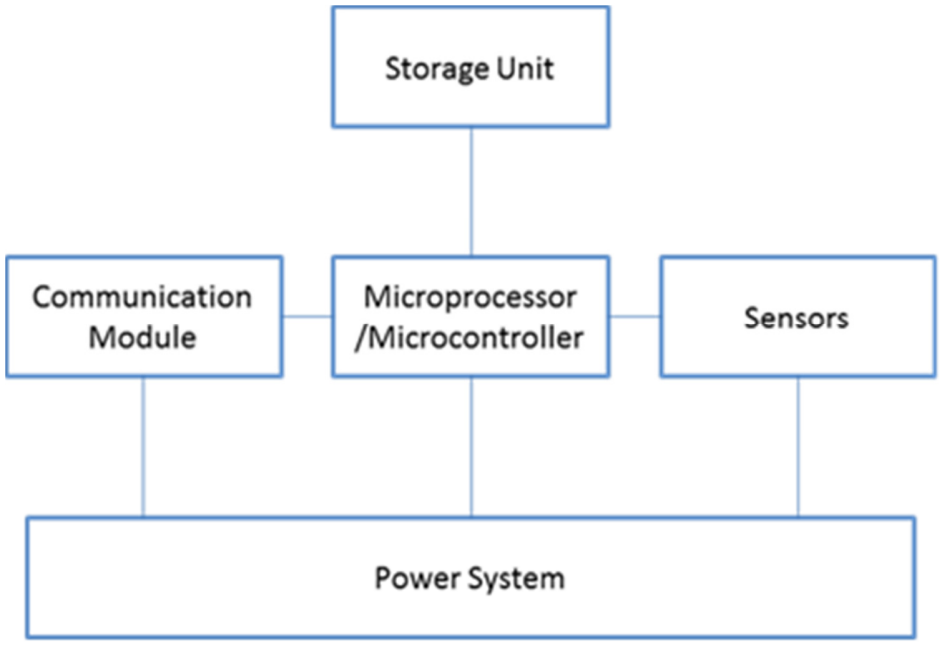

Figure 4.4 Major components of sensor node

Microprocessors or microcontrollers control all the processes and the behavior of the device, and can execute any code. The storage unit stores the gathered data and the relayed data. Normally programs and data use different memory allocations. Sensors are the units used to gather information from the environment or data on specific object. The communication modules are used to convey the data out to the external network and end users. The power system is usually a battery, with or without energy harvest devices.

4.3.1.3.WSN Protocol Stack

The protocol stack of WSN utilizes a simplified open system interface (OSI) model, it usually consists of a Physical Layer, Data Link Layer, Network Layer, Transport Layer, and Application Layer as shown in Figure 4.5. Besides, the stack should also include a power management platform, mobility management platform, and task management platform. These platforms enable the sensor node to work efficiently and utilize the least energy, thus prolonging the system battery life.

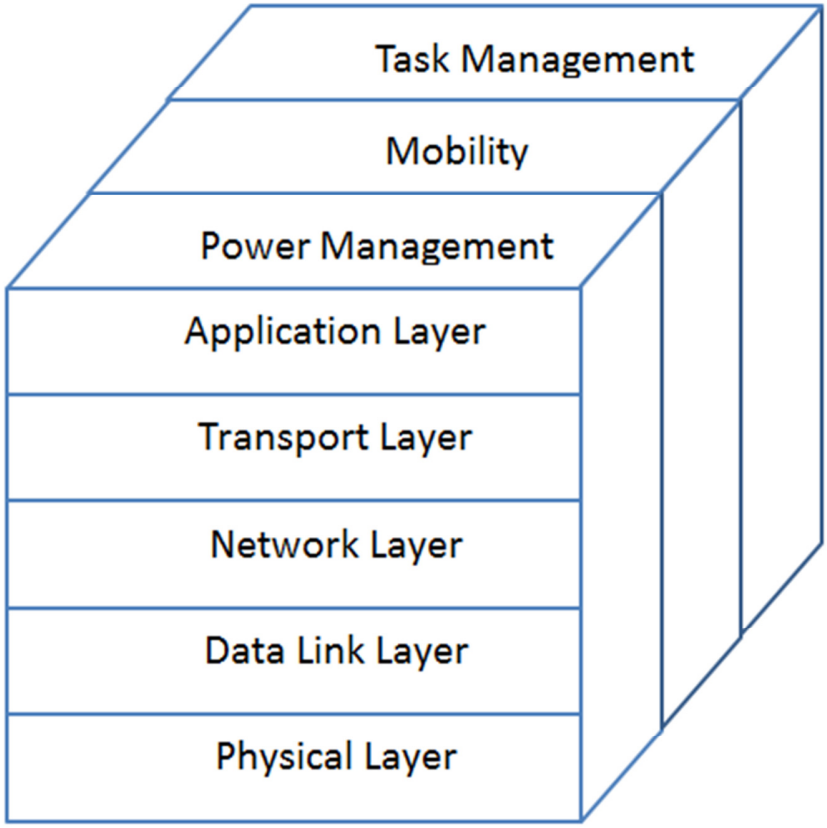

Figure 4.5 WSN protocol stack

Physical Layer

The Physical Layer consists of the basic hardware transmission technologies of a network such as signal modulation/demodulation, transmission and reception. The main

functions of the Physical Layer include frequency selection, signal modulation, and data encryption. For long range telecommunication, it is a critical component in term of implementation complexity and energy consumption.

Data Link Layer

The Data Link Layer is focused on solving multiple access problems. It provides the functions and procedures to transfer data between network entities without contention and might provide the means to detect and correct errors that may occur in the Physical Layer.

Network Layer

The Network Layer takes care of the data routing from the Transportation Layer. With many sensor nodes scattered around the observation area, a routing protocol is necessary to be used for the communication between sensor nodes and sink node.

Transportation Layer

To ensure QoS of the WSN, the Transportation Layer is utilized to maintain data stream throughout the WSN. Refer to the protocol diagram in Figure 4.5. When the WSN needs to be connected to another type of network, the Transportation Layer allows the sink node to communicate with the Task Management node with conventional TCP or UDP protocols. However, since the sensor nodes have very limited power and memory resources, the WSN itself needs a resource efficient protocol.

Application Layer

Based on the task requirement of the WSN, different applications can be added to the Application Layer. It can include a series of application softwares for monitoring purposes.

Because of their limited computing power, memory storage and communication capability, each individual sensor node can only acquire a very limited topology of the

network, so the protocol cannot be over complicated. Meanwhile, WSN topology may be constantly changing, i.e. wireless mobile sensor network, with a requirement of dynamic networking resource reallocation, thus places an even higher requirement of the WSN protocol. The WSN protocol must also ensure that each individual node forms a multi-hop data transportation network, and the current key research areas are Network Layer and Data Link Layer protocols.

4.3.2.Characteristics of Wireless Sensor Network

Large Scale

To acquire precise real-time information, it is necessary to deploy a large number of sensor nodes to the area of interest, the number of nodes can be thousands or more. For example, with the nodes loaded on and deployed by aircraft, WSN can be installed over thousands of acres of land for geological survey or oceanic environmental survey.

Energy Limitation

Every node in the network has access to limited energy. WSN typically works in rural areas with sparse populations or even in hazardous environments. Sometimes it is impossible to change their battery, thus they requires ultra-low power consumption to prolong the operation life of the network.

Self-organization

Self-organization includes functions of auto network association, node and terminal identification, and hack prevention. Compared to a fixed point wireless network, the configuration of WSN is more similar to ad hoc networks, with the prerequisite of a suitable communication protocol for unmanned operation.

Self-management

In WSN, data processing is done within the nodes in preference to reducing data rate on the wireless medium, so that only the data related to other nodes are sent over the RF link. The data centric character is another feature of WSN. Since the positions and deployment of the nodes are not pre-planned, it is possible that some nodes will go out of service due to errors or accidents during deployment. To ensure undisturbed services, redundant nodes must be included in a WSN design. Moreover, data sharing and cooperation between nodes must be implemented to guarantee complete monitoring of the subject.

Differences from ad hoc networks

WSN is similar to an ad hoc network in the feature of distributed network. However, there are many differences between them. Generally speaking, WSN nodes have more limited access to resources compared to handheld devices, but the computing requirement is only optional. When a computational task is needed, if the cost of communication is lower, it could be possible to transfer the computing task to the sink node to improve overall performance.

4.3.3.Wireless Sensor Network Applications

WSN nodes have the capability of continuously gathering data, detecting events, and marking events, monitoring position, and controlling other nodes. These features plus the wireless communication capability ensure broad applications of WSN. It can be applied in environmental monitoring and prediction, geological survey, health monitoring, smart homes, building monitoring, control of complex machinery, metropolitan traffic control, space exploration, garage management, industrial park safety, etc. A very important feature of WSN nodes is that they can be air-dropped to any designated area for different

missions including humanitarian missions. As the research and application of WSN deepens, it will have great impact on every aspect of human lives.

4.3.4.Current Research on Wireless Sensor Network

The earliest WSN research effort was funded by NSF and DARPA, and was carried out by the University of California and Cornell University. Starting in the year 2000, much industrial research on WSN has been reported, including work from Intel [61] and Microsoft [62].

Nowadays, WSN research has gone through two stages of developments. The first stage is focused on the utilization of a micro-electro-mechanism system (MEMS) technology and miniaturization of the nodes. Example works include Wireless integrated network sensors [63] (WINS), and Smart Dust [64]. The second stage of the research is mostly about the network itself and has become a popular study area currently. From the network architecture point of view, every layer has to be studied separately to optimize the overall performance of the WSN. Current research is mainly focused on Network Layer and Link Layer with special interest in establishing robust p2p or meshed network through different MAC protocols.

4.4.Wireless Sensor Network Design

In general, WSN is a large scale, multiple-node network with all the nodes independent and maintenance-free. There are at least two types of nodes in a WSN, the WSN nodes and the sink nodes. For testing purposes, an off-the-shelf USB Dongle with C8051F342 MCU and Si4431 radio from Silicon Labs connected to a laptop computer was used as a sink node.

4.4.1.WSN sensor node module

As for the WSN nodes, they should be small, portable, of low power consumption, and have a highly robust wireless link. A compact design is also desirable for control of cost and large scale production. The WSN node must have MCU, RF module, GSM module, power module, and pneumatic control module (power deployment hardware). A design schematic is shown in Figure 4.6.

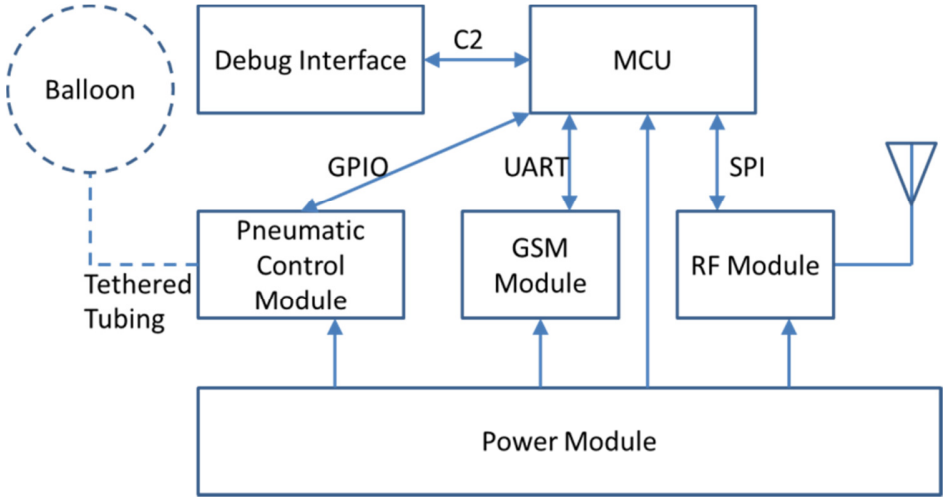

Figure 4.6 WSN node system structure diagram

For the MCU and RF module we used a Silicon Labs C8051F912 MCU and a Si4431 radio [65]. This combo features ultralow power and voltage operation. A single AAA battery can support the module in full active mode (24.5 MHz clock) for over 14 days. The C8051F912 has an on-chip dc-dc converter to allow operation from a single cell battery with a supply voltage as low as 0.9 V. The dc-dc converter is configured to enable bypass mode when VBAT is greater than VDD for use with solar panel. A power harvest interface is utilized for solar panel connection. The Si4431 radio is connected to the MCU through SPI and is controlled by Silicon Labs EZMacPro library, as shown in Figure 4.8. A PCB meander line antenna from Silicon Labs EZRadioPro reference design is used together

with the Si4431 radio. The MCU also has a C2 interface for debugging and firmware updates. The schematic of the MCU configuration is shown in Figure 4.8. The PCB design is sent to Advanced Circuit for fabrication, and the fabricated board is shown in Figure 4.9. Keeping the board to a minimal size, leadless QFN-based ICs and surface mount passive components sized down to 0402 based packages are chosen for the prototype. An advantage to using standard surface mount components is that the board can be assembled on a larger scale using standard manufacture assembly lines for electronics because they are easily handled using automated 'pick and place' machines. Using components this small, hand-soldering is less than ideal for populating the board; therefore, the reflow soldering technique is used to fabricate the PCB assembly. This method requires that a solder paste to be applied to each of the component pads on the circuit board. To place the correct solder paste in the right location, a solder paste stencil made of 3mm thick clear Mylar for relatively low cost at Pololu Robotics and Electronics is designed and applied to the fabrication process. Upon placing the components, the circuit board is place in an oven to flow the solder, which will harden when cooled. The unpopulated circuit board is shown in Figure 4.9. The fully assembled board is shown in Figure 4.10.

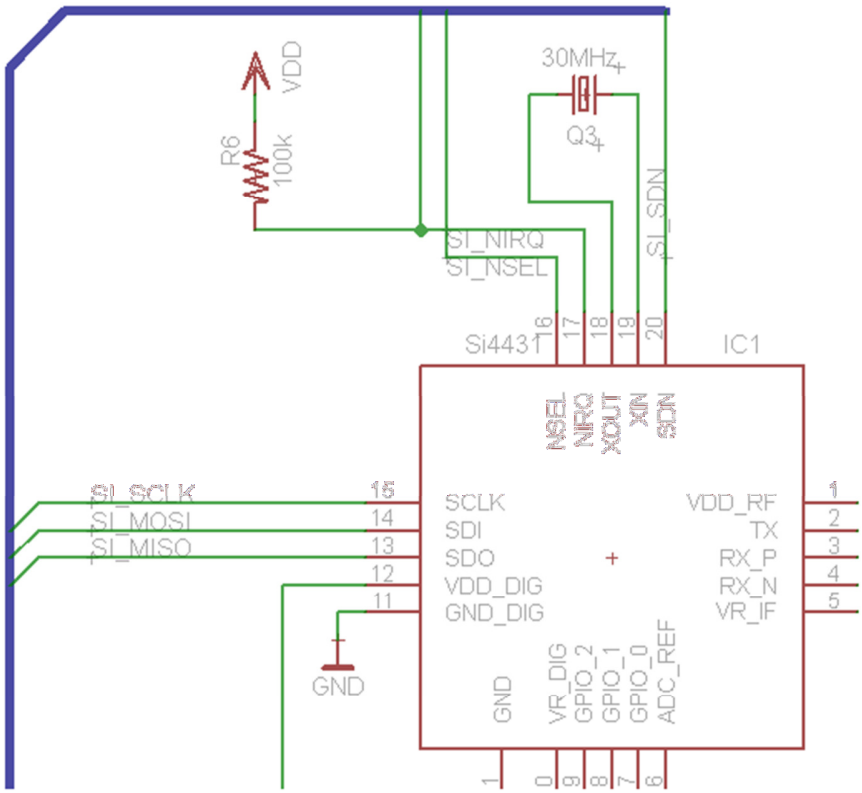

Figure 4.7 Schematics of SPI interface

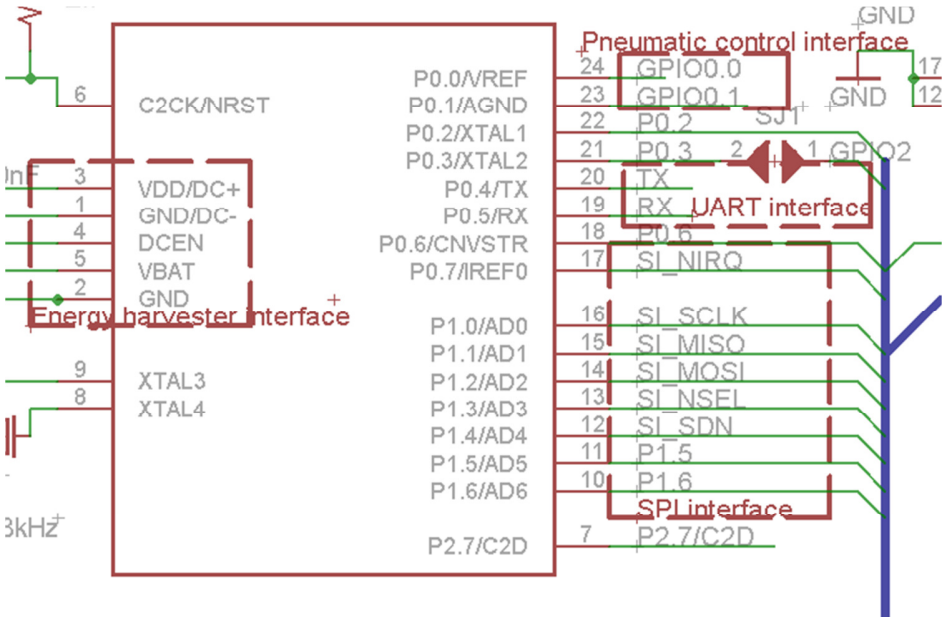

Figure 4.8 MCU pin configuration

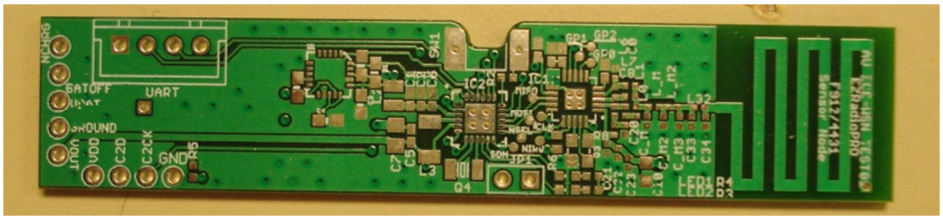

Figure 4.9 Manufactured WSN node PCB board

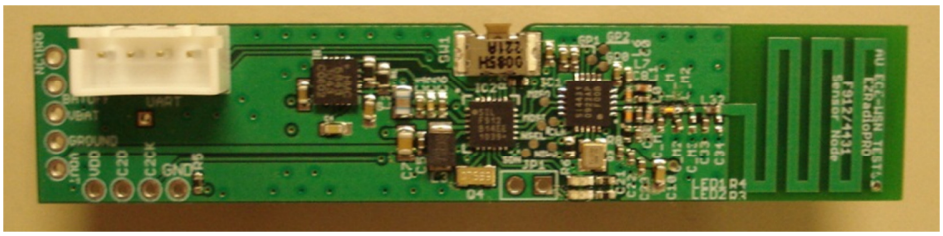

Figure 4.10 Populated WSN node

4.4.2.GSM module

Since IS-95-style CMDA is a tightly controlled intellectual property, adapting CDMA is out of the question. GSM modules have become our main focus since they are proven to be working well and over 80% of the world's carriers are using it [66].

The greatest challenge presented in our project was to accommodate the GSM “Um” air interface into WSN design. Although the GSM industry is one of the largest industries in the world, there are only few implementations and most of them are close source. We have investigated OpenBTS®, which is a promising open source project. However, operation of OpenBTS stack requires a computer with Linux OS and Universal Software Radio Peripheral hardware. Accommodating entire GSM stack into WSN nodes with limited computing capability and battery operation requirement can be an extremely challenging task even for expert wireless companies, if at all possible. Our solution to this problem was to develop a low power mixed-signal GSM transceiver IC supporting SDCCH and SACCH channels.

Although SMS is defined in five layers of “Um”, only L1 and L2 layers are necessary to provide SMS to mobile users in our setup. The function of L3 and above can be passed on to the WSN network layer to relay text messages and using WSN as the SMS backhaul. The proposed GSM chip should contain the following components: Analog TX: PA, VCO, filters, oscillators; Analog RX: LNA, Mixers, PGA, PLLs, ADC; Digital: GMSK or 8PSK modem, and interface control. The GSM IC can be interfaced with popular low power microprocessors such as the C8051F series or the ARM series with simplified OpenBTS stack to provide registration and SMS services. For this experiment, only off-the-shelf components are utilized to prove the concept. However, attention and help from the transceiver IC industry is welcome in the future.

Alternatively, to prove we could extract text messages from a “Um” air interface, we modified a commercial GSM module with only SMS multicasting capability and interfaced it to the WSN node module. The cellular module we used was a GSM SM5100B from SpreadTrum and is powered by an external LiPo battery. It is a quad-band GSM module with SMS, GSM/GPRS, two UARTs, and an SPI interface. The SM5100B is connected to the WSN node’s MCU using two wires UART at 9600bps baud rate, (8-N-1), and no flow control. The breadboard prototype test is shown in Figure 4.11.

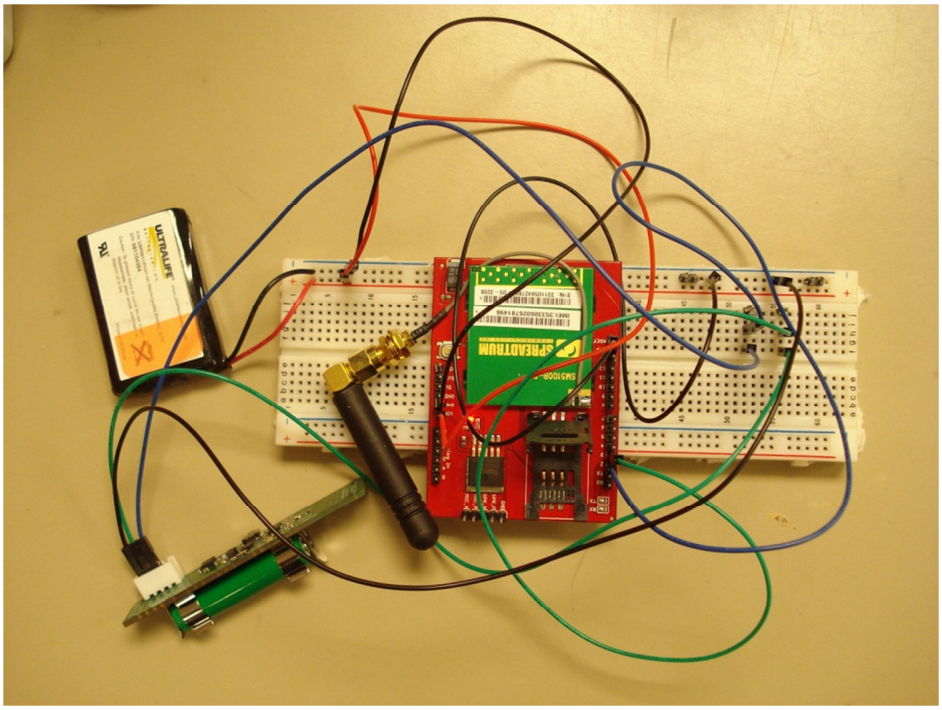

Figure 4.11 GSM module attached to WSN node through breadboard

4.4.3.Power harvest module

For the wireless node to be able to operate in varying environmental conditions, we chose to implement two sources of power: photovoltaic cells and a secondary battery. Using this combination, it is possible to sustain system operations for an extended time period. The secondary batteries provide power to the system in times of darkness, as well as any periodic high current demand need by the RF transceiver. The solar cells power operations during times of sunlight, as well as replenish the charge of the secondary batteries from the excess power generated. The solar panel tested is shown in Figure 4.12. Looking at the simplified diagram below in Figure 4.13 we see that in times of sunlight, the solar cell will develop a voltage potential across the cells and this voltage is greater than the voltage of the batteries, the Schottky diode will start conducting and will allow current to flow from the solar cell and into the battery and/or the voltage regulator. Excess power not

needed by the voltage regulator is then diverted into the battery. Over time, the battery will reach a voltage level that is associated with being fully charged. To prevent from over-charging, which may cause irreversible damage, a Zener diode has been placed in parallel with the battery. By selecting the correct reverse breakdown voltage of this Zener diode, any excess power generated by the solar cells that is not needed by the battery or the system will be dissipated.

Since the voltage of the battery or the solar cells is not controlled, a voltage regulator must be used in order to adjust and control the voltage supplied to the rest of the system. To achieve this regulation as efficiently as possible, the DC/DC convertor onboard the C8051F912 MCU is utilized for this purpose. Using this convertor, the system can be correctly powered from the batteries and solar cell when their voltages weaken to 0.9 volts. When the voltage supplied by the solar cell/battery combination reaches the design regulator output voltage, the regulator will bypass itself to operate at the utmost efficiency. Since the DC/DC convertor is flexible within the input voltage range, this allows for different combinations of batteries and solar cells for the system if other power source options are desired.

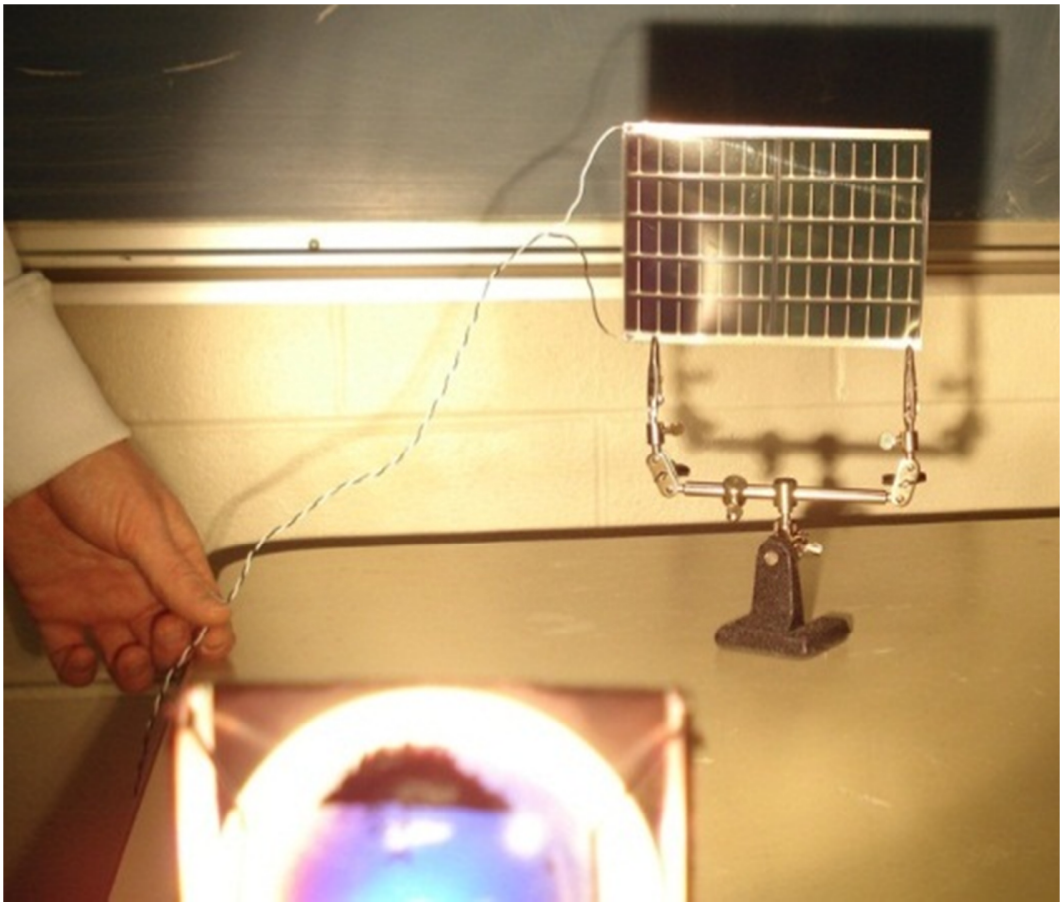

Figure 4.12 Solar panel under test

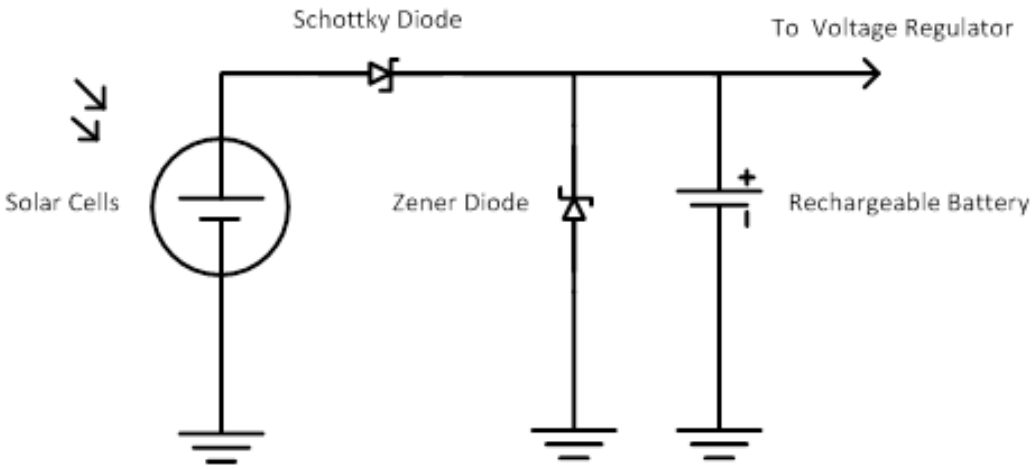

Figure 4.13 Improvement schematic of the energy harvest interface

4.4.4.Pneumatic control module

Since the WSN node will be dropped into high population areas, safe descent must be emphasized in the design. Normally parachutes or balloons are the only two options. We have chosen an inflatable weather balloon approach because it has a twofold benefit: it provides elevation to the sensor module to increase communication range and serves to slow the descent. The balloon is inflated via a helium cartridge, with a pressure regulator, and a low power solenoid valve. A fixed pressure regulator was selected because it weighs less than a conventional regulator with a gauge. The solenoid valve is controlled by the MCU through GPIO port P0.0. The pneumatic module is shown in Figure 4.14. The pneumatic off-the-shelf hardware was selected as being most well suited to fulfill our design requirements. The individual components are justified as follows: the smallest OTS helium cartridge is chosen. The helium is stored in a burst resistant, high pressure container and thus requires a pressure regulator or reducer. A fixed pressure regulator with safety relief features is chosen because it is lighter than an adjustable regulator. A micro-solenoid valve controllable by the MCU to inflate the balloon is also included.

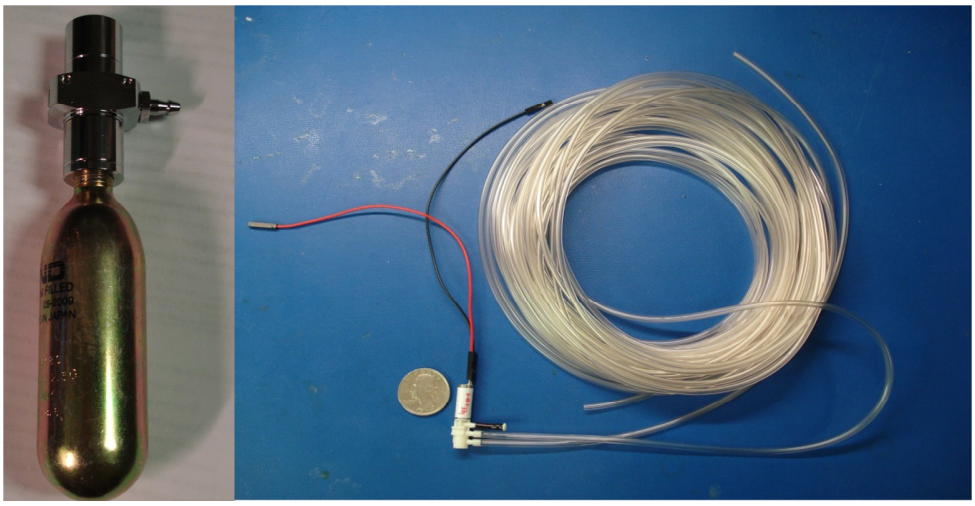

Figure 4.14 Components of pneumatic system

4.4.5.Multi-functional Tether

An important piece of hardware was not available commercially to connect the balloon and WSN node with the base module. Instead we developed a novel multi-functional tether using a textile technology called braiding to incorporate pneumatic tubing, electrical conductors, a protective layer and strength members in a single manufacturing process, see Figure 4.15. 16 Nylon yarns were braided over the tubing and electrical conductors using a Wardwell Maypole style braiding machine to consolidate these components, see Figure 4.16. The Nylon yarns serve as primary strength members, as well as provide environmental protection against abrasion and ultraviolet degradation.

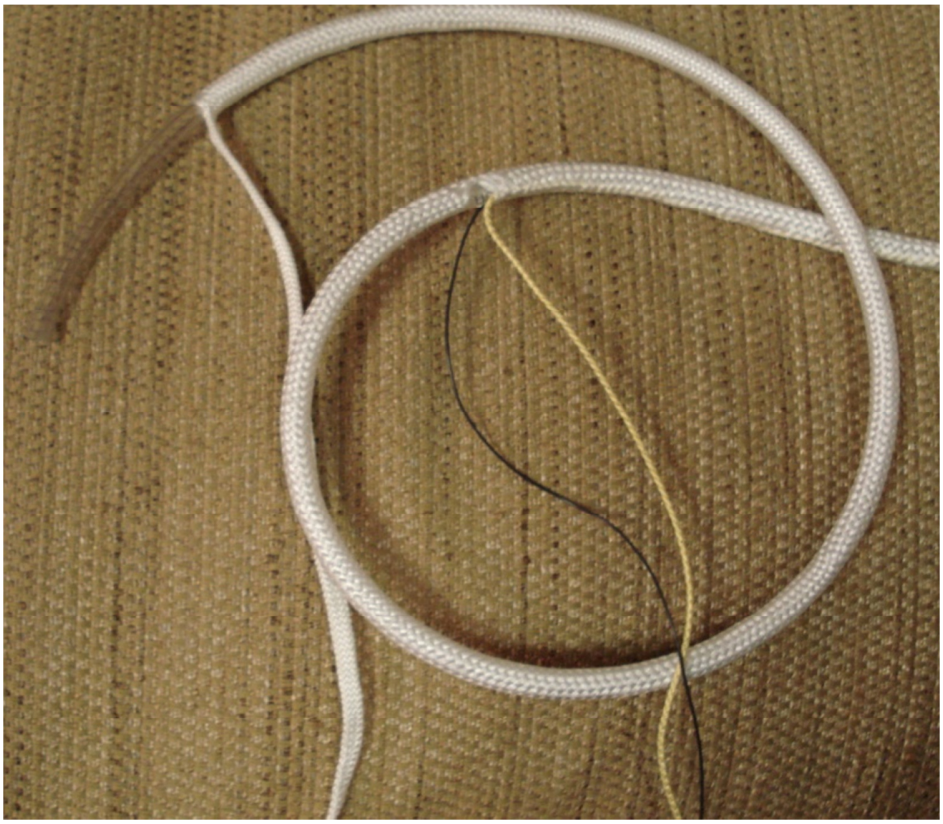

Figure 4.15 Multi-functional braided tether with pneumatic tubing and wires

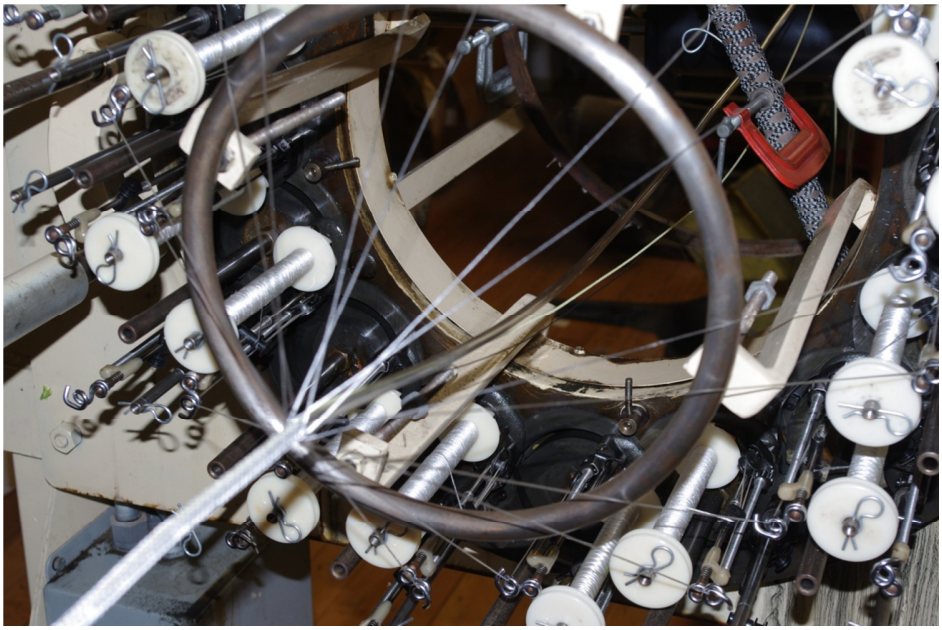

Figure 4.16 Braiding machine during manufacture of multi-functional tether

4.4.6.Weather Proof Protect Shell and Base Module

The bottom portion of the protective shell and base module contains the pneumatic control module and protects against impact by shock absorbing polyurethane foam, see Figure 4.17. The protective shell is also designed to act as an anchor to the ground by arranging the heavy components appropriately. Although weight is important, it is intended to optimize the physical arrangement of components throughout the design, so that each component serves multiple design needs. A two liter soda bottle is utilized to serve as a protective shell and housing for the primary components during deployment and end use, see Figure 4.18. The advantages of using a recycled bottle as a protective shell are manifold: First, it is an off-the- shelf component that can be easily provided from many sources. Second, as a component benefitting from mass production, it is inexpensive. Third, it is lightweight, strong, and can provide sufficient protection against moisture and environmental hazard. We have modified the bottle to produce top and bottom sections.

Each of the aforementioned modules is inserted and the top and bottom section re-combined, see Figure 4.18.

Figure 4.17 Impact resisting polyurethane foam

Figure 4.18 Weatherproof shell constructed from recycled soda bottle

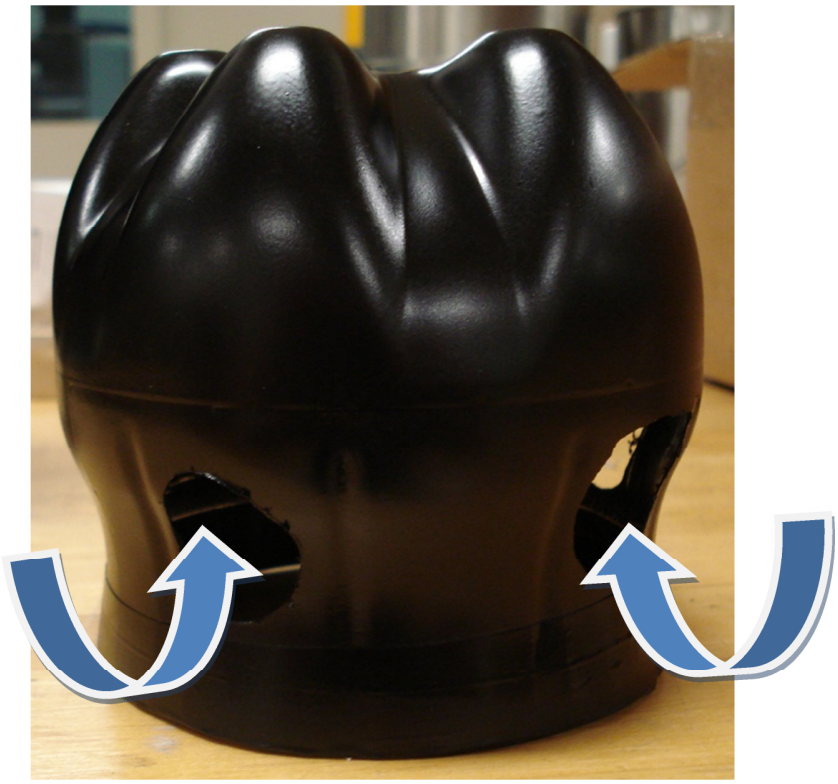

Figure 4.19 Air holes drilled in bottle to cause separation during deployment

The top and bottom are designed to separate automatically during airborne deployment. Holes have been placed along the sides of the bottom section in such a way

that air pressure is exerted during descent causing a separation, see Figure 4.19. The design is such that as the bottle begins to descend, the top and bottom separate, the balloon begins to inflate, and the multi-functional tether unspools. Although a high altitude deployment test is not scheduled at this time, each system component was tested individually with success. For example, an air nozzle test at various air velocities is carried out to test the separation and found minimal air pressure causes the top to separate from the bottom. Figure 4.20 shows the initial separation experiment. The bottle was dropped from a second story and the separation was observed as well. The separated top and bottom compartments are shown in Figure 4.21.

Figure 4.20 Air pressure separation experiment

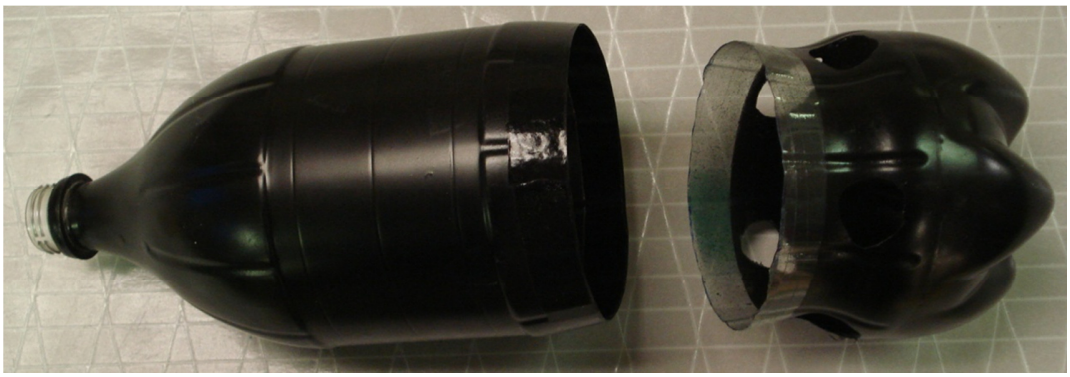

Figure 4.21 Top and bottom separation

4.5.Microcontroller Firmware

The MCU firmware is developed using Silicon Labs Integrated Development Environment. The WSN protocol stack is developed based on Silicon Labs EZMacPro library with MAC layer and partially hardware supported PHY layer.

The communication protocol we used has a star topology with the USB Dongle as master and WSN node as slave. The nodes are self-organized using contention sensing method provided by the EZMacPro library (Listen-before-talk). Multi-hopping mode is also enabled for nodes to relay received text messages. The implemented routing protocol uses a simple flood-and-forwarding algorithm. The advantage of using EZMacPro library allows us focus more on the design rather than "reinventing the wheel"; it also supports multiple addressing modes, contention detection, CRC, and frequency hopping. For each network, it can address up to 255 WSN nodes. EZMacPro implements its own state machine using two interrupt routines. The timer can realize different timed tasks, while External INT supports RF related interrupt requests. The behavior of EZMacPro is determined by the parameter of a series of EZMacPro registers. APP layer can easily access and control low level behavior using C functions.

4.6. Graphic User Interface

Our GUI is written in Visual C# based on the Silicon Labs P2P UART communication demo with SLABHIDDevice.dll USB dynamic library. We added in an addressing mode so that it will be compatible with the star topology. The GUI provides ASCII and HEX input/output through the wireless link to the WSN nodes.

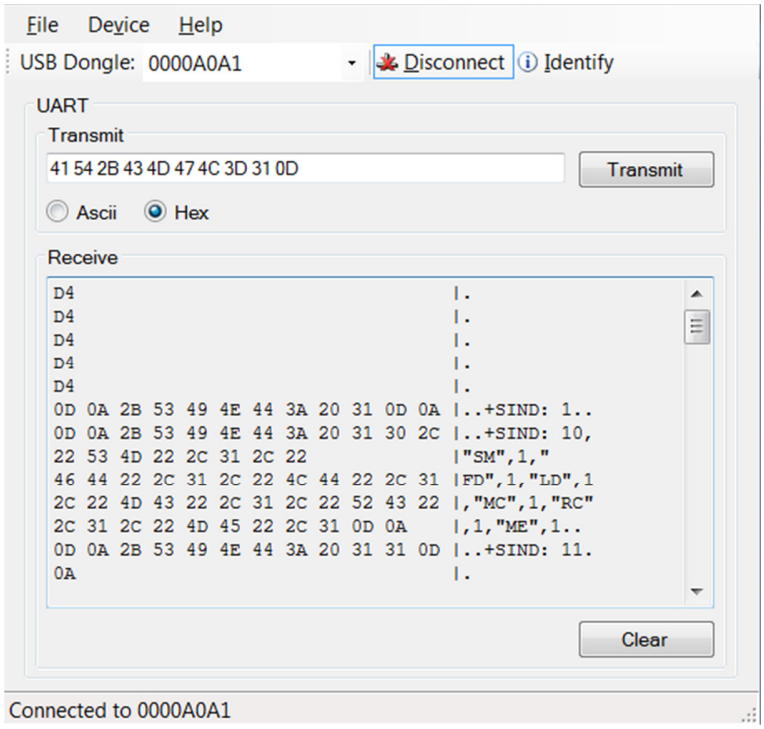

Figure 4.22 Start up data through GSM-UART-RF-USB link

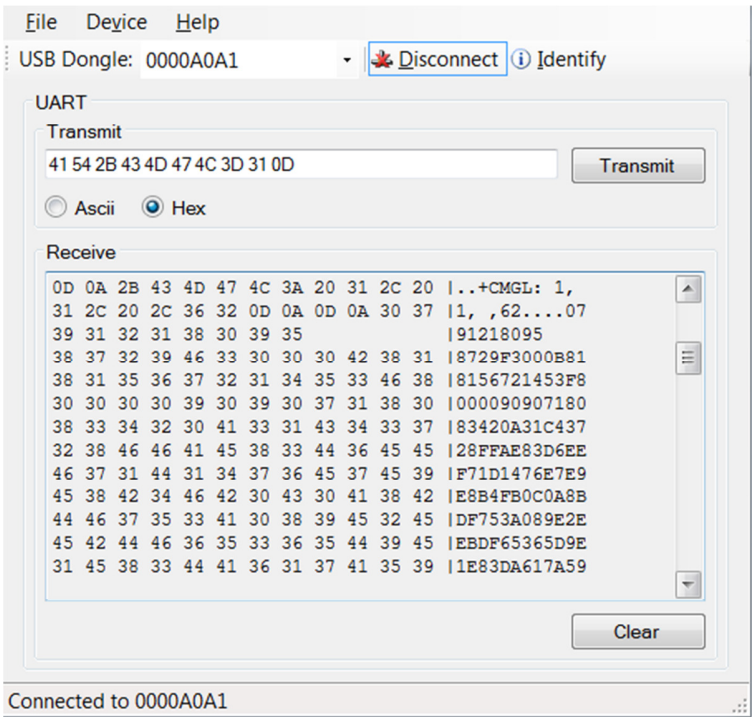

Figure 4.23 SMS Received in PDU format through GSM-UART-RF-USB link

4.7.Results

Communication with the GSM module using AT commands and retrieval of SMS from GSM module are successfully carried out through the WSN RF link. An AT "command request for receive" SMS is sent from the master to the WSN node through the RF link, and then transmitted to the GSM module via UART. The gathered SMS in PDU form is then transferred to the WSN node through UART and then transmitted over the RF link to the sink node. Figure 4.22 shows the received start up data indicating the GSM module is successfully registered to the cellular network. Figure 4.23 shows the received text message in PDU format and Table 4-1 shows the decoded text message. The result proves that a WSN RF link can be used to receive, transmit, and relay GSM text messages.

Table 4-1 Received SMS in PDU format and decoded text.

PDU format	Decoded text
07912180958729F3000B818156721453F8000090907 18083420A31C43728FFAE83D6EEF71D1476E7E9E8B4 FB0C0A8BDF753A089E2EEBDF65365D9E1E83DA617 A599E0EB3E73F	SMSC#+12085978923 Sender:18652741358 TimeStamp:17/09/09 08:38:24 TP_PID:00 TP_DCS:00 TP_DCS-popis:Uncompressed Text class:0 Alphabet:Default Do you know anything about piezoeltric materials? Length:49

4.8.Summary

Utilizing off-the-shelf components is very important in a research and development environment. However, these products are not always ideal for their intended application. Weight is critical in this design. Although helium balloon payloads are sufficient for the prototype design, no intuition about helium balloon payload before this project was taken into account seriously. A further design iteration and testing where minimal weight is the

primary objective will be carried out and save even more weight. It is also learned that the manufacturer's specification can be misleading in design work of this type.

A novel rapidly deployable communication network concept has been proposed and prototype developed. The design is a result of a multi-disciplinary efforts including mechanical, electrical, computer, and textile engineering. The concept is developed with laboratory testing and proven in the field. The software and hardware are developed with both laboratory equipment and field testing. The concept of transmitting text message data between Um radio interface and WSN radio interface is proven. A novel multi-functional tether is also developed to facilitate communication, allow pneumatic control of the balloon, and provide the necessary tensile strength and environmental protection. Although we have proven the concept by developing a deployable scheme for emergency communication during disaster relief, we have also learned many lessons, and realize future work is needed including increasing communication range and developing application specific components optimized for this endeavor. We sincerely hope this technology can be developed further and implemented to save lives, improve emergency management and response, and that our effort may truly benefit humanity in the future.

Chapter 5.Conclusion and Future Work

5.1.Conclusion on Electromagnetic Textile Research

This dissertation explored the radiation mechanism of woven antennas by conducting simulations and antenna testing. The results suggest that the structure of the woven antenna disturbed the fundamental resonant mode of the MSA, while the second lowest resonant mode remained. The designed woven antennas also possess an efficient resonant mode much lower than all MSA model predictions. Thus, it is a novel type of compact, low profile, and highly efficient antenna.

Meanwhile, such phenomena also lead to the numerical research of textile FSS and AMC/AEC structures. This research is among the first to discover the unique electromagnetic properties of both materials. Based on these findings, this new type of material is defined as the *Electromagnetic Textile* distinguishing from the common E-textile, which merely provides DC connectivity of computing, digital components, and electronics to be embedded in fabrics.

The development of a novel electromagnetic material is accomplished. The unique material is applicable to a variety of electromagnetic problems, including novel low-profile antennas, frequency selective surfaces, and artificially electromagnetic surfaces. The

author hopes this research will draw interest from both textile and electromagnetism researchers and start a new era of electromagnetic textile material research.

5.2.Conclusions on Emergency Communication Network Development

Efforts on development of novel ECN resulted in desirable outcome. The hypothesis that WSN RF link can be used to relay GSM text messages was proven. The protective shell and tether have shown adequate strength during field testing. The feasibility of using air-drop SMS-WSN to form emergency communication network was successful. However, due to the complexity of the ECN system, significant work remains from both a theoretical and an experimental perspective. We are very interested in furthering this entire project to develop what is necessary so that it might be implemented. Presently we are considering new design iteration, incorporating the lessons learned to improve the design. Future research will be strongly advanced by partnering with industry to leverage their knowledge, resources, and experience to extend the present capabilities to include mixed-signal IC design among other possibilities.

References

[1]S. Cherry, "The wireless last mile," Spectrum, IEEE, vol. 40, pp. 18-22, 2003.

[2]C. A. Balanis, Antenna Theory: Analysis and Design: Wiley-Interscience, 2005.

[3]J. Kraus and R. Marhefka, Antennas: McGraw-Hill New York, 1988.

[4]K. Wong and J. Wiley, Compact and broadband microstrip antennas: Wiley Online Library, 2002.

[5]W. Stutzman, Thiele, Antenna Theory and Design: New York: Wiley, 1981.

[6]R. Garg, Microstrip antenna design handbook: Artech House, 2001.

[7]Y. Lo, et al., "Theory and experiment on microstrip antennas," Ieee Transactions on Antennas and Propagation, vol. 27, pp. 137-145, 1979.

[8]K. Carver and J. Mink, "Microstrip antenna technology," Ieee Transactions on Antennas and Propagation, vol. 29, pp. 2-24, 1981.

[9]W. Richards, et al., "An improved theory for microstrip antennas and applications," Ieee Transactions on Antennas and Propagation, vol. 29, pp. 38-46, 1981.

[10]A. Simmons and A. Kay, "The Scalar Feed--A High Performance Feed for Large Paraboloid Reflectors," presented at the Design and Construction of Large Steerable Aerials, 1966.

[11]V. Rumsey, "Horn antennas with uniform power patterns around their axes," Antennas and Propagation, IEEE Transactions on, vol. 14, pp. 656-658, 2002.

[12]H. Minnett and B. Thomas, "A method of synthesizing radiation patterns with axial symmetry," Ieee Transactions on Antennas and Propagation, vol. 14, pp. 654-656, 1966.

[13]S. Lee and W. Jones, "Surface waves on two-dimensional corrugated surfaces," Radio Sci, vol. 6, pp. 811–818, 1971.

[14]P. S. Kildal, "Definition of artificially soft and hard surfaces for electromagnetic waves," Electronics Letters, vol. 24, pp. 168-170, 1988.

[15]P. S. Kildal, "Artificially soft and hard surfaces in electromagnetics," Antennas and Propagation, IEEE Transactions on, vol. 38, pp. 1537-1544, 1990.

[16]P. S. Kildal, "The hat feed: A dual-mode rear-radiating waveguide antenna having low cross polarization," Antennas and Propagation, IEEE Transactions on, vol. 35, pp. 1010-1016, 2002.

[17]E. Yablonovitch, "Inhibited spontaneous emission in solid-state physics and electronics," Physical review letters, vol. 58, pp. 2059-2062, 1987.

[18]S. John, "Strong localization of photons in certain disordered dielectric superlattices," Physical review letters, vol. 58, pp. 2486-2489, 1987.

[19]J. D. Joannopoulos and J. N. Winn, Photonic crystals: molding the flow of light: Princeton Univ Pr, 2008.

[20]Y. Rahmat-Samii and H. Mosallaei, "Electromagnetic band-gap structures: classification, characterization, and applications," 2002, pp. 560-564.

[21]D. Sievenpiper, et al., "High-impedance electromagnetic surfaces with a forbidden frequency band," Microwave Theory and Techniques, IEEE Transactions on, vol. 47, pp. 2059-2074, 1999.

[22]R. Mittra, et al., "Techniques for analyzing frequency selective surfaces-a review," Proceedings of the IEEE, vol. 76, pp. 1593-1615, 2002.

[23]B. A. Munk, Frequency selective surfaces: Theory and design: Wiley-Interscience, 2000.

[24]C. Tsao and R. Mittra, "Spectral-domain analysis of frequency selective surfaces comprised of periodic arrays of cross dipoles and Jerusalem crosses," Antennas and Propagation, IEEE Transactions on, vol. 32, pp. 478-486, 2002.

[25]C. Tsao and R. Mittra, "A spectral-iteration approach for analyzing scattering from frequency selective surfaces," Antennas and Propagation, IEEE Transactions on, vol. 30, pp. 303-308, 2002.

[26]P. S. Nakar, "Design of a compact Microstrip Patch Antenna for use in Wireless/Cellular Devices," 2004.

[27]E. Madenci and I. Guven, The finite element method and applications in engineering using ANSYS: Springer-Verlag New York Inc, 2006.

[28]I. Locher, et al., "Design and characterization of purely textile patch antennas," Ieee Transactions on Advanced Packaging, vol. 29, pp. 777-788, Nov 2006.

[29]Y. Kim, et al., "Wearable UHF RFID tag antenna design using flexible electro-thread and textile," Antennas and Propagation International Symposium, 2007 IEEE, pp. 5487-5490, 2007.

[30]R. K. Shaw, et al., "The characterization of conductive textile materials intended for radio frequency applications," Ieee Antennas and Propagation Magazine, vol. 49, pp. 28-40, Jun 2007.

[31]C. Hertleer, et al., "The use of textile materials to design wearable microstrip patch antennas," Textile Research Journal, vol. 78, pp. 651-658, Aug 2008.

[32]Y. Ouyang and W. J. Chappell, "High Frequency Properties of Electro-Textiles for Wearable Antenna Applications," Antennas and Propagation, IEEE Transactions on, vol. 56, pp. 381-389, 2008.

[33]S. Bashir, et al., "A flexible fabric metasurface for on body communication applications," 2009, pp. 725-728.

[34]G. A. Conway and W. G. Scanlon, "Antennas for Over-Body-Surface Communication at 2.45 GHz," Ieee Transactions on Antennas and Propagation, vol. 57, pp. 844-855, Apr 2009.

[35]S. Zhu and R. Langley, "Dual-band wearable textile antenna on an EBG substrate," Antennas and Propagation, IEEE Transactions on, vol. 57, pp. 926-935, 2009.

[36]P. S. Kildal, et al., "Special issue on artificial magnetic conductors, soft/hard surfaces, and other complex surfaces," Antennas and Propagation, IEEE Transactions on, vol. 53, pp. 2-7, 2005.

[37]L. J. Martin, et al., "Effect of Permittivity and Permeability of a Flexible Magnetic Composite Material on the Performance and Miniaturization Capability of Planar Antennas for RFID and Wearable Wireless Applications," Ieee Transactions on Components and Packaging Technologies, vol. 32, pp. 849-858, Dec 2009.

[38]W. Lee, et al., "Characteristics of an electromagnetic wave absorbing composite structure with a conducting polymer electromagnetic bandgap (EBG) in the X-band," Composites Science and Technology, vol. 68, pp. 2485-2489, 2008.

[39]N. Zhao, et al., "Microwave absorbing properties of activated carbon-fiber felt screens (vertical-arranged carbon fibers)/epoxy resin composites," Materials Science and Engineering: B, vol. 127, pp. 207-211, 2006.

[40]S. Lee, et al., "Radar Absorbing Structures with Frequency Selective Fabric Composites," 2006.

[41]S. Lee, et al., "Electromagnetic characteristics of frequency selective fabric composites," Electronics Letters, vol. 42, pp. 439-441, 2006.

[42]S. Lee, et al., "Fabrication and design of multi-layered radar absorbing structures of MWNT-filled glass/epoxy plain-weave composites," Composite structures, vol. 76, pp. 397-405, 2006.

[43]P. Kim, et al., "EM characteristics of the RAS composed of E-glass/epoxy composite and single dipole FSS element," Composite structures, vol. 75, pp. 601-609, 2006.

[44]M. Duhovic and D. Bhattacharyya, "Simulating the deformation mechanisms of knitted fabric composites," Composites Part A: Applied Science and Manufacturing, vol. 37, pp. 1897-1915, 2006.

[45]A. Foroozesh, et al., "Application of artificial ground planes in dual-band orthogonally-polarized low-profile high-gain planar antenna design," Progress In Electromagnetics Research, vol. 84, pp. 407-436, 2008.

[46]T. Kim and C. Seo, "A novel photonic bandgap structure for low-pass filter of wide stopband," Microwave and Guided Wave Letters, IEEE, vol. 10, pp. 13-15, 2002.

[47]H. Mosallaei and Y. Rahmat-Samii, "Periodic bandgap and effective dielectric materials in electromagnetics: characterization and applications in nanocavities and waveguides," Antennas and Propagation, IEEE Transactions on, vol. 51, pp. 549-563, 2003.

[48]Y. H. Ouyang, et al., "Body-Worn Distributed MIMO System," Ieee Transactions on Vehicular Technology, vol. 58, pp. 1752-1765, May 2009.

[49]C. Hertleer, et al., "Aperture-Coupled Patch Antenna for Integration Into Wearable Textile Systems," Antennas and Wireless Propagation Letters, vol. 6, 2007.

[50]M. Tanaka and J. H. Jang, "Wearable microstrip antenna for satellite communications," Ieice Transactions on Communications, vol. E87B, pp. 2066-2071, Aug 2004.

[51]P. Salonen, et al., "WEBGA-wearable electromagnetic band-gap antenna," Antennas and Propagation Society Symposium, 2004. IEEE, vol. 1, 2004.

[52]P. Salonen, et al., "Dual-band wearable textile antenna," Antennas and Propagation Society Symposium, 2004. IEEE, vol. 1, 2004.

[53]M. Tanaka and J. Jang, "Wearable microstrip antenna," 2003, pp. 704-707.

[54]P. Salonen and L. Hurme, "A novel fabric WLAN antenna for wearable applications," Antennas and Propagation Society International Symposium, 2003. IEEE, vol. 2, 2003.

[55]"A Failure of Initiative. Final Report of the Select Bipartisan Committee to Investigate the Preparation for and Response to Hurricane Katrina.," United States Government Printing Office2006.

[56]M. Thomas, et al., "EVResponse-moving beyond traditional emergency response notification," 2005.

[57]A. Curtis, et al., Hurricane Katrina: GIS response for a major metropolitan area: Natural Hazards Center, 2006.

[58]A. Gunes and J. Kovel, "Using GIS in emergency management operations," Journal of Urban Planning and Development, vol. 126, p. 136, 2000.

[59]T. Schoenharl, et al., "WIPER: Leveraging the cell phone network for emergency response," International Journal of Intelligent Control and Systems, vol. 11, pp. 209–216, 2006.

[60]J. Deaton, et al., "Analyzing Options for Airborne Emergency Wireless Communications," Idaho National Laboratory2008.

[61]A. Mainwaring, et al., "Wireless sensor networks for habitat monitoring," 2002, pp. 88-97.

[62]C. S. Raghavendra, et al., Wireless sensor networks: Springer, 2004.

[63]G. J. Pottie and W. J. Kaiser, "Wireless integrated network sensors," Commun. ACM, vol. 43, pp. 51-58, 2000.

[64]J. M. Kahn, et al., "Next century challenges: mobile networking for "Smart Dust"," presented at the Proceedings of the 5th annual ACM/IEEE international conference on Mobile computing and networking, Seattle, Washington, United States, 1999.

[65]SiliconLaboratories. (2010, C8051F91x-90x Data Sheet. Available: http://www.silabs.com/SupportDocuments/TechnicalDocs/C8051F91x-90x.pdf

[66]OpenBTS. OpenBTSBackground. Available: http://gnuradio.org/redmine/wiki/gnuradio/OpenBTSBackground

APPENDIX A. FSS Simulation Using Periodic Boundary Conditions in Ansoft HFSS

An overview of the full-wave analysis of frequency selective surfaces using Periodic Boundary Conditions (PBCs) in Ansoft HFSS is presented in this appendix. This tutorial is based on the resources provided by Ansys Corporation.

The characteristics of Frequency selective surfaces (FSSs) are their incident wave reflection and transmission properties. FSSs in general are 2-D planar, periodic arrays with an infinite extent. According to the Floquet's theorem, the scattering properties from the entire infinite array can be derived from the field information of a single period of the array (unit cell). This condition assumes a plane-wave excitation.

Ansys HFSS utilizes the Floquet theorem to simulate antenna array and FSSs. This can be done through the modeling one unit cell and applying the periodic boundary conditions (PBC) to the unit cell. The excitation is usually set up as a plane-wave port on one side of the unit cell. The procedure we used to simulate an FSS in HFSS 12 is provided here through an example, including all the steps for modeling. Example considered here is the surface presented in Chapter 3, the square aperture FSS.

Simulation Model Setup

The example considered here is a single sided array of metallic aperture on top of a substrate. After drawing the unit cell, the PBC is assigned as the boundary condition to each pair of the opposite side walls of the unit cell to set up the infinitely array 2-D space.

Perfectly-matched layers (PMLs) are set up over the top and bottom sides of the box outgoing wave absorption. Finally, the excitation is chosen to be the incident plane-wave. These steps are summarized in the following.

1) Model the unit cell, including the substrate and the metallic aperture on top of the substrate.

2) Draw an air box which includes the unit cell. The box sides must touch the substrate edges.

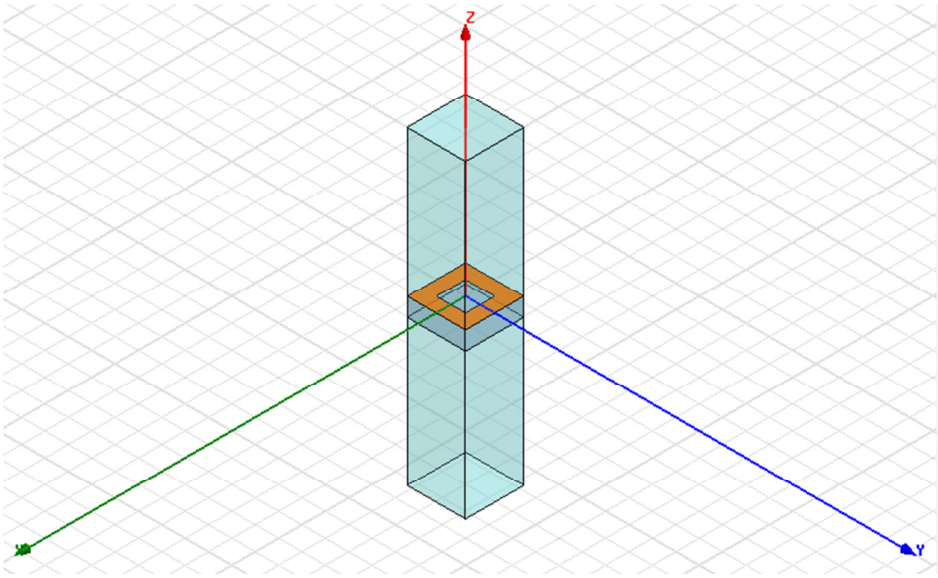

Figure A.1 The unit cell geometry inside the simulation air box

3) Assign the Master and Slave boundaries to the air box. Select the face shown in Figure A.2, and click *HFSS>Boundaries>Assign>Master* or right click on Boundaries in the Project tree and select *Assign>Master.* Click the drop down menu for the U vector, and click, *New Vector*. The *Measure dialog* and the *Create Line* prompt appear. Draw the U vector of the coordinate system on the selected face. Click on the lower left corner as the starting point, and drag the cursor to the right corner and click. In the **Master Boundary dialog**, for the *V Vector*, check the box for *Reverse direction*, and OK to close the dialog.

Select the opposite face, and *HFSS>Boundaries>Assign Slave* or right click on Boundaries in the Project tree and select *Assign>Slave.* The Slave dialog appears with the General Tab selected. Select Master1 as the Master boundary. Draw the U Vector as shown. Accept the other settings and OK to close the dialog. Repeat the procedure for the Master2 and Slave 2 boundaries.

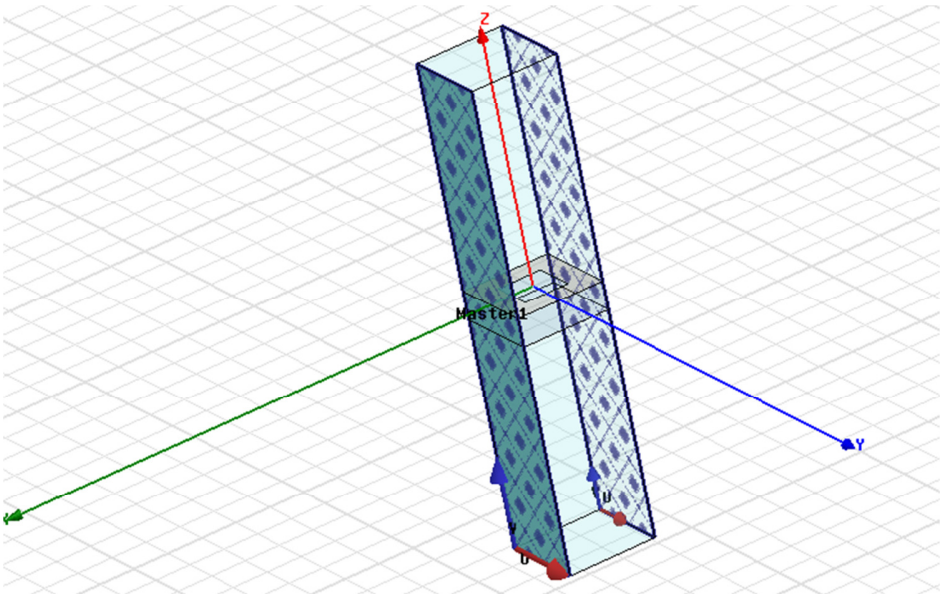

Figure A.2 Assign master and slave boundary

Assign the Floquet Ports

This section shows how to assign the Floquet ports to the top and bottom faces of the model.

Select the top face of the model, and click *HFSS>Excitations>Assign>Floquet Port*. The Floquet Port wizard appears, showing the General page. For the Lattice Coordinate System, from the drop down menu for $\boldsymbol{a}$ direction, select New Vector. The Measure Data dialog appears, and the Create Line dialog tells you to draw the $\boldsymbol{a}$ lattice vector on the plane of the face as shown in Figure A.3, clicking on the corner nearest the Z axis to start, and then clicking on the corner along the X direction. When you make the second click to

complete the vector, the **Measure Data** and **Create line** dialogs disappear, and the **Floquet Port** wizard reappears, showing that the $\boldsymbol{a}$ vector is Defined. Repeat the process to draw the $\boldsymbol{b}$ vector as shown.

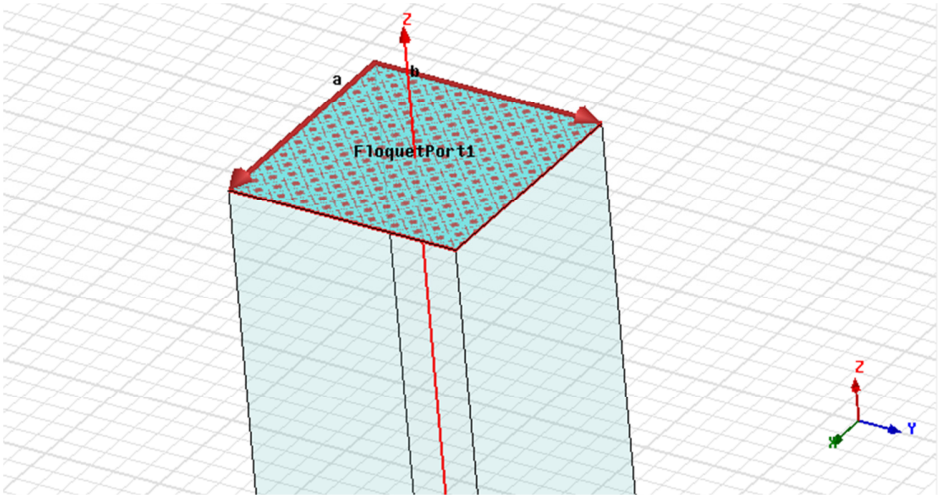

Figure A.3 Assign Floquet port

Click **Next** in the Floquet wizard to set the Phase Delays. Select the **Input Lattice Phase Delays** radio button, and click **Next** to go to the Modes setup page. On the **Modes setup** page, enter 6 as the **Number of Nodes**. This fills out the **Mode** table to 6 entries with initial 0 values. Click the **Modes Calculator** button for assistance in setting up the modes. Accept the values by clicking OK to close the Calculator. This fills out the table with calculated values. Accept default set up for the rest of Floquet port wizard.

Setup the Analysis

To setup this analysis, Right click on **Analysis** in the project tree, and select *Add Solution Setup.* This opens the **Solution Setup** dialog. On the General tab, set the **Solution frequency** to 10 Ghz. Set the **Maximum Number of Passes** to 10, and the **Maximum Delta S** as 0.02 as shown in Figure A.4. On the **Options** tab, check the **Do Lamda Refinement** box, and set the **Lambda** target as 0.2. Set the **Maximum Refinement Per**

Pass to 20%, the **Minimum Number of Passes** to 6, and the **Minimum Converged Passes** to 2. Select **First Order Basis** function, and click OK to accept the Setup.

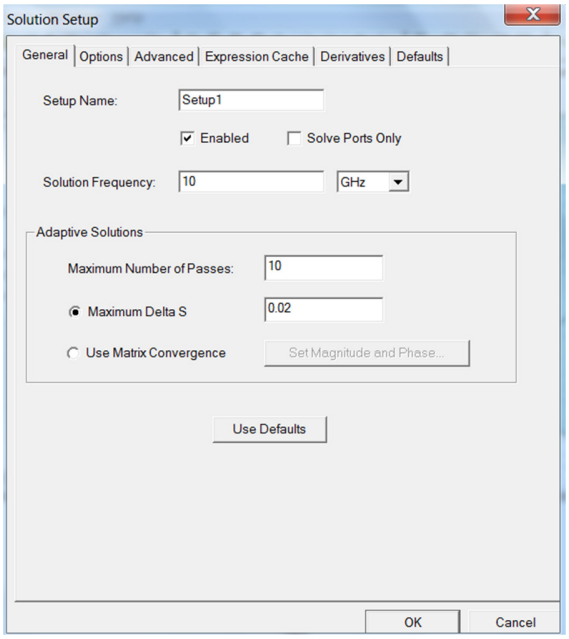

Figure A.4 Solution setup dialog

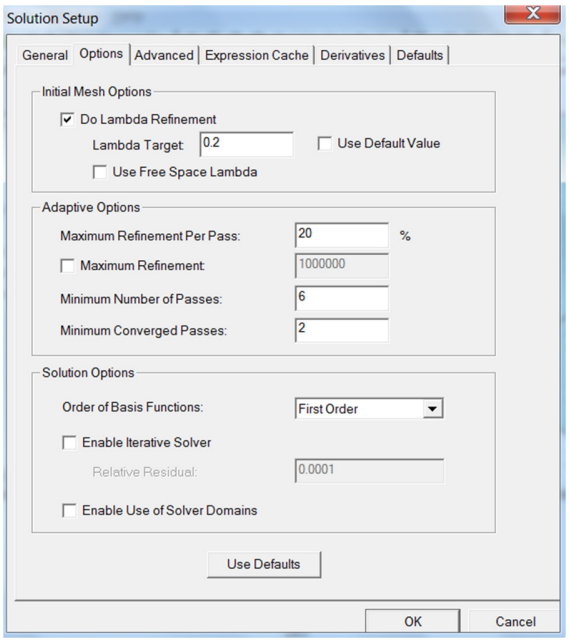

Figure A.5 Solution setup option dialog

Setup the Sweep

To setup the Sweep, Rightclick on Setup1 in the Project tree, and select **Add Frequency Sweep**. The **Edit Sweep** dialog appears. For the Sweep Type, select Interpolating. For the **Frequency Setup**, select Linear Step. Then set the Start as 8 GHz, the Stop as 20 GHz, and the Step Size as 0.2 GHz. For the **Interpolating Sweep** options, set the Max Solutions as 50, and Error Tolerance at 0.5%. Click the **Advanced Options** button to display the Interpolating Sweep Advanced Options dialog. Set the Minimum Solutions to 5, and the Minimum number of Subranges to 1. Click OK to close the Interpolating Sweep Advanced Options, and OK to close the Edit Sweep dialog. Right click on the Sweep in the Project tree and click Analyze on the shortcut menu to start the simulation. This will take some time.

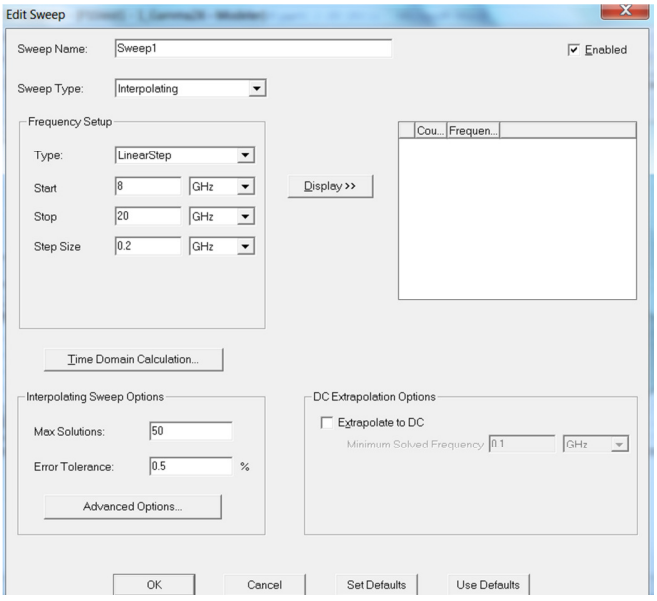

Figure A.5 Sweep setup dialog

APPENDIX B. AMC Simulation Using the Floquet Modal Analysis in Ansoft HFSS

The Sievenpiper mushroom structure has been widely studied in the microwave engineering field due to its unique properties. The Sievenpiper mushroom structure basically consists of a metallic patch connected to ground with a shorting post. The general model is shown in Fig. 1.

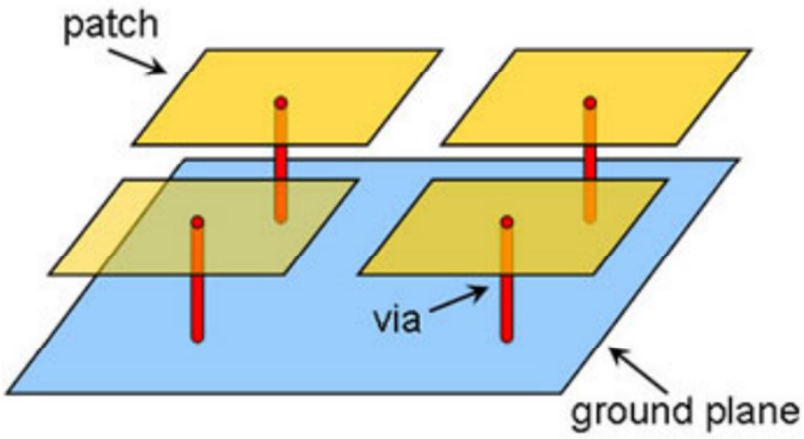

Figure B.1 General model of Sievenpiper mushroom surface

It can be used as a high-impedance surface and act like an artificial magnetic conductor. The Sievenpiper mushroom structure has also been widely used to realize AMC since it can be designed to have in phase reflection characteristic. In this appendix, the dispersion diagram of a Sievenpiper mushroom structure is generated using HFSS's eigenmode solver.

Dispersion Diagram Basics

We want to use HFSS to obtain a dispersion diagram for the Sievenpiper mushroom. A dispersion diagram is a plot of propagation constant versus frequency; a dispersion diagram basically tells you how much phase shift a material has at a given frequency. Since a Sievenpiper mushroom allows for waves to travel in two-dimensions, its propagation constant can be written as a vector quantity, $\boldsymbol{\beta} = \boldsymbol{x}k_x + \boldsymbol{y}k_y$. In order to generate the dispersion diagram, a unit-cell has to be defined and the appropriate periodic boundary conditions (PBCs) have to be applied.

The Brillouin zone is shown with the high-symmetry points defined as

$$\Gamma = (k_x p = k_y p = 0)$$

$$\mathrm{X} = (k_x p = \pi, k_y p = 0)$$

$$\mathrm{M} = (k_x p = k_y p = \pi)$$

The Brillouin zone is the most fundamental region for defining the propagation vector for a unit-cell; basically if one can define all the propagation vectors in the Brillouin zone, one obtains the entire characteristic of the entire periodic structure. Therefore the dispersion diagram will start at $\boldsymbol{\Gamma}$ then to $\boldsymbol{X}$ then to $\boldsymbol{M}$ and back to $\boldsymbol{\Gamma}$ as indicated by the path depicted on the Brillouin zone.

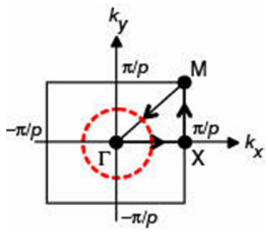

Figure B.2 Brillouin zone

Model Setup

First we must configure HFSS to use its eigenmode solver; *HFSS>Solution Type...>Eigenmode.* Next, the unit-cell of the Sievenpiper mushroom structure has to be drawn in HFSS. It consists of a square patch, a via, and a square block of substrate as shown in Figure B.3. The dimension of the patch is 4.8x4.8 mm^2 and is assigned a PEC boundary condition. The via has a radius of 0.12 mm, a height of 1.27 mm, and is assigned a perfect conductor material. In the case of the substrate, its dimensions are 5.0x5.0x1.27 mm^3 and the substrate material is Rogers RT/duroid 6010/6010LM.

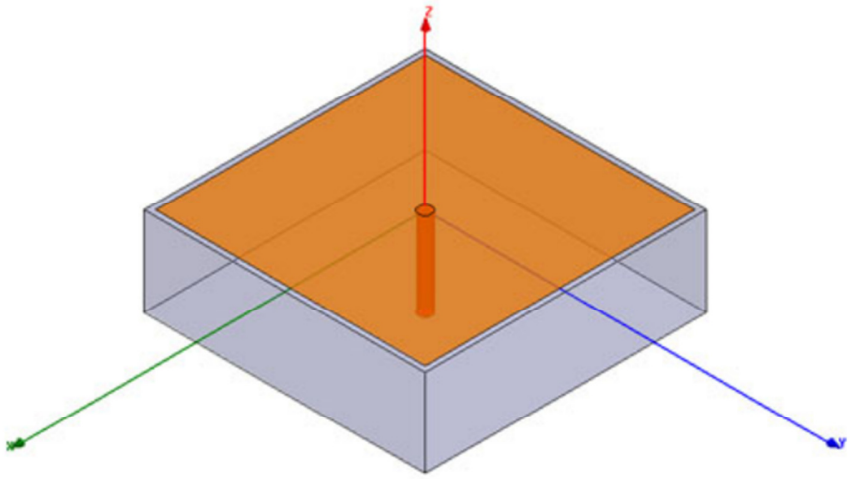

Figure B.3 HFSS model of Sievenpiper mushroom structure

Since the Sievenpiper structure is open to air in the positive z-direction, an airbox has to be defined for the simulation. To simulate an infinite free space, a perfect matched layer (PML) boundary is defined on top of the airbox as shown in Figure B.4. Radiation boundary cannot be used in the eigenmode simulation. The height of the airbox has to be approximately six times the substrate thickness. The default values for the PML boundary condition are used.

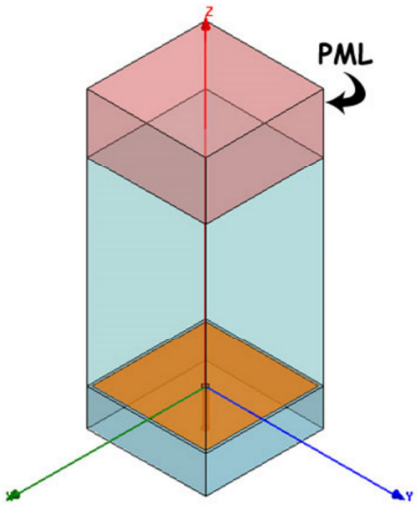

Figure B.4 Airbox and PML added to unit-cell

Periodic Boundary Conditions

Periodic boundary conditions must be applied to the face of the entire structure, which includes the airbox and the PML. Therefore, another airbox has to be created with encloses the original airbox and PML.

1. Select the negative y-z face of the unit-cell and assign a *Master Boundary Condition* (**mx**); you have to define the *U Vector* which starts at (-2.5, -2.5, 0) and ends at (-2.5, 2.5,0). The completed boundary assignment should look like Figure B.5. Next select the positive y-z face of the unit-cell and assign a *Slave Boundary Condition* (**sx**). Again define the *U Vector* which starts at (2.5, -2.5, 0) and ends at (2.5, 2.5, 0). Then input the phase delay using a variable (**px**) as shown in Figure B.6.

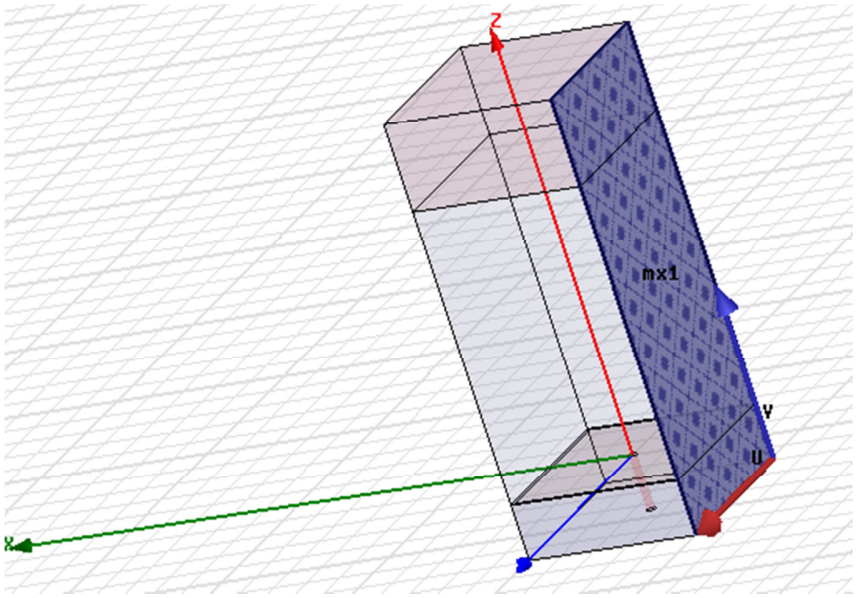

Figure B.5 Completed master boundary condition

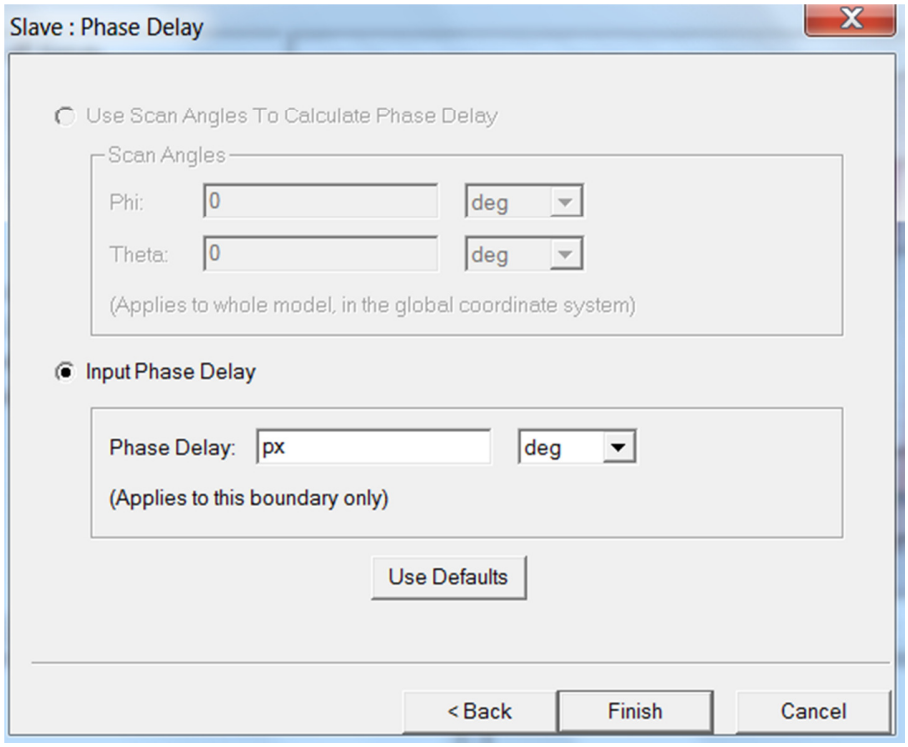

Figure B.6 Phase delay

2. Do the same to the x-z faces of the unit-cell. Label the master as **my** and the slave as **sy**. For **sy** make sure to reverse the *V Vector* and use a variable (**py**).

Analysis/Optometrics Setup

Before the eigenmode analysis can be started, several steps need to be completed first. First, add a solution setup and input the values as depicted in Figure B.7. In addition, in the options tab of the *Solutions Setup*, input a minimum converged passes of 2. Note that the mesh gets large (around 30,000 tets) for each eigenpoint. As a result, this simulation takes several hours even for only one mode.

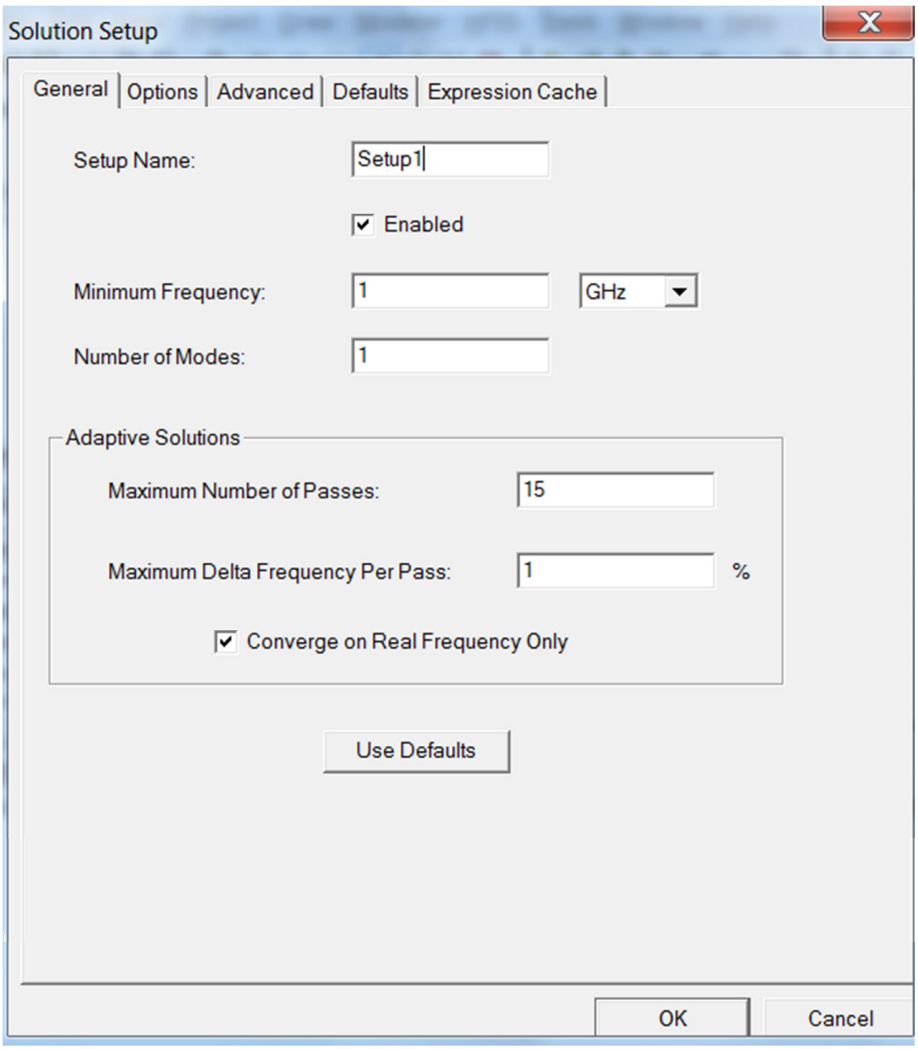

Figure B.7 Solution setup dialog

Next, parametric sweeps are added for each design in the simulation file.

For the first parametric sweep, we will go from Γ to X and. Add a linear step sweep for the variable **px** from 15 deg to 180 deg with 15 deg steps. In the Options tab make sure to check both *Save Fields and Mesh* and *Copy geometrically equivalent meshes.*

For the second parametric sweep, we will go from X to M and this will be labeled 2_X2M. Add a linear step sweep for the variable **py** from 15 deg to 180 deg with 15 deg steps. We have to set **px** to 180 deg. To do this go to General tab and check override for **px** and input 180 deg as shown in Figure B.8. In the options tab make sure to check both *Save Fields and Mesh* and *Copy geometrically equivalent meshes.*

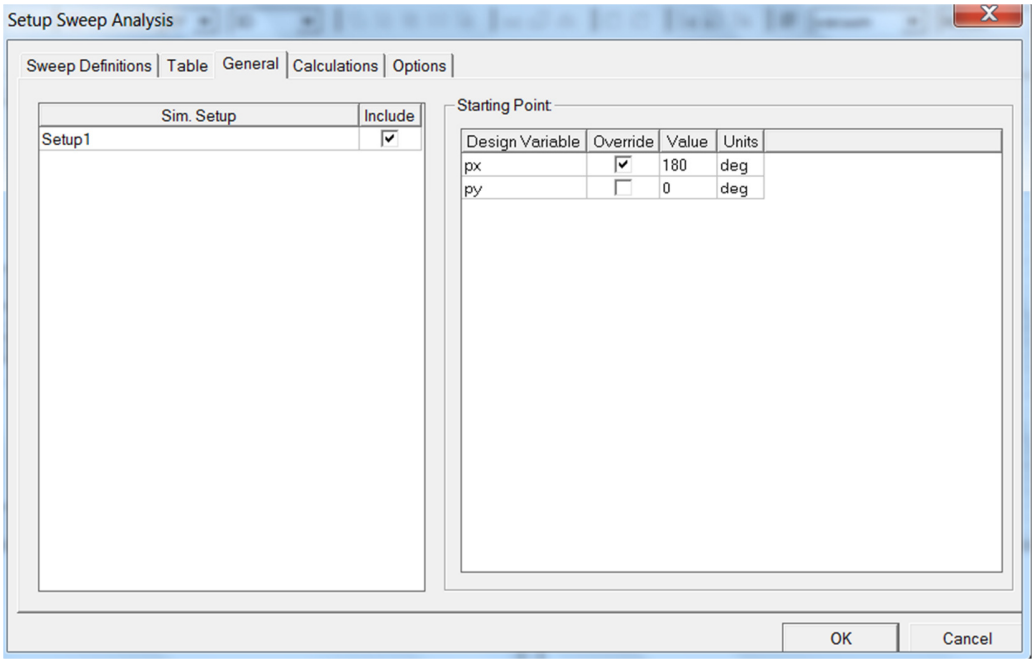

Figure B.8 Override **px** variable

For the third parametric sweep, we will go from M to Γ and this will be labeled 3_M2Gamma. Add a linear step sweep for the variable **px** from 15 deg to 180 deg with 15 deg steps and also for the variable **py.** Select both of these sweeps and Sync them as shown

in Figure B.9. In the options tab make sure to check both *Save Fields and Mesh* and *Copy geometrically equivalent meshes.*

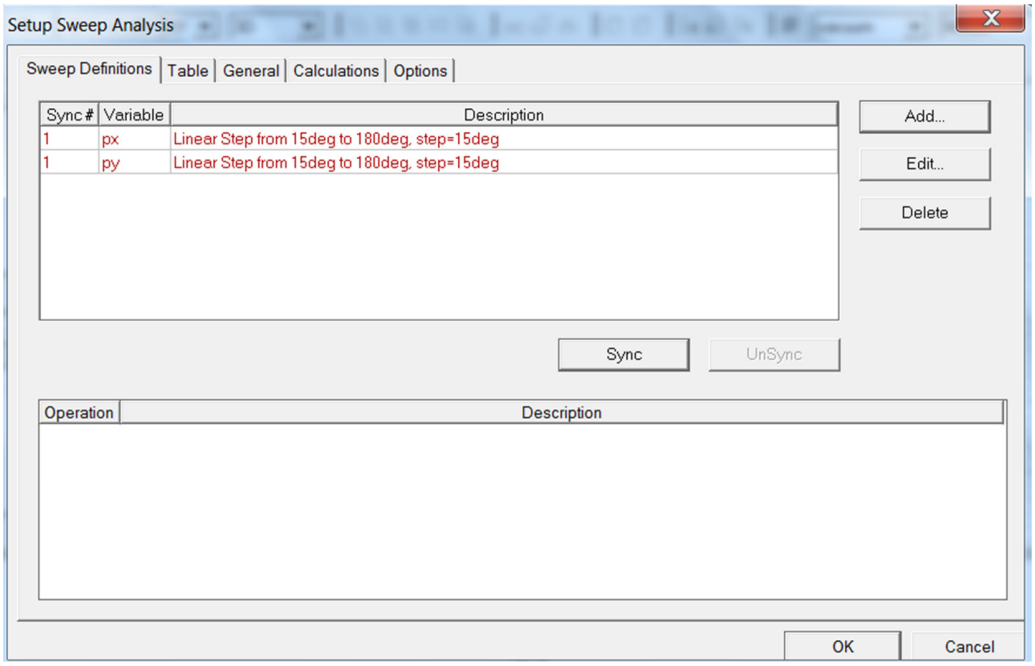

Figure B.9 Sync up sweeps

Plotting Results

Plots for each parametric sweep have to be made. For the Γ to X parametric sweep, create a report and use the default values (Eigenmode Parameters, Rectangular Plot). In the Sweep tab, choose *Sweep Design and Project variable values* and choose **px** values from 15 deg to 180 deg and for **py** select only 0 deg. For the Y tab, choose Eigen Modes>Mode(1) through Mode(4)>re. We only wish to look at the real part of the eigenmode, the imaginary part is due to loss which is ignored since a parallel plate waveguide's loss is negligible for the fundamental mode. The finished plot should look like Figure B.10.

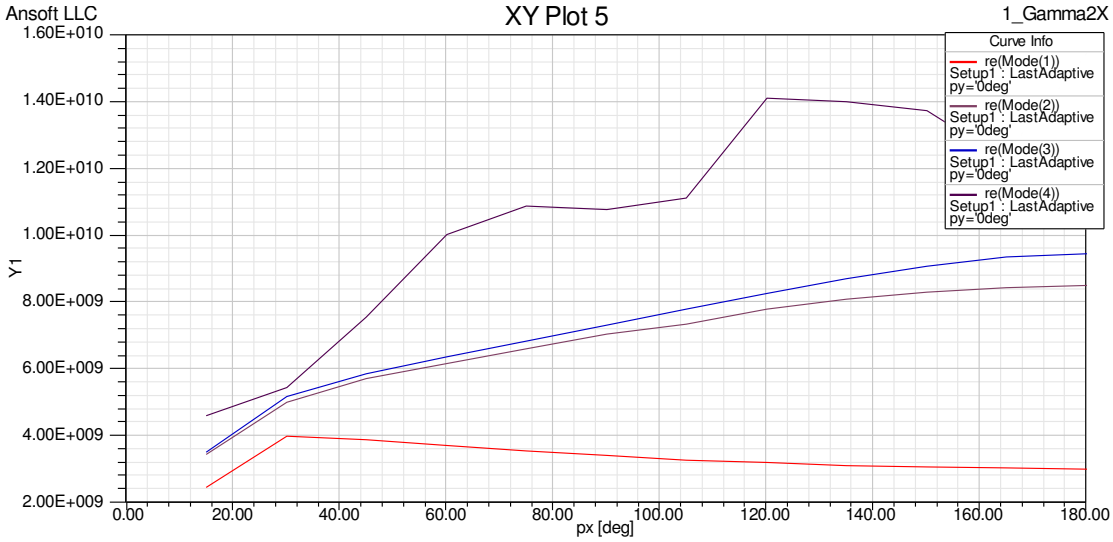

Figure B.10 Plot of Γ to X

To plot the X to M parametric sweep, do the same as for the Γ to X parametric sweep report. However, make **py** as the primary sweep and set **px** to 180 deg. The finished plot should look like Figure B.11.

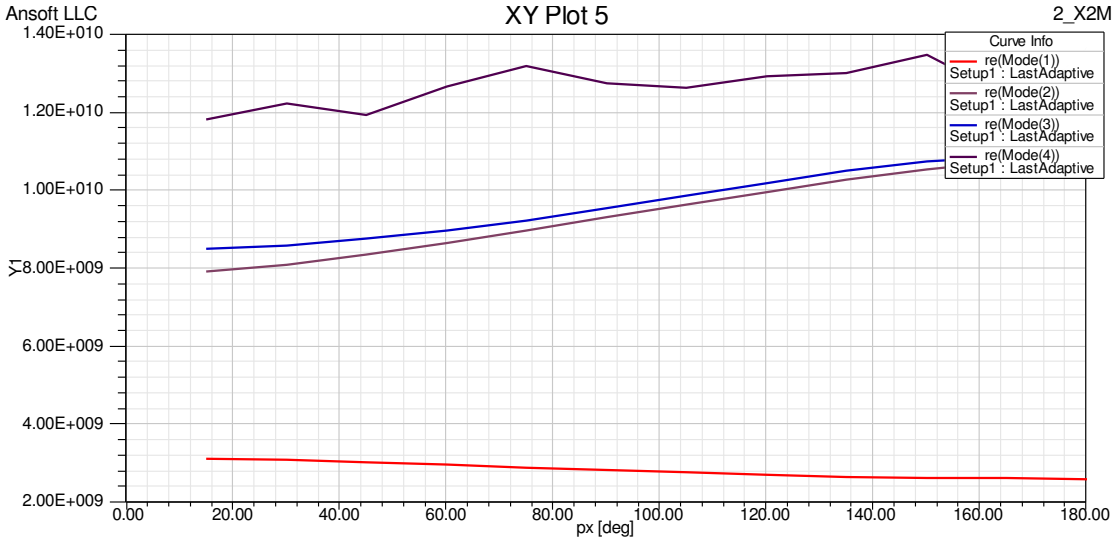

Figure B.11 Plot of X to M

To plot the *M* to *Γ* parametric sweep, do the same as for the previous plots, but this time select values of 15 deg to 180 deg for both **px** and **py**. However, the resulting plot will just be a series of unconnected dots. This is because HFSS's plotting function does not know which order to connect them. You can easy export the data and plot it yourself or create another HFSS design and only add an *M to Γ* parametric sweep. HFSS will then connect the dots in the results as shown in Figure B.12. The complete dispersion diagram is shown in Figure B.13; it was plotted by exporting the eigenvalues obtained from HFSS and using an external plotting program.

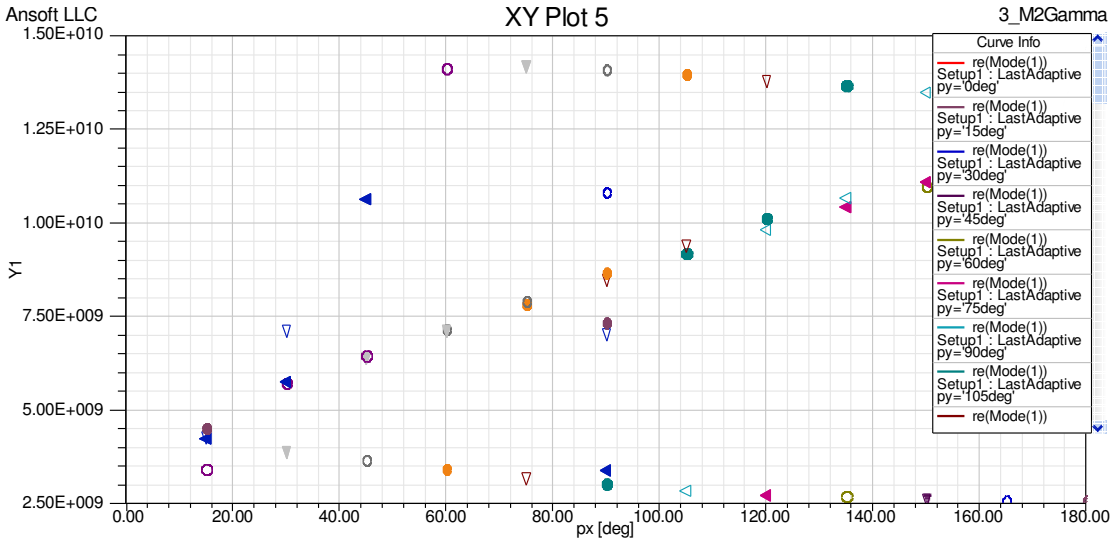

Figure B.12 Plot of *M* to *Γ*

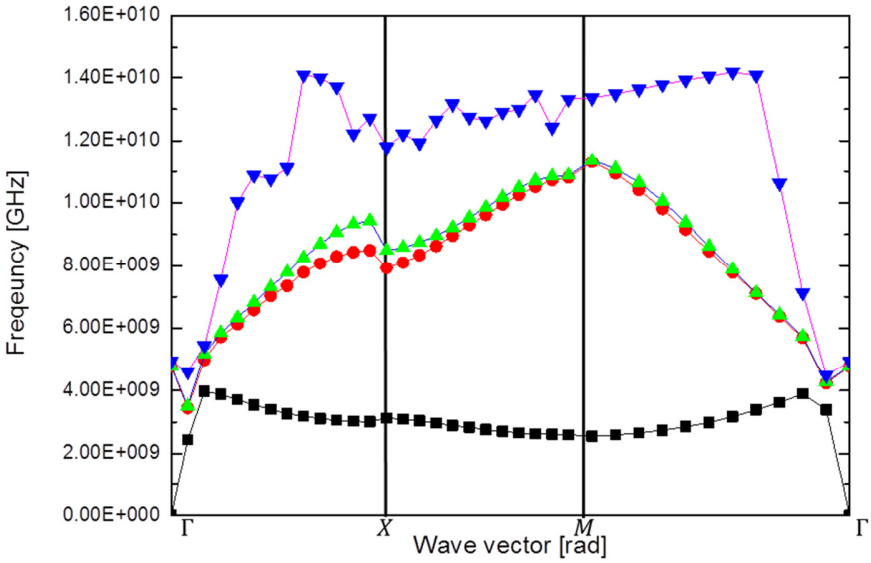

Figure B.13 Complete dispersion diagram